The effect of the heliospheric current sheet on cosmic-ray modulation

KD Moloto

20661533

Dissertation submitted in partial fulfilment of the requirements for the degree *Magister Scientiae* in Space Physics at the Potchefstroom Campus of the North-West University

Supervisor: Prof RA Burger

Assistant Supervisor: Prof H Moraal

October 2015

There is only one thing that makes a dream impossible to achieve: the fear of failure.

- Paulo Coelho

This work is dedicated to my parents

- For all the love and sacrifice.

Maktub

Abstract

The heliospheric current sheet is a dominant feature of the heliosphere. As solar activity increases, the tilt angle of the current sheet increases, and so does the region swept out by this structure, to cover most of the heliosphere during solar maximum conditions. An analysis of neutron monitor data in the form of count rate as function of tilt angle is presented. It is shown that the use of an effective tilt angle from a moving average preceding the time of observation, instead of the tilt angle at the time of observation, yields intensity-tilt loops that are in qualitative agreement with predictions of an idealized drift model. The characteristics of these loops are then a natural consequence of drift patterns during alternate solar magnetic polarity cycles. A detailed theoretical derivation for the drift-velocity field, valid throughout a model heliosphere that includes a wavy current sheet, is provided. A simplified *ab initio* approach is followed to model long-term cosmic-ray modulation using a steady-state three-dimensional numerical code. A composite slab/2D model is assumed for the structure of the turbulence. The spectra for the components are assumed to have a flat energy range and a Kolmogorov inertial range. Standard diffusion coefficients based on these spectra are used. A parameterized construction is used for the problematic drift coefficient, for which a generally accepted theoretical description is still lacking. The spatial dependence of magnetic variances and correlation scales, required as input for the drift- and diffusion coefficients, follows from parametric fits to results from a transport model for composite turbulence and not the model itself, hence the qualification of simplified and not fully *ab initio*. Effective values are used for all parameters in the modulation model. The unusually high cosmic-ray intensities observed during the 2009 solar minimum follow naturally from the current model for most of the energies considered. Lack of information about the solar-cycle dependence of all the required turbulence quantities at Earth, required such a dependence to be modelled. This was done in terms of the solar-cycle dependence of the magnetic field, for which long-term data exist. Reasonable qualitative agreement with

long-term cosmic-ray data is found. Better agreement is found for intensity as function of time at higher model energy, and better agreement with intensity-tilt loops at lower energy. In both cases, the highest model intensity occurs during the 2009 solar minimum. This is the first time that turbulence has been demonstrated as the most likely cause of the higher than usual cosmic-ray intensities during the 2009 solar minimum. It is shown that the temporal dependence of the current diffusion coefficients at Earth is inversely proportional to that of the magnetic field. It is, however, emphasized that this proportionality does not apply to their spatial dependence.

Keywords: Cosmic rays, current sheet, diffusion, gradient- and curvature drift, heliospheric magnetic field, modulation, turbulence

Acronyms and Abbreviations

The acronyms and abbreviations used in the text are listed below. For the purposes of clarity, any such usages are written out in full when they first appear.

2D	two-dimensional
AU	astronomical unit
HCS	heliospheric current sheet
HMF	heliospheric magnetic field
MHD	magnetohydrodynamic
NLGC	nonlinear guiding centre

Contents

CHAPTER 1

Introduction

GALACTIC cosmic rays that enter the heliosphere encounter a turbulent plasma originating at the Sun, embedded in which is the solar magnetic field. Perhaps the most prominent feature of the heliosphere within the termination shock is the current sheet that separates hemisphere with opposite magnetic polarity. The current sheet has a wavy structure due to the rotation of the Sun and the offset between the solar magnetic- and rotational axes. This offset increases as the Sun becomes more active, and consequently the current sheet sweeps out larger and larger regions of the heliosphere during the increasing phase of a solar activity cycle. When solar activity starts to decrease, so does the offset and the region swept out by the current sheet.

The goal of theoretical cosmic-ray modulation studies is to model the intensity of these charged particles as function of time and spatial position. In broad terms, two approaches are possible: to concentrate on fitting cosmic-ray observations, even if it means using *ad hoc* transport parameters; or, to try and model the underlying physical processes from first principles, and then see how well the resulting model can explain cosmic-ray observations. The second, *ab initio*, approach, is by far the most challenging. It has been shown to provide reasonable fits to cosmic-ray proton observations during solar minimum conditions [*Engelbrecht*, 2013; *Engelbrecht and Burger*, 2013].

The approach used in the present study can be seen as a simplified *ab initio* approach. It is *ab initio*, because standard unchanged expressions are used for the diffusion coefficients parallel- and perpendicular to the background magnetic field, and for the drift coefficient.

A choice is made for the form of the turbulence spectrum, and the structure of the turbulence is specified as a combination of slab turbulence and 2D-turbulence [*Matthaeus et al.*, 1990; *Matthaeus et al.*, 2007]. The transport of the respective variances and correlation scales follow from the model developed by *Oughton et al.* [2011] and applied by *Engelbrecht* [2013] to cosmic-ray modulation. The present approach is referred to as "simplified", because the turbulence transport model itself is not solved, but fits are made to the solutions for the spatial dependence of the turbulence parameters referred to above. Moreover, the turbulence is assumed to be independent of solar heliographic latitude. The challenge for the present project is that we not only need to know how turbulence evolves as function of radial distance at all solar heliographic latitudes, but also how it changes as function of solar activity. The sad fact is that it is completely unlikely that all of these observations will be carried out because it would require a huge armada of spacecraft gathering data over decades. Cosmic-rays traverse all of the heliosphere, and observations that span many decades are available. Cosmic rays can therefore be used as probes of turbulence, and may be able to give information about turbulence in regions and during periods where and when observations cannot be made, and likely will never be made.

The starting point then of the current model is a turbulence spectrum that in terms of frequency or wavenumber, has a flat energy range and a Kolmogorov inertial range, the latter with a spectral index of $-5/3$. While there is observational evidence that the turbulence spectrum at Earth is not flat in the energy range [see, e.g., *Bieber et al.*, 1993], there are indications that it is indeed flat at larger heliocentric radial distances [see, e.g., *Fraternale et al.*, 2015]. We assume that the turbulence is a composite of slab turbulence and 2D turbulence, as proposed by *Matthaeus et al.* [1990]. In the case of slab turbulence, the wave vectors are parallel to the background magnetic field. This kind of turbulence is often referred to as one-dimensional or Alfvénic turbulence. In the case of 2D turbulence, the wave vectors are in a plane perpendicular to the background magnetic field. Magnetic fluctuations perpendicular to the background magnetic field are therefore a mixture of slab- and 2D turbulence. We assume that the shapes of the slab- and the 2D spectra are the same [see, e.g., *Bieber et al.*, 1994].

To model the spatial dependence of the slab- and the 2D variance and the respective correlation scales, fits are made to the results presented by *Engelbrecht* [2013], and which are similar to those presented by *Oughton et al.* [2011]. As will be shown, to obtain good fits to a limited set of solar minimum cosmic-ray observations requires somewhat different spatial dependences of the turbulence quantities than those required to fit cosmic-ray observations over several decades.

Standard unchanged expressions are used for elements of the diffusion tensor, which are the diffusion coefficients parallel- and perpendicular to the background magnetic field, and the drift coefficient. These transport coefficients were derived for the shape of the turbulence spectra used here.

This study requires knowledge of the temporal behaviour over decades of all the turbulence quantities at Earth. This information is currently incomplete, and we therefore model the temporal dependence of the variances and correlation scales to be the same as some power of the magnitude of the observed magnetic field. Since the temporal dependence of the latter at Earth is known, we can model the temporal dependence of the variances and the correlation scales. We show that as a consequence of our choices, the temporal dependence at Earth of the parallel- and the perpendicular mean free path for protons at all energies is the same as that of the inverse of the magnitude of the magnetic field at Earth.

The diffusion tensor is then used in a three-dimensional steady-state numerical modulation model, originally constructed by *Hattingh* [1998]. Since cosmic rays that are observed at Earth have sampled solar wind plasma that has originated at the Sun over a period of a year or more, we use effective values for all input into the modulation model, calculated over a given period prior to the time the cosmic-ray observations were made. This approach has been used by e.g. *Potgieter et al.* [2014], but only for the heliospheric tilt angle and the magnitude of the heliospheric magnetic field. These authors did not consider a turbulence spectrum or any of its properties. The output of the modulation model is compared in different ways to neutron-monitor observations.

The next chapter gives a very brief overview of background to the present study, and some properties of cosmic rays and the heliosphere. In Chapter 3, an expression for cosmic-ray drift in a heliosphere that includes a wavy current sheet is derived.

In Chapter 4, a short introduction to turbulence properties that are relevant to the current study is given. Models are selected and introduced for diffusion- and drift coefficients, all of which depend upon turbulence quantities either through theory or through construction, if a theory is lacking.

In Chapter 5 a simple drift model is introduced to study the dependence of cosmic-ray intensities on the heliospheric tilt angle. To account for the difference between neutron monitor observations and the simple drift model, the concept of an effective tilt angle is introduced, and its effect on intensity-tilt loops from one solar activity cycle to the next, studied.

The results of the previous chapters are applied in Chapter 6 to study the modulation of galactic cosmic-ray protons with a three-dimensional steady-state cosmic-ray modulation

code. Energy spectra for three consecutive solar minima, including the so-called unusual minimum of 2009, are calculated and compared with observations. Model results are compared with cosmic-ray observations spanning almost 40 years, as well as predicted properties of intensity-tilt loops. The consequence of the assumed solar-cycle dependence of turbulence for the diffusion tensor is also discussed.

In Chapter 7 a summary of the work presented in this study is given, along with the conclusions drawn from the results gained.

CHAPTER 2

Structure And Properties Of The Heliosphere And Its Constituents

2.1 Introduction

OUR local star, the Sun, is a rotating magnetic star of which the atmosphere constantly blows radially away. It forms a huge bubble of supersonic plasma, the solar wind [see, e.g., *Parker*, 1958b], which engulfs the Earth and the other planets, shaping their environments. The term heliosphere describes this region of interstellar space directly influenced by the Sun. Embedded in the solar wind is the Sun's turbulent magnetic field, which is transported with it into space and which in turn plays a major role in the transport of cosmic rays. Changes in the intensity of these charged particles with time as a function of energy and position is referred to as the modulation of cosmic rays.

In what follows aspects of the structure of the Sun, the heliosphere, the modulation of cosmic rays, their classification and origin, as well as models for the heliospheric magnetic field (HMF), are briefly outlined.

2.2 The Basic Structure Of The Sun

The Sun is the largest and most prominent object in our solar system. It is a magnitude 4.8 star of spectral type G2V, with a mass of $\sim 2 \times 10^{30}$ kg and a radius of $\sim 7 \times 10^{5}$ km

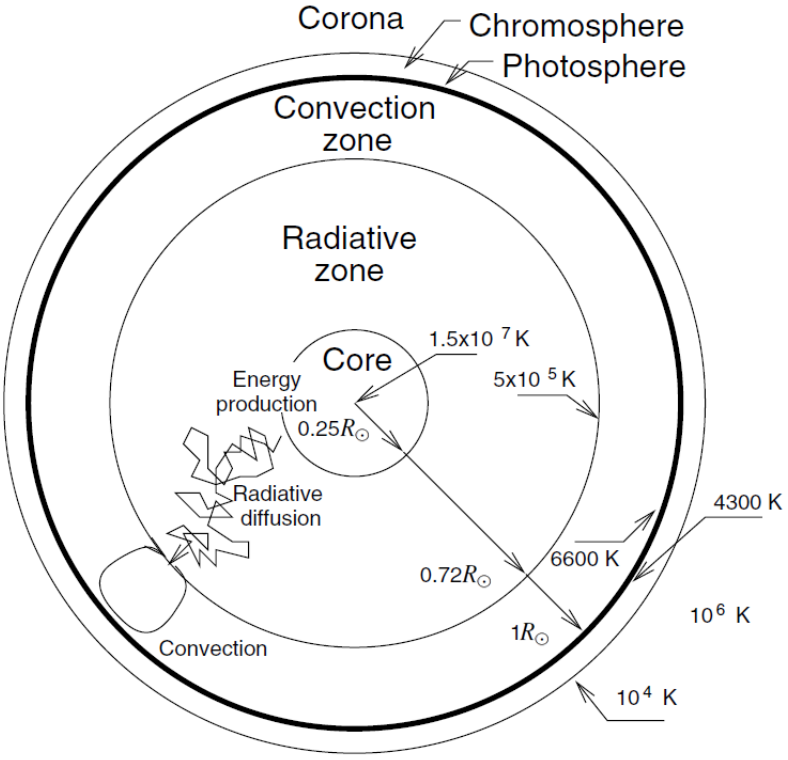

Figure 2.1: *A representation of the internal structure of the Sun and its immediate surroundings. The regions inside the Sun are defined by how energy is transferred from the core to the surface. The regions of the Sun's atmosphere are defined by their density and temperature [Koskinen, 2011].*

[*Kallenrode*, 2001]. It contains more than 99.8 % of the solar system mass and is composed of 92 % hydrogen and 7 % helium, the remainder being traces of heavier elements. The mean distance from the Sun to the Earth is $\sim 1.5 \times 10^8$ km and is called an astronomical unit, abbreviated as AU in this study.

Figure 2.1 illustrates the interior structure of the Sun, which is divided into six regions, and its immediate surroundings [see, e.g., *Castellani et al.*, 1997; *Brun et al.*, 1998; *Shaviv and Shaviv*, 2003; *Koskinen*, 2011]:

The Core

The core region is the high density, high temperature region at the centre of the Sun where thermonuclear energy production takes place. It contains half of the solar mass and all the Sun's energy production takes place in this region.

Radiative Zone

Above the core is a region of highly ionised gas (dense plasma) called the radiative zone. The energy produced in the core is transported through the core and the radiative zone by gamma-ray diffusion. The gamma rays are scattered, absorbed

and re-emitted many times before they reach the outer edge of the radiative zone. The process can take of order a hundred thousand years.

The Convection Zone

In the uppermost 30 % of the solar interior is the convection zone. In this region the solar material is convectionally unstable because the radial temperature gradient is large. The Sun is in a plasmatic state and this allows for gas around the equator to rotate faster than the gases closer to the poles. This is called differential rotation and it takes the gas at the equator about 25.4 days to rotate once around the Sun while it takes close to 32 days for the gases close to the poles [*Snodgrass*, 1983]. The synodic period of the Sun as observed from Earth, at a solar heliographic latitude of 26 degrees, is about 27.3 days. The inner part of the Sun seems to rotate as a solid sphere. It is only the outer 30 % of the Sun that experiences differential rotation. At the bottom of the convection layer, two layers with different rotation speeds meet, creating "velocity shear". This is the area where it is believed the Sun's magnetic field is created and where sunspots and other solar activity phenomena are generated [see, e.g., *Spiegel and Zahn*, 1992; *Brun et al.*, 1999]. Energy is transported outwards towards the solar surface by the convective motion of large cells. These convection cells give the Sun's surface its characteristic granular appearance [see, e.g., *Garaud and Guervilly*, 2009].

The Photosphere

The photosphere is the region where outgoing matter changes rapidly from completely opaque to almost completely transparent, allowing electromagnetic radiation to escape freely into space [*Meyer-Vernet*, 2007].

The Chromosphere

The next part of the solar atmosphere, just above the photosphere, is called the chromosphere. This is the pinkish region visible just before a total solar eclipse [*Meyer-Vernet*, 2007]. The chromosphere is followed by a very thin narrow transition layer where the temperature increases from $\sim 10^4$ K to $\sim 10^6$ K. The mechanism resposible for this increase is unknown [see, e.g., *Meyer-Vernet*, 2007; *Pontieu et al.*, 2009].

The Corona

The outermost part of the solar atmosphere is the corona. This is the region that is visible during a total eclipse. Due to the negative pressure gradient between the solar corona and interplanetary space at large radial distances, the particles in the corona must constantly be accelerated radially outward, reaching a supersonic flow speed in order to maintain dynamic equilibrium [*Parker*, 1958a]. This outflow is known as the solar wind, as previously noted.

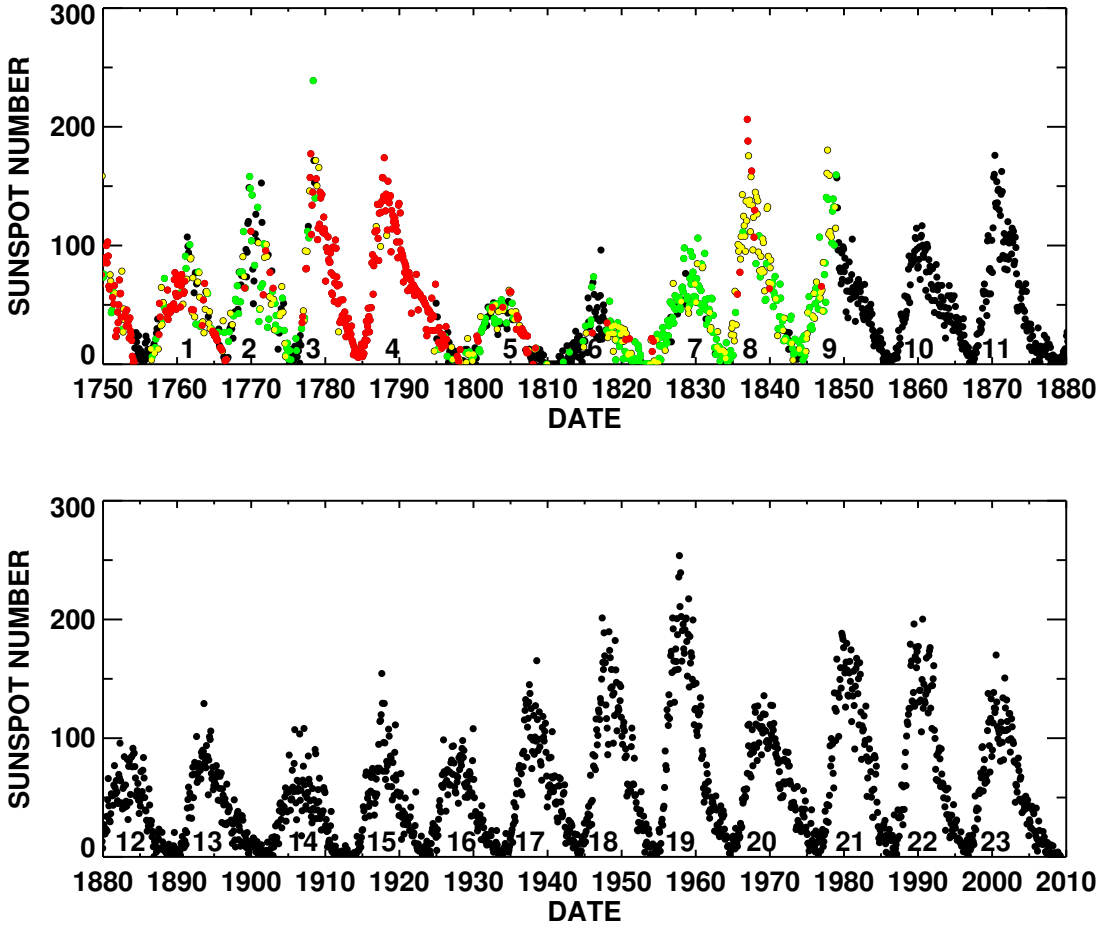

Figure 2.2: *Monthly averaged sunspot numbers from 1750 to 1880 in the top panel, and 1880 to 2010 in the bottom panel. The numbers above the date axis are solar cycle numbers. Months with full observations are shown in black. Those with 1-10 days missing are shown in green and those with 11-20 days missing are shown in yellow. Months with more than 20 days missing are shown in red. The first official solar cycle started in 1755, while cycle number 23 ended on December 2008 [Hathaway, 2010].*

2.3 Solar Activity

Sunspots are dark areas of irregular shape seen on the photosphere of the Sun. These regions are associated with strong magnetic fields and are direct indicators of the level of solar activity [*Schrijver et al.*, 1998]. If these fields have strengths of ∼0.3 T, they limit effective heat conduction. This implies a local temperature reduction and thus that these regions are cooler than the rest of the surface [*Meyer-Vernet*, 2007].

Monthly averages of sunspot numbers are shown in Figure 2.2. From these observations it is evident that the Sun has a quasi-periodic ∼11 year solar activity cycle. In this cycle the Sun goes through a period of fewer and smaller sunspots during solar minimum followed by a period of larger and more sunspots during solar maximum. *Hale* [1908] discovered that the leading spots in sunspot pair have opposite polarities in opposite

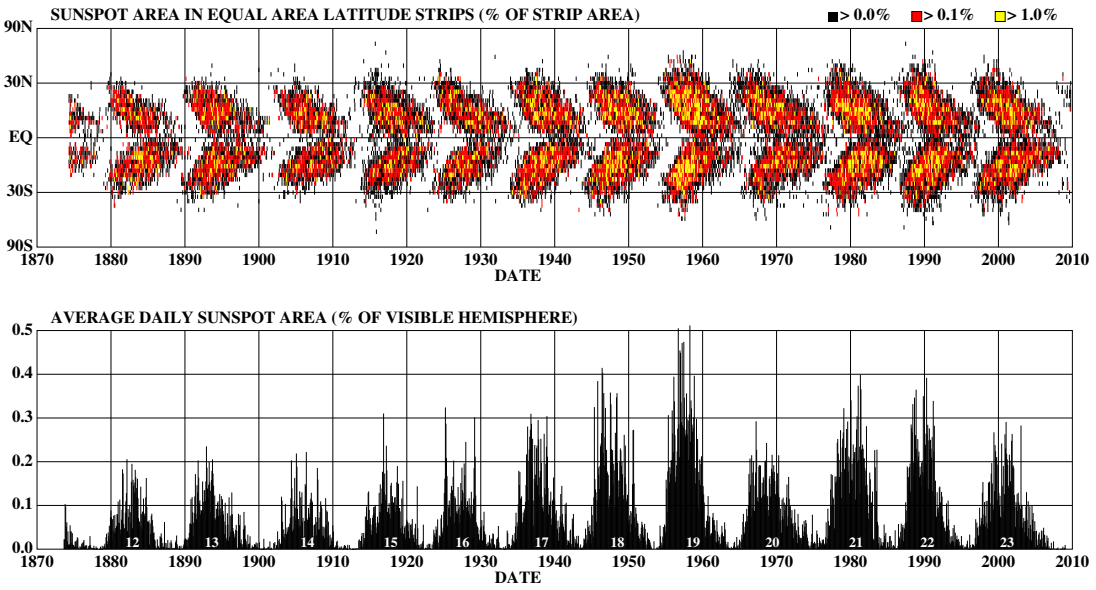

Figure 2.3: *Sunspot area as a function of latitude and time in the top panel. The average daily sunspot area for each solar rotation since May 1874 is plotted as a function of time in the bottom panel. Sunspots form in two bands, one in each hemisphere, and migrate toward the equator as the cycle progresses [Hathaway, 2010].*

hemispheres and this is known today as Hale's sunspot polarity law. The magnetic polarities of sunspot pairs alternate in a hemisphere every ∼11 years due to the solar activity cycle. If, for instance, the leading sunspot in a pair in the northern hemisphere has a positive polarity in one solar activity cycle, the leading sunspot will have a negative polarity in the next cycle. Conversely, the leading sunspot in the southern hemisphere will have a negative polarity in the first solar activity cycle and positive polarity in the second one. This leads to the conclusion that the solar magnetic field oscillates with a mean period of ∼22 years, reversing polarity every ∼11 years. Sunspots also show a clear latitudinal dependence during a solar cycle, called Spörer's Law, shown in the top panel of Figure 2.3. They form in two bands on either side of the Sun's equator, first at mid-latitudes and later move towards the solar equator during solar maximum, but with a zone of avoidance near the equator. When these sunspots fade, sunspots of the new cycle start appearing at mid-latitudes, creating the Maunder Butterfly diagram [*Maunder*, 1904]. The bottom panel shows the average daily sunspot area for each solar rotation.

2.4 The Solar Wind

The concept of a solar wind, originally called solar corpuscular radiation, was introduced ∼50 years ago to account for the fact that comets' tails always point radially away

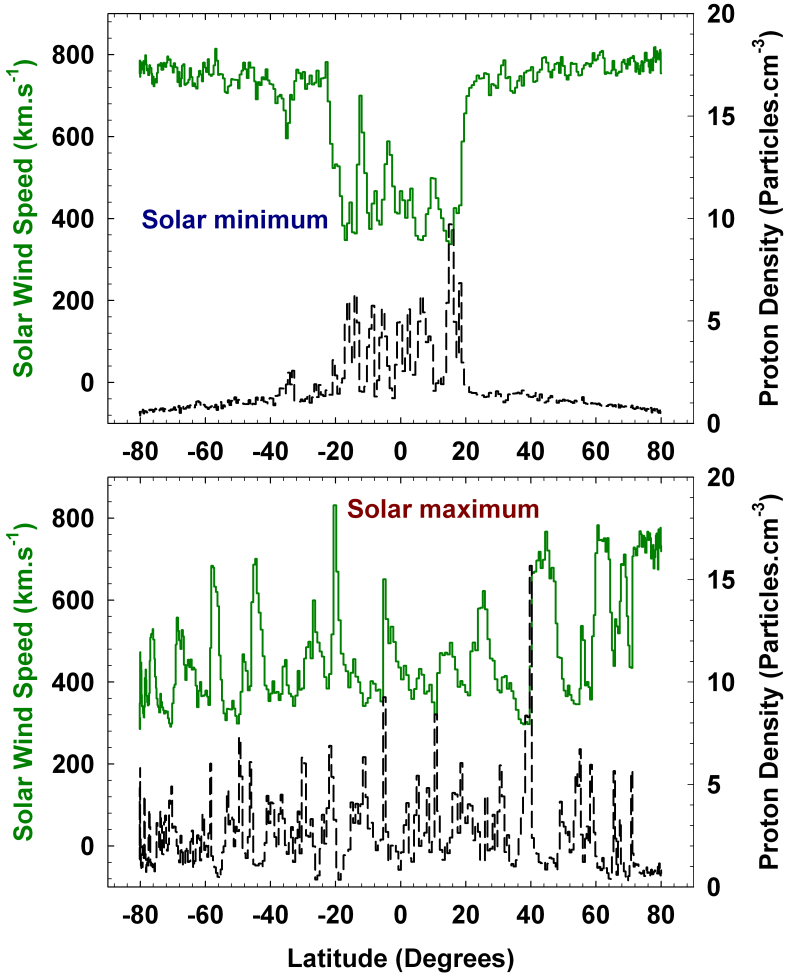

Figure 2.4: *The solar wind speed (green line) and the solar wind proton density (black line) as measured by the Ulysses spacecraft during solar minimum conditions (top panel, September 1994 - July 1995) and solar maximum conditions (bottom panel, October 2000 - September 2001). The solar equator is located at 0° latitude [Strauss, 2010].*

from the Sun, regardless of the position of the comet. The name 'solar wind' was first introduced by *Parker* [1958a] who argued that the atmosphere of the Sun could not be in static equilibrium and was in fact expanding at supersonic speed. The highly-conducting solar wind carries the solar magnetic field embedded in it into interplanetary space, forming the heliospheric magnetic field (HMF) which plays a key role in the modulation of cosmic rays in the heliosphere. The first *in situ* observations of the supersonic solar wind were made by the *Mariner 2* spacecraft [see, e.g., *Gombosi*, 1998].

Early estimates of the solar wind speed, based on its effect on comets, were in the region of $400\,\mathrm{km\,s^{-1}}$ to $1000\,\mathrm{km\,s^{-1}}$, which is not too far from today's observed values. Observations by the *Ulysses* spacecraft [see, e.g., *McComas et al.*, 2000] have revealed unambiguously that the solar wind speed is not uniform over all latitudes and can

broadly be divided into a fast and a slow solar wind. The latitudinal dependence of the solar wind occurs due to the interaction between the expanding corona and the Sun's magnetic field. Close to the Sun, plasma flow is dominated by the Sun's magnetic field, which is in the form of a dipole during solar minimum conditions [see, e.g., *Gosling and Pizzo*, 1999]. In the solar equator regions, the radial plasma flow and the Sun's magnetic field are orientated almost perpendicular to each other and the magnetic field thus inhibits the expansion of the corona. These field lines are in the form of loops which begin and end on the solar surface and stretch around the Sun to form the streamer belts. In turn these streamer belts are regarded as the most plausible sources of the slow solar wind, which has typical average speed of up to $400\,\mathrm{km\,s^{-1}}$. Other indications are that the slow solar wind may arise from the edges of coronal holes [see, e.g., *Smith*, 2000; *Schwenn*, 2006; *Wang*, 2011].

In the polar regions, however, the Sun's magnetic field is dominated by polar coronal holes which form open magnetic field lines directed parallel to the outflowing solar wind and so do not inhibit it's flow, giving rise to the fast solar wind streams in these regions. The latitudinal dependence of the solar wind speed is thus defined by the latitudinal distribution of polar coronal holes on the Sun's surface [see, e.g., *Cranmer*, 2009; *Wang*, 2009]. During solar maximum conditions the polar coronal holes show no clear distribution, and neither does the solar wind. The fast solar wind has a characteristic average speed of up to $800\,\mathrm{km\,s^{-1}}$ and emanates from the polar coronal holes that are typically located at higher heliographic latitudes. The fast solar wind can sometimes extend close to the equator and overtake the earlier emitted slower stream, resulting in corotating interaction regions (CIRs) [see, e.g., *Fujiki et al.*, 2003; *McComas et al.*, 2008; *Heber*, 2011].

This latitudinal dependence of the solar wind speed was observed by the *Ulysses* spacecraft during solar minimum conditions as shown in the top panel of Figure 2.4. During solar maximum conditions, shown in the bottom panel, no clear latitude dependence can be distinguished. Also shown in Figure 2.4 is the solar wind proton density, which is inversely correlated to the solar wind speed as required by the conservation of mass flux.

A simplistic understanding of the formation of the heliosphere is that the solar wind flows radially outward from the Sun and therefore blows a spherical bubble that continually expands. But as the solar wind expands into space, its pressure decreases with radial distance from the Sun. This is because interstellar space is not empty, but contains matter in the form of the interstellar medium (ISM). At some stage the speed of the supersonic solar wind plasma decreases to subsonic speeds and a heliospheric shock, called the solar wind termination shock (TS) forms [see, e.g., *Choudhuri*, 1998]. Beyond

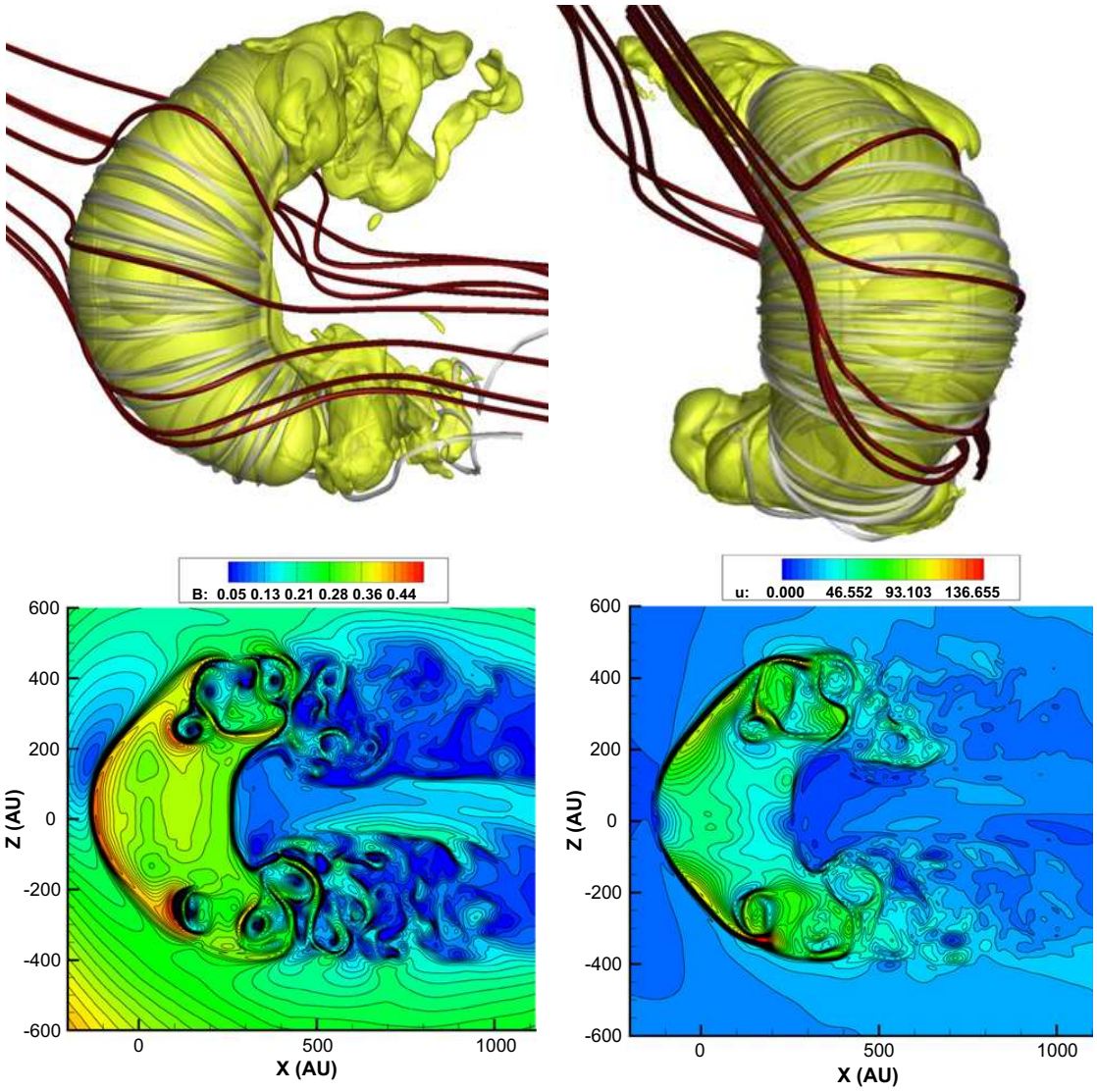

Figure 2.5: *Two-lobe structure heliosphere with an interstellar magnetic field resulting from MHD simulations. The top left-hand and right-hand panels show the side and nose view of the heliosphere, respectively. The grey lines are solar magnetic field lines; the red lines are interstellar magnetic field. The bottom left-hand and right-hand panels show magnetic field and solar wind speed contours, respectively [Opher et al., 2015].*

this point, which two measurements show occurs at a distance of between 83.7 AU to 94 AU [e.g., *Stone et al.*, 2005; *Stone et al.*, 2008] the solar wind propagation direction in the front/nose of the heliosphere changes to the meridional and azimuthal directions as it is "turned around" by its encounter with the ISM.

The traditional view of the shape of the heliosphere is that it is a quiescent, comet-like object aligned in the direction of the Sun's trajectory through the ISM [*Parker*, 1961; *Baranov and Malama*, 1993] with a long tail extending for thousands of AU. A dramatically different scenario is described by *Opher et al.* [2015] who argue, based on magnetohydrodynamic (MHD) simulations, that the twisted magnetic field of the Sun

confines the solar wind plasma beyond the termination shock and drives jets to the north and south of the heliosphere, very much like some observed astrophysical jets. These jets are deflected into the tail region by the motion of the Sun through the ISM. The interstellar wind blows the two jets into the tail but is not strong enough to force the lobes into a single comet-like tail. Instead, the interstellar wind flows around the heliosphere and into the equatorial region between the two jets, thus separating them as can be seen in the top left-hand and right-hand panels of Figure 2.5, which show the the side view and nose view of the simulated heliosphere, respectively.

The lobes are turbulent (due to large-scale MHD instabilities and reconnection) and strongly mix the solar wind with the ISM beyond ∼400 AU. This can be seen in the bottom left-hand and right-hand panels of Figure 2.5, which shows the magnetic and solar wind speed contours, respectively. The large-scale voids indicate that mixing of the ISM and solar material has taken place. The presence of turbulent lobes has significant implications for magnetic reconnection and particle acceleration in the heliosphere.

Opher et al. [2015] suggest that the two-lobe structure is consistent with the energetic neutral atom (ENA) images of the heliotail from *IBEX* where two lobes are visible in the north and south and the suggestion from the *Cassini* ENAs that the heliosphere lacks a tail [*Krimigis et al.*, 2009; *McComas et al.*, 2013].

2.5 The Heliospheric Magnetic Field

On average, the Sun is like a bipolar bar magnet, with one hemisphere having a positive and the other one a negative polarity, and a thin plane in the equatorial region being neutral [*Stix*, 2004]. As was noted previously, this polarity is reversed every 11 years, resulting in a 22-year magnetic field cycle. One can expect that a charge-sign dependence in cosmic-ray transport will reflect the 22-year magnetic cycle. That this is the case, is clearly visible in Figure 2.6, which shows a periodicity of approximately 22 years in cosmic-ray intensity at Earth.

During solar minimum conditions the heliosphere is dominated by the influence of the high speed solar wind originating from well developed polar coronal holes on the Sun. Most heliographic magnetic field lines have their origin in the coronal holes and are swept out into the heliosphere by the solar wind [*Balogh et al.*, 1995]. Figure 2.7 shows a two-dimensional schematic presentation of the magnetic field within a few solar radii. The closed field lines that begin and end on the the solar surface are the streamer belts and the open magnetic field lines that get dragged into the heliosphere by the solar wind form the heliospheric magnetic field.

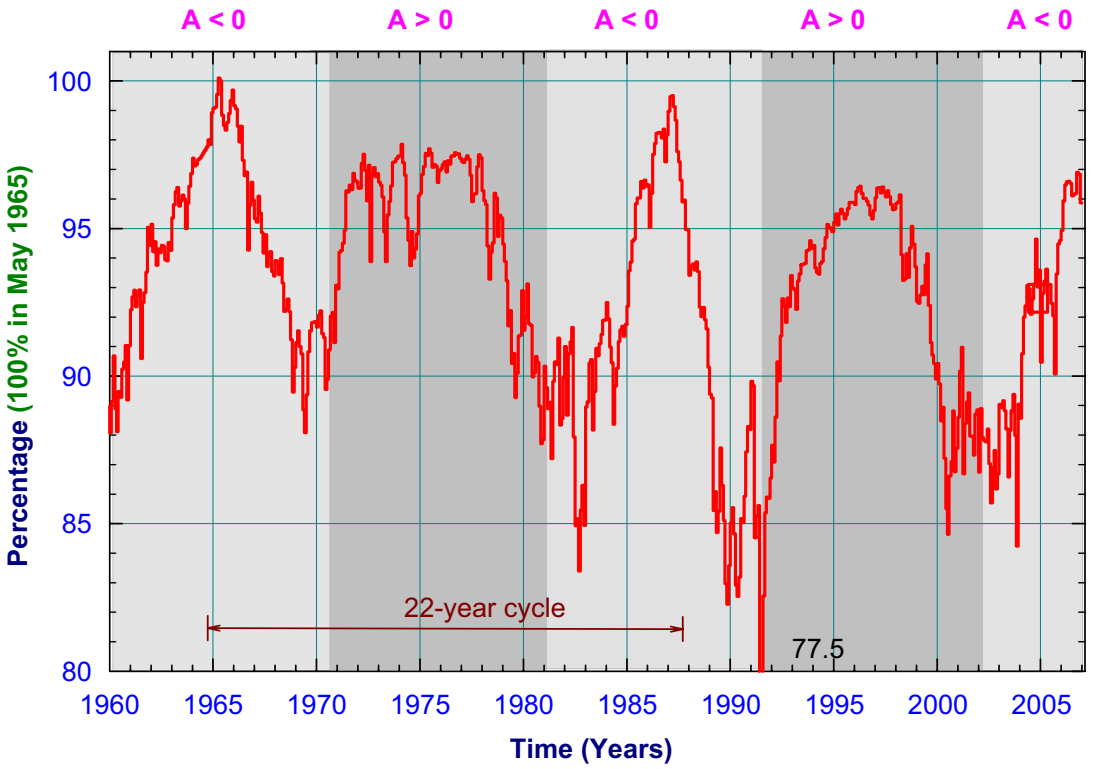

Figure 2.6: *Cosmic ray intensity, corrected for atmospheric pressure changes, as measured by the Hermanus neutron monitor [Potgieter, 2008].*

Latitudinal differences in the rotation speed of the Sun causes stretching and distortions in the field lines and eventually kinks and twists develop. This differential solar rotation winds the magnetic field around the Sun's equator, adding more complexity to its structure [see, e.g., *Phillips et al.*, 1995]. In this work we are interested in the global magnetic field of the Sun, the open magnetic field lines which are dragged into the heliosphere.

There are a variety of models for the HMF [for a review see *Burger*, 2005]. Perhaps the most interesting one is the model of *Fisk* [1996], but it is also the most controversial [see, e.g., *Roberts et al.*, 2007]. In the current study the model of *Parker* [1958a] will be used because there is no evidence yet that a study of long-term cosmic-ray modulation requires a more complex field. However, Fisk fields and their variants can in principle explain short-term intensity variations observed by the same instruments used to study long-term modulation [see, e.g., *Engelbrecht*, 2008]. These fields have a meridional component in contrast to the less complex Parker field. We will therefore discuss both the Parker field and Fisk-type fields as representative of models of the HMF.

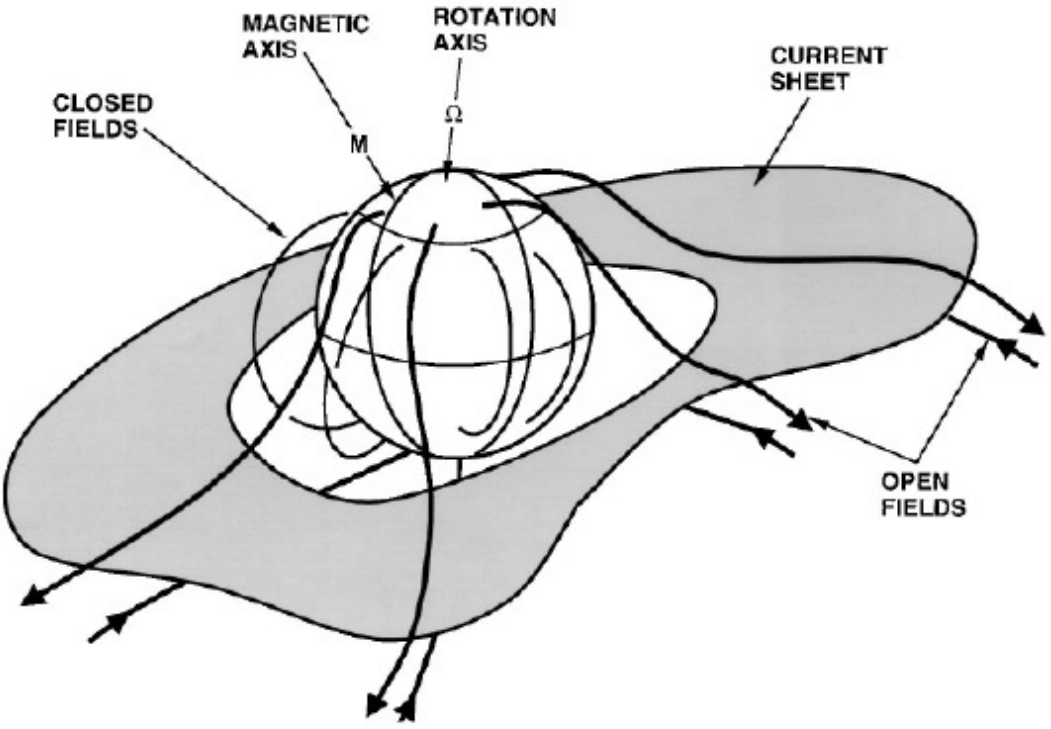

Figure 2.7: *Schematic representation of the solar magnetic field lines near the Sun. The closed fields (loops) begin and end on the Sun. The open fields have one end on the Sun, the other "end" being carried off by the solar wind. The shaded surface is the heliographic current sheet [Smith, 2001].*

2.5.1 Parker Model Of The Heliospheric Magnetic Field

This, the simplest of the models for the heliospheric magnetic field, was first derived by *Parker* [1958a]. The field is written in heliographic coordinates as

$$\mathbf{B} = A \left(\frac{r_e}{r}\right)^2 (\mathbf{e}_r - \tan\psi \mathbf{e}_\phi)\,, \tag{2.1}$$

with $r_e = 1\,\mathrm{AU}$, $\mathbf{e}_r$ and $\mathbf{e}_\phi$ unit vectors in the radial and in the azimuthal direction, respectively, and $|A|$ is the magnitude of the radial component of the field at Earth. The sign of A indicates the polarity of the field. When it is positive, the field in the northern hemisphere points away from the Sun, while it points inward in the southern hemisphere. The reverse applies when A is negative. In what follows, the notation $A > 0$ for positive polarity and $A < 0$ for negative polarity will be used.

The quantity ψ is the Parker spiral angle, which is the angle between the radial direction and that of the average HMF at a certain position, defined by

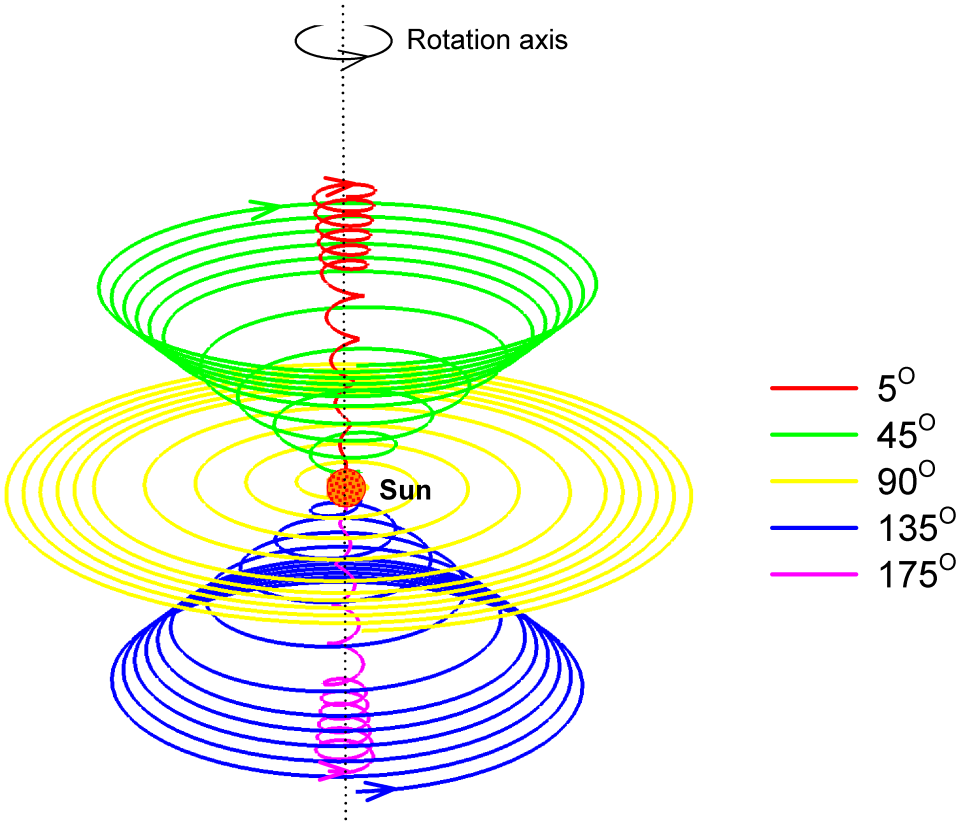

Figure 2.8: *A graphical illustration of the 3D structure of the Parker HMF lines corresponding to different polar angles 5° (red), 45° (green), 90° (yellow), 135° (blue) and 175° (purple) with Sun at the centre. The magnetic field lines are compressed from the position of TS to the heliopause due to the slow solar wind in the inner heliosheath region. The dotted vertical line represents the rotation axis (magnetic pole) of the Sun. The arrows show the direction of the HMF and the direction of rotation about the axis of the Sun [Manuel, 2013].*

$$\tan\psi = \frac{\Omega\,(r - r_{\mathrm{o}})\sin\theta}{V_{sw}}, \tag{2.2}$$

where V_{sw} is the solar wind speed, $\Omega = 2.67 \times 10^{-6}\,\mathrm{rad\,s^{-1}}$ is the average angular rotation speed of the Sun, r is heliocentric radial distance, θ is polar angle (colatitude), and r_{o} is the radial distance at which the field is assumed to be purely radial, and which defines the spherical source surface. The theoretical description of the HMF is usually assumed to apply from this surface onward. Since the source surface is at a fraction of an AU, r_o is often neglected compared to heliocentric radial distance in a 100 AU heliosphere. The spiral angle gives an indication of how tightly wound the HMF spiral is. The basic structure of the HMF is thus that of Archimedean spirals lying on cones of constant heliographic latitude, as shown in Figure 2.8. The cones and the corresponding magnetic field lines do not cross or merge, since the divergence of the magnetic field must at all times remain zero. Note that the current study makes no assumptions regarding

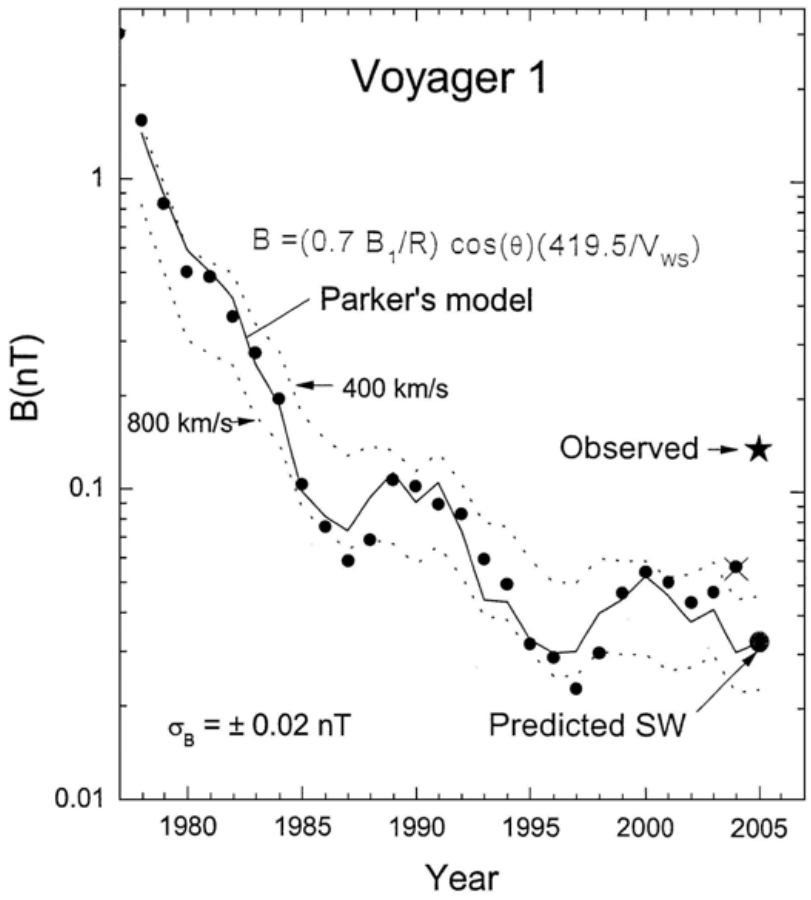

Figure 2.9: *Comparison of Voyager 1 yearly averages of HMF magnitude since launch with the Parker model using measured HMF at 1 AU. The dots show the yearly averages measured by Voyager 1 and the solid curve is Parker's model. The dashed curves are the predictions of Parker's model for a solar wind speed of 400 km s^{-1} and 800 km s^{-1}, respectively. Solar cycle changes with a period of ∼11 years can be seen to be superimposed on the long-term decrease [Ness, 2006].*

the structure of the field beyond the termination shock, in contrast to *Manuel* [2013] and other authors.

Note that the ratio Ω/V_{sw} is very close to 1 AU^{-1} for a 400 km s^{-1} solar wind, expressed in AU s^{-1}. Since at Earth $r = 1$ AU and the polar angle $\theta = 90°$, a typical value of ψ is 45° at Earth and tends to 90° when $r \geq 10$ AU in the equatorial plane. Observations have revealed the existence of a Parker spiral HMF at mid to low heliolatitudes, but the structure at polar regions is still under debate [see *Ness and Wilcox*, 1965; *Thomas and Smith*, 1980; *Roberts et al.*, 2007; *Smith*, 2011; *Sternal et al.*, 2011]. The magnitude of the HMF at Earth has an average value of $B_e \approx 5$ nT to 6 nT during typical solar minimum conditions, but increases with time by up to a factor of ∼2 during solar maximum conditions. The magnitude of the Parker HMF from Equation 2.1 is given by

$$B = |A| \left(\frac{r_e}{r}\right)^2 \sqrt{1 + \left(\frac{\Omega\,(r - r_o)\sin\theta}{V_{sw}}\right)^2}. \tag{2.3}$$

Note that beyond a few AU, the magnitude decreases as r^{-2} in the solar equatorial region, but as r^{-1} over the solar poles where $\sin\theta$ is close to zero. Figure 2.9 shows the comparison of the Parker model with the magnetic field in the equatorial plane as observed by *Voyager 1*, the latter indicated by dots. The HMF estimate from Parker's model (shown as a solid line) is based upon the observed HMF at Earth and solar wind speeds measured (within 10 AU) or estimated (beyond 10 AU) using *Voyager 1* data. Note that the *Voyager 1* solar wind plasma probe failed shortly after the Saturn encounter in 1979. Deviations of the estimated field due to lower or higher average solar wind speeds, indicated by the two dotted lines, are for speeds of $400\,\mathrm{km\,s^{-1}}$ and $800\,\mathrm{km\,s^{-1}}$, respectively. As is clear from Equation 2.3, a larger solar wind speed results in a smaller magnitude of the field at a given radial distance. Clearly evident in this figure are two local maxima and two local minima in the HMF during 1990 and 2000, and 1987 and 1997, respectively, which are 11-year variations associated with solar activity.

2.5.2 Fisk-Type Models Of The Heliospheric Magnetic Field

In the previous section it was shown that observations indicate that the HMF close to the ecliptic can be considered, on average, to be a simple Archimedean spiral as predicted by Parker's model. However, *Fisk* [1996] pointed out that a correction needs to be made to the Parker model, the reason being that the Sun undergoes differential rotation as discussed in Section 2.2. If it is assumed that the HMF footpoints are connected to the photosphere, they too will undergo differential rotation. The interplay between the differential rotation of the footpoints of the HMF lines on the photosphere of the Sun, and the subsequent non-radial expansion of the field lines with the solar wind from coronal holes, can result in excursions of the field lines with heliographic latitude [*Fisk*, 1996].

In Fisk-type models the HMF footpoints thus undergo a double precession, shown in Figure 2.10. Hence, as opposed to the Parker model, footpoints on the source surface do not only rotate about $\boldsymbol{\Omega}$, but also about a virtual axis $\mathbf{p}$, which in turn, rotates about $\boldsymbol{\Omega}$. The axis $\mathbf{p}$ is the radial extension of the point where the field line originating at a solar pole, which experiences no effect of differential rotation, maps out to the source surface. Note that the magnetic and rotational axes of the Sun are misaligned by the tilt angle α [see, e.g., *Burger et al.*, 2008].

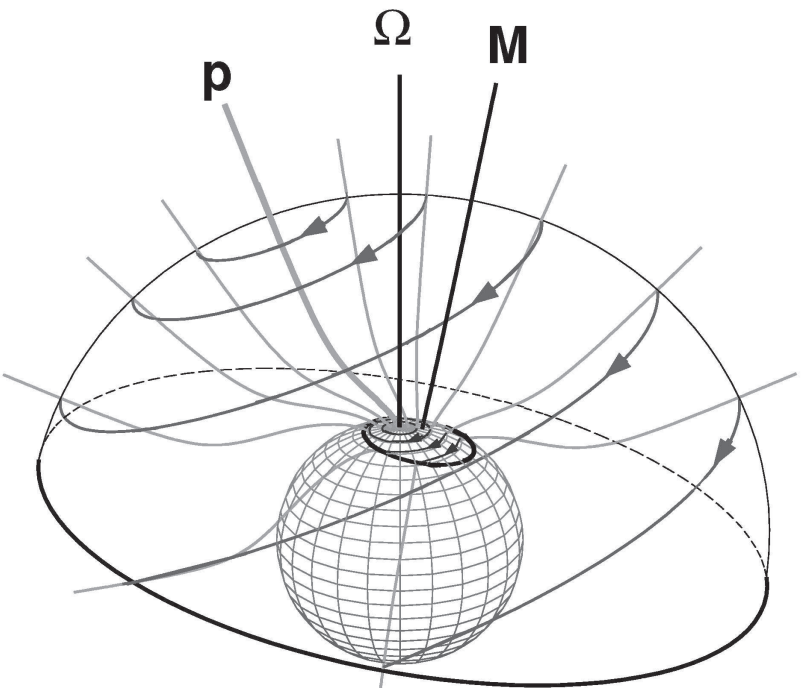

Figure 2.10: *A schematic illustration of the expansion of magnetic field lines from a polar coronal hole in the Sun's northern hemisphere according to the model by Fisk [1996]. Magnetic field lines anchored on the photosphere (inner sphere) are projected onto the solar wind source surface (outer sphere) [Fisk et al., 1999].*

The three components of the original Fisk field model, which are only valid at high latitudes, are given by [*Zurbuchen et al.*, 1997]

$$\begin{aligned} B_r &= B_e \left(\frac{r_e}{r}\right)^2 \\ B_\theta &= B_r \frac{\omega r}{V_{sw}} \sin\beta \sin\left(\phi + \frac{\Omega r}{V_{sw}}\right) \\ B_\phi &= B_r \frac{r}{V_{sw}} \left[\omega \sin\beta \cos\theta \cos\left(\phi + \frac{\Omega r}{V_{sw}}\right) + \sin\theta \left(\omega \cos\beta - \Omega\right)\right], \end{aligned} \tag{2.4}$$

with B_e the magnitude of the radial component of the HMF at Earth. Note that for historical reasons this quantity is denoted by $|A|$ in expressions for the Parker field, as in e.g. Equation 2.1. Here ω is the differential rotation rate (usually taken to be a constant fraction of Ω) and β the angle between the rotation axis of the Sun and the **p**-axis. The model of *Fisk* [1996] has been the subject of various studies [see, e.g., *Zurbuchen et al.*, 1997; *Fisk et al.*, 1999; *Fisk*, 2001; *Van Niekerk*, 2000]. However, not only is it not valid at all heliographic latittudes, it turned out to be rather difficult to implement in numerical modulation models [see, e.g., *Kóta and Jokipii*, 1997, 1999, 2001; *Burger et al.*, 2001; *Burger and Hitge*, 2002]. *Burger and Hitge* [2004] introduced a hybrid approach to Fisk-type fields, which combines a Fisk field at high latitudes with a Parker

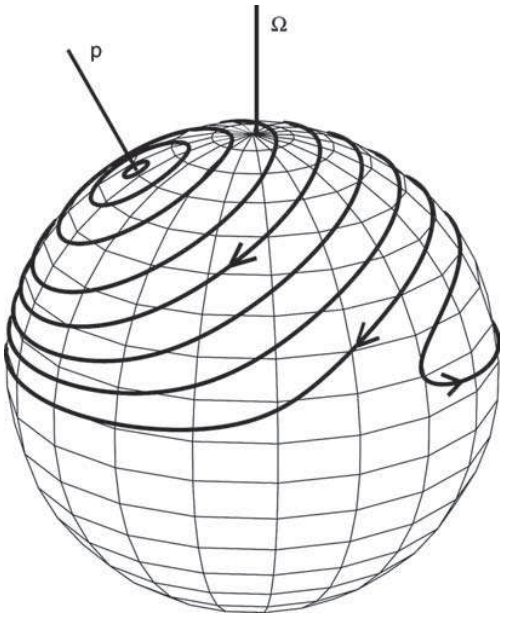

Figure 2.11: *Illustration of the trajectories of coronal magnetic field lines which open into the heliosphere in both the polar coronal hole and at low latitudes. Adapted from Fisk et al. [1999].*

field at low latitudes to reflect spacecraft observations of the HMF described above. The expression for the components of their field in heliographic coordinates is

$$\begin{aligned}\mathbf{B} = B_e \left(\frac{r_e}{r}\right)^2 \Bigg\{ \hat{\mathbf{e}}_\mathbf{r} + \frac{\omega r F_S}{V_{sw}} \sin\beta \sin\left(\phi + \frac{\Omega r}{V_{sw}}\right) \hat{\mathbf{e}}_\theta \\ + \frac{r}{V_{sw}} \Bigg[\omega F_S \sin\beta \cos\theta \cos\left(\phi + \frac{\Omega r}{V_{sw}}\right) \\ + \sin\theta \left(\omega F_S \cos\beta - \Omega\right) \\ + \omega \frac{dF_S}{d\theta} \sin\beta \sin\theta \cos\left(\phi + \frac{\Omega r}{V_{sw}}\right) \Bigg] \hat{\mathbf{e}}_\phi \Bigg\},\end{aligned} \tag{2.5}$$

where F_S is referred to as a transition function. The latter depends only on polar angle, where $F_S = 1$ at high latitudes (small polar angles) the field is a pure Fisk field, and where $F_S = 0$ at low latitudes (polar angles close to 90°) it is a pure Parker field, while intermediate values indicate a mixture or hybrid of the two fields. Note that if $\beta = 0$, the meridional component of the field disappears and it becomes a pure Parker field. Trajectories of the magnetic field footpoints on the source surface for this field are shown in Figure 2.11. Note that the hybrid field has field line footpoints moving parallel to the solar heliographic equator at low latitudes, but the footpoint trajectories at high latitudes are similar to the trajectories shown in Figure 2.10. In later papers, Fisk and co-workers would define a return region at low latitudes surrounding the solar magnetic equator [see, e.g., *Fisk et al.*, 1999].

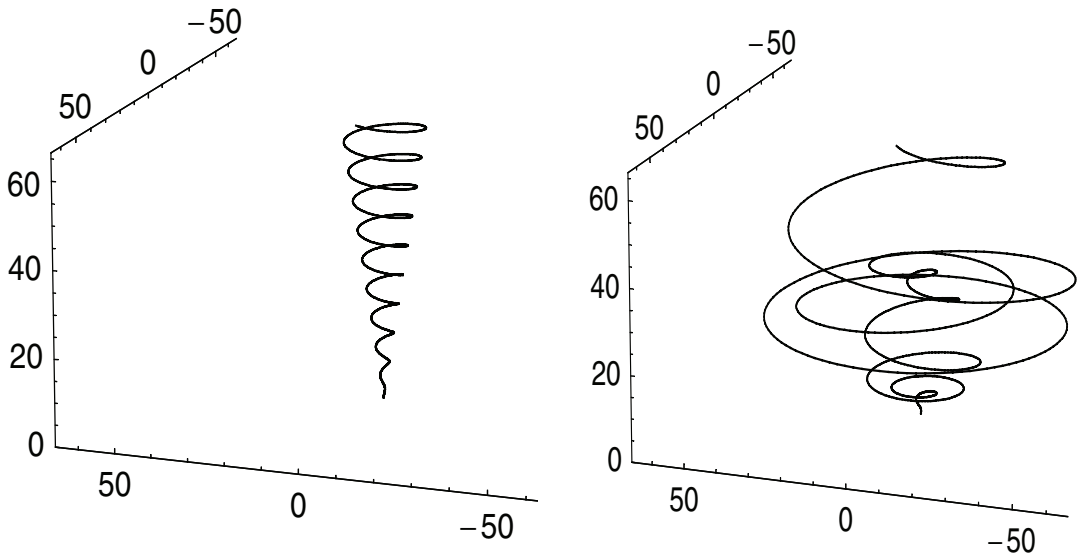

Figure 2.12: *Configuration of a magnetic field line originating at 10° colatitude, for the Parker field (left-hand panel) and the Fisk field (right-hand panel). All units are AU [Burger, 2005].*

While the hybrid model introduced by *Burger and Hitge* [2004] has been refined somewhat in later work [see, e.g., *Burger et al.*, 2008], the basic concept remains the same. Differential rotation indeed has a large effect on the structure of the heliospheric magnetic field. This is shown in Figure 2.12, which compares a field line originating at the same latitude, for the Parker field (left-hand panel) and the pure Fisk field (right-hand panel). The large latitudinal excursions experienced by field line in the Fisk model are clearly shown in this comparison.

The left-hand panel of Figure 2.13 shows a field line originating at the same latitude as those in Figure 2.12. Although not identical because of the value of F_S not being exactly equal to 1, the hybrid field yields field lines that are qualitatively the same as for the pure Fisk field. However, as one moves to lower latitudes close to the heliographic equator, shown in the right-hand panel of Figure 2.13, the field clearly becomes Parker-like, with a significant meridional component only very close to the Sun.

The hybrid field of *Burger et al.* [2008] has been used by other authors to study the effect of a Fisk-type field on the modulation of charged particles in the heliosphere [see, *Engelbrecht*, 2008; *Sternal et al.*, 2011].

2.6 Heliospheric Current Sheet

The heliospheric current sheet (HSC) is a major three-dimensional corotating structure in the heliosphere, which is an extension of the magnetic equator (or neutral line, see

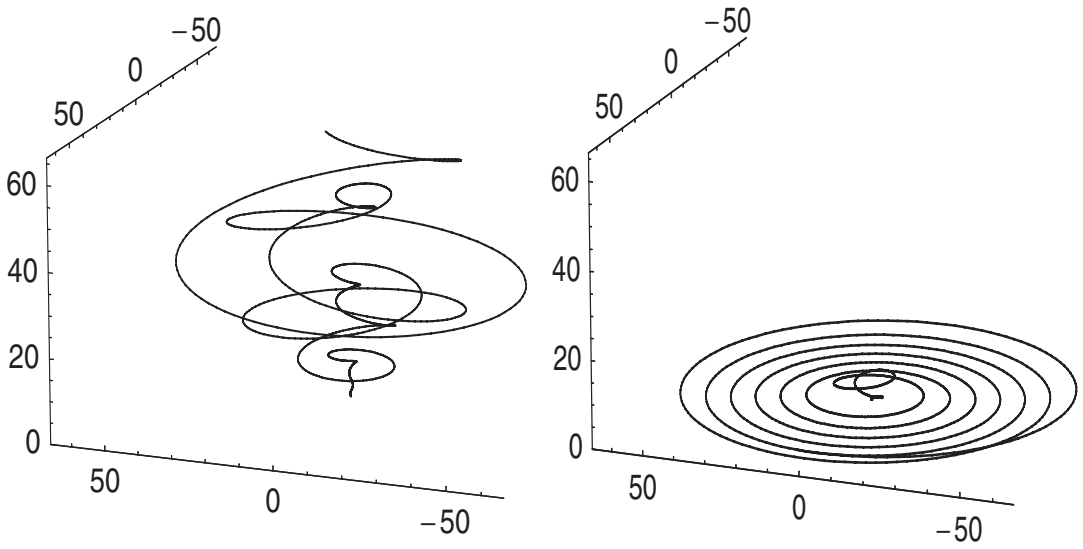

Figure 2.13: *Configuration of a magnetic field line originating at 10° colatitude (left-hand panel) and 85° colatitude (right-hand panel), for the hybrid field. All units are AU [Burger, 2005].*

Section 2.5.2) from the source surface to the outer regions of the heliosphere, separating the two hemispheres of opposite magnetic polarities. The origin of the HCS lies in the open magnetic field lines that originate on the solar surface at high latitude and get dragged towards the ecliptic plane, as shown in Figure 2.7. Being part of the HMF, it is frozen into the solar wind and propagates radially outward with the wind as shown in the same figure.

As mentioned in Section 2.5, the rotational and magnetic axes of the Sun are misaligned by the tilt angle α. As the Sun rotates, the HCS also rotates, resulting in a wavy or warped structure. At 1 AU the thickness of the HCS is ∼10 000 km [*Smith*, 2001], which is so thin by astronomical standards that it is often assumed to be of zero thickness. The structure of the HCS varies greatly during a solar cycle. The tilt angle α increases with increasing solar activity, greatly warping the structure of the current sheet. Increasing solar activity may also affect the dipolar structure of the solar magnetic field, introducing quadrupole moments which may result in multiple current sheets in the heliosphere [*Kóta and Jokipii*, 2001]. As solar minimum conditions return, the solar magnetic and rotational axes almost align, producing a fairly simple, single current sheet. In the present study, it is assumed that only a single current sheet occurs at all levels of solar activity.

An expression for the wavy HCS was first derived by *Jokipii and Thomas* [1981]. It can be derived by considering Figure 2.14 (see also *Krüger* [2005]). The tilted dashed circle

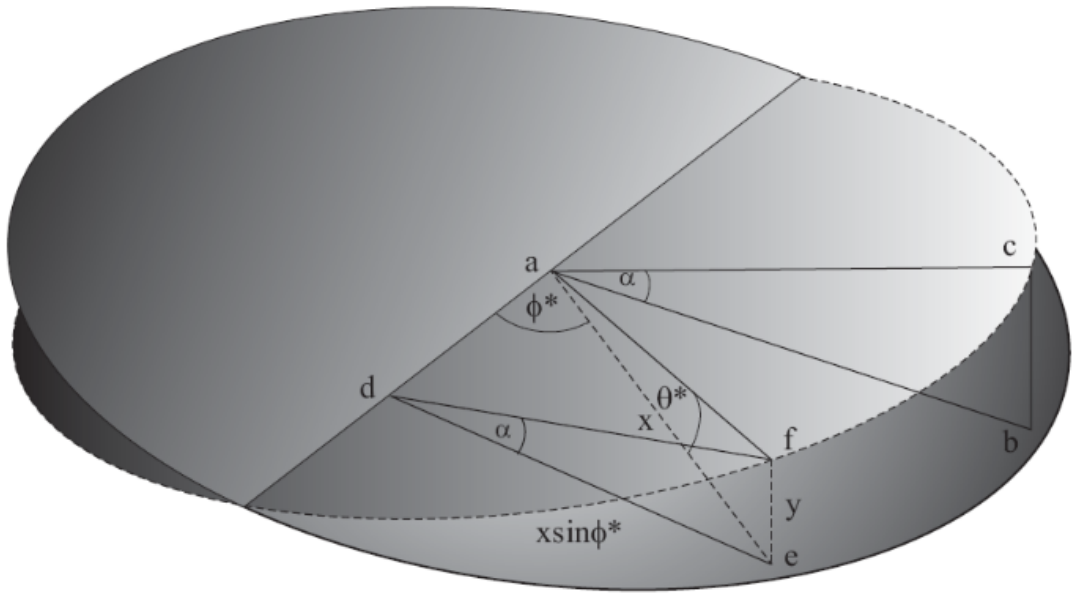

Figure 2.14: *The solid circle is in equatorial plane of the Sun. The dashed circle denotes the position of neutral line on some source surface and the tilt angle is* α*. The triangle* afd *on the tilted plane is projected onto the equatorial plane as* aed*. The lines* cb *and* fe *are perpendicular to the equatorial plane. The lines* ab *and* de *are parallel and both are perpendicular to the intersection of the two planes [Burger 2014, private communication].*

in the figure denotes the solar magnetic equator, the neutral line from which the current sheet emanates in this model. From this figure

$$\frac{y}{x \sin \phi^*} = \tan \alpha. \tag{2.6}$$

But

$$\frac{y}{x} = \tan \theta^*, \tag{2.7}$$

therefore

$$\tan \theta^* = \tan \alpha \sin \phi^*. \tag{2.8}$$

Here θ^* denotes the heliographic latitude of the neutral line, which will define the current sheet as one follows the plasma being blown radially away from the Sun. The question now is where a given angular displacement θ^* will map to at a distance r from the Sun in the co-rotating system. This displacement is frozen into the radial solar wind, and will take a time Ω/V_{sw} to cover this distance. During this time, the angular displacement θ^*

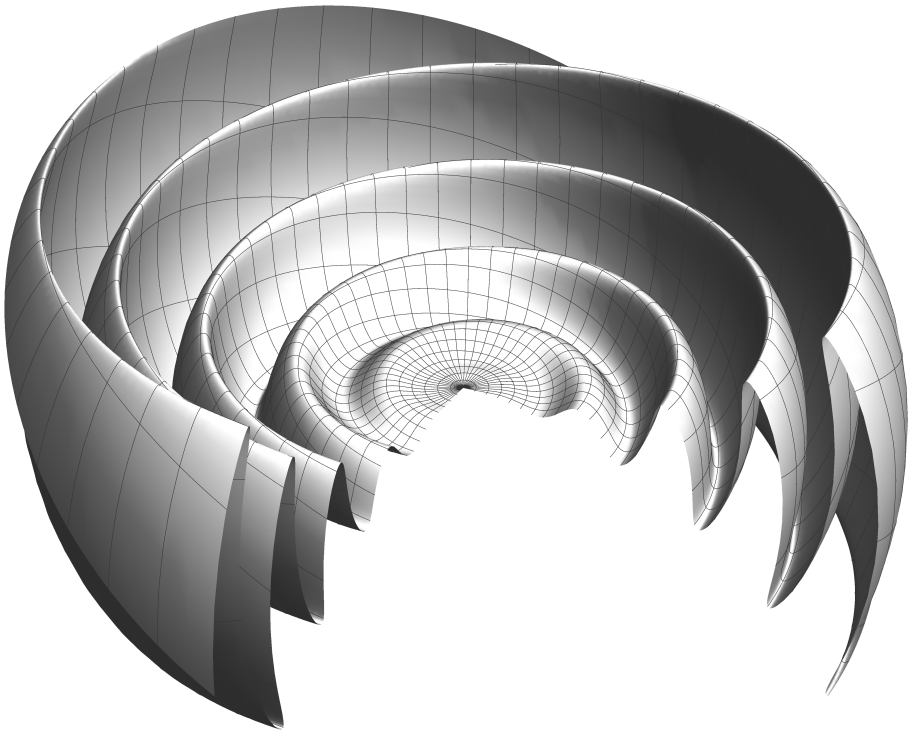

Figure 2.15: *Heliospheric current sheet, for a tilt angle of 20°, up to a radial distance of 30 AU. A section of the sheet has been removed to accentuate its wavy structure [Burger 2015, private communication].*

will have rotated through an angle $\Omega r/V_{sw}$, so that the angle ϕ at which it originated at the Sun, and at which it is observed at r, is related to its present azimuthal angle ϕ^* by

$$\phi^* = \phi + \frac{\Omega r}{V_{sw}}. \tag{2.9}$$

A fixed observer at position (r, ϕ) will see the Sun rotating counter-clockwise such that

$$\phi^* = \phi - \phi_0 - \Omega t + \frac{\Omega r}{V_{sw}}, \tag{2.10}$$

with ϕ_0 the angular displacement between the two system at $t = 0$. If α is small then θ^* is small and we can write

$$\sin\theta^* = \sin\alpha \sin\phi^*, \tag{2.11}$$

or

$$\theta^* = \sin^{-1}\left[\sin\alpha \sin\left(\phi + \frac{\Omega r}{V_{sw}}\right)\right]. \tag{2.12}$$

In terms of the polar angle $\theta = \pi/2 - \theta^*$ we have that

$$\theta = \frac{\pi}{2} - \sin^{-1}\left[\sin\alpha \sin\left(\phi + \frac{\Omega r}{V_{sw}}\right)\right]. \tag{2.13}$$

Alternatively, $\sin(\pi/2 - \theta) = \sin\alpha \sin\phi^*$, which leads to $\cos\theta = \sin\alpha \sin\phi^*$. In general,

$$\theta = \frac{\pi}{2} - \tan^{-1}\left[\tan\alpha \sin\left(\phi + \frac{\Omega r}{V_{sw}}\right)\right]. \tag{2.14}$$

This current sheet is shown in Figure 2.15 for a tilt angle of 20°.

Figure 2.16 shows observations of the tilt angle using two different models to compute it from solar magnetic field maps [*Hoeksema*, 1992], the "classic" and the new "radial" model. To compute the tilt angle, the "classic" model uses a line-of-sight boundary conditions, with a source surface at 2.5 solar radii, while the new "radial" model uses the radial boundary conditions at the photosphere, with a source surface at 3.5 solar radii. From these models it follows that the tilt angle varies from a minimum value of ∼5° during solar minimum periods to an upper limit of ∼75° during solar maximum periods, the latter value being a limitation of the observation technique. Note that data are only available as from mid-1976. This is obviously a restriction for studies of long-term cosmic-ray modulation that require observed tilt angles as input, such as the present one.

The HCS potentially has a significant effect on cosmic-ray transport in the heliosphere because particles can drift along it, and under certain conditions it can provide easy access into the inner heliosphere. The significance of cosmic-ray drift was pointed out by e.g. *Jokipii et al.* [1977], *Potgieter* [1984] and *Potgieter and Moraal* [1985]. Detailed discussions of cosmic-ray drifts are given in Chapters 3 and 4.

2.7 Classification And Transport Of Cosmic Rays

First detected on Earth by ionisation chambers, and later confirmed to be of extraterrestrial origin, cosmic rays are mostly fully ionised highly energetic particles with kinetic energies ranging from about 10^6 eV to as high as 10^{26} eV. Those particles that arrive at Earth are composed of 98 % fully ionised nuclei, primarily protons, and 2 % electrons and positrons. Within the heliosphere, cosmic rays of different origins are identified, and can be classified into four main populations:

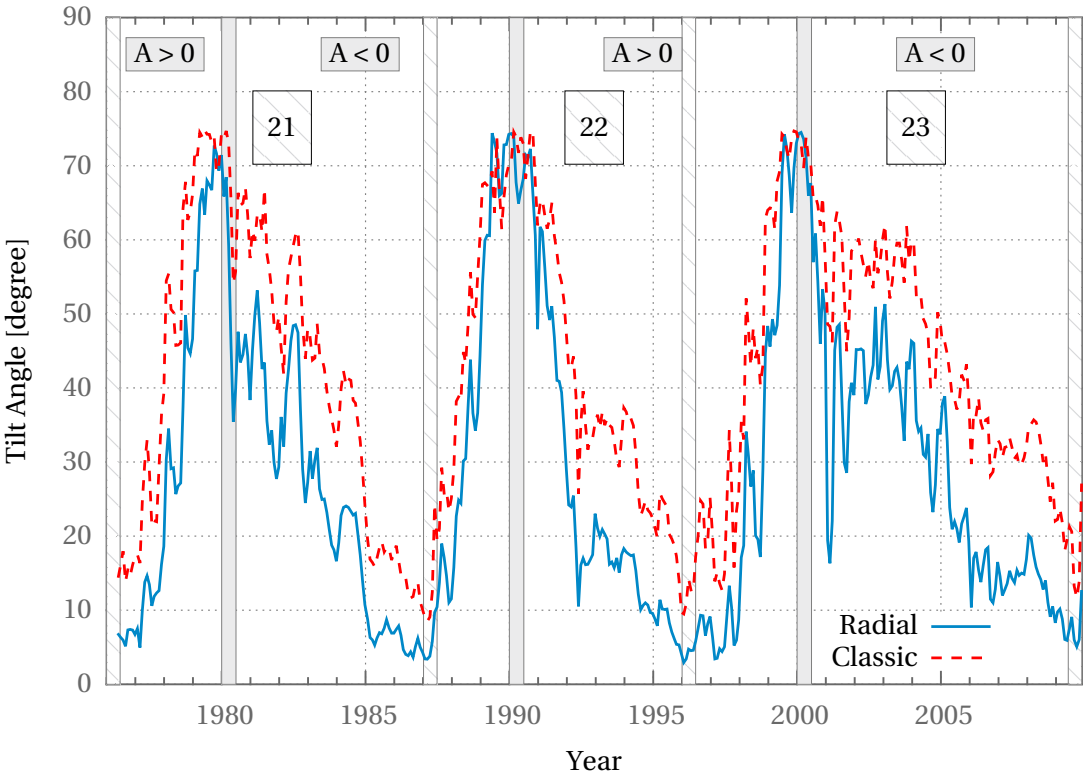

Figure 2.16: *Two different models for the tilt angle α. The "classic" uses a line-of-sight boundary condition at the photosphere and includes a significant polar field correction. The newer, possibly more accurate "radial" model uses a radial boundary condition at the photosphere, and requires no polar field correction. The dark and light shaded areas represent the periods where there were not well defined HMF polarities and the start and end of solar cycles, respectively. Tilt angle data from* `http://wso.stanford.edu/Tilts.html`.

1. Galactic cosmic rays (GCRs): this population enters the heliosphere almost isotropically from interstellar space. They are believed to be accelerated by shocks in the galaxy (like supernova remnants, pulsars, and active galactic nuclei) to very high energies [*Axford*, 1981; *Busching and Potgieter*, 2008; *Fisk and Gloeckler*, 2012]. GCRs are considered to be particles with energies up to 10^{15} eV. Above this energy, they are believed to originate from extragalactic sources [see, e.g., *Schlaepfer*, 2003; *Aharonian et al.*, 2012]. In this work we are only interested in the modulation of GCRs.

2. Solar energetic particles (SEPs): these particles are of solar origin. They are accelerated mainly by solar flares, coronal mass ejections and shocks in the interplanetary medium. They have energies up to several hundred MeV but can only be observed at Earth for periods varying from hours to a few days at a time, mainly during times of maximum solar activity periods [see, e.g., *Forbush*, 1946; *Balogh et al.*, 2008; *Cliver*, 2008; *Grechnev et al.*, 2008; *Usoskin*, 2008].

3. Anomalous cosmic rays (ACRs): these cosmic rays are formed due to the ionisation of interstellar neutral gas relatively close to the Sun. Neutral particles are ionised by photo-ionisation or by charge exchange and then the new-born ions (called pick-up ions) are transported to the outer heliosphere. There they are believed to be accelerated at the solar wind termination shock to become ACRs that can then enter the heliosphere [see, e.g., *Fisk et al.*, 1974; *Fichtner*, 2001; *Florinski*, 2009; *Gloeckler et al.*, 2009; *Potgieter*, 2010; *Strauss et al.*, 2010].

4. Jovian electrons: these energetic electrons are continuously emitted into interplanetary space at a heliocentric radial distance of ∼5 AU by Jupiter's magnetosphere, and were discovered during the Jupiter fly-by of the *Pioneer 10* spacecraft in 1973. The Jovian magnetosphere is a relatively strong source of electrons with energies up to ∼30 MeV. They are observed at Earth and up to ∼10 AU from the Sun [see, e.g., *Ferreira et al.*, 2001; *Ferreira*, 2005; *Heber and Potgieter*, 2006, 2008; *Dunzlaff et al.*, 2010].

When cosmic rays enter the heliosphere, their transport is governed by four modulation processes, namely (1) convection, due to the radially expanding solar wind, (2) energy changes due to adiabatic cooling, as well as continuous acceleration like heating or stochastic acceleration and diffusive shock acceleration, (3) diffusion due to the turbulent HMF, and (4) drift due to gradients and curvatures in HMF or any abrupt changes in the field direction [see, e.g., *Potgieter*, 1984; *Ferreira*, 2002; *Langner*, 2004; *Strauss*, 2010]. The basic equation that describes the spatial- and time evolution of the cosmic-ray distribution function in the heliosphere is the Parker transport equation [*Parker*, 1965], given by

$$\frac{\partial f_0(\mathbf{r},p,t)}{\partial t} = \nabla\cdot(\mathbf{K}\cdot\nabla f_0(\mathbf{r},p,t)) - \mathbf{V}_{sw}\cdot\nabla f_0(\mathbf{r},p,t) + \frac{1}{3}\left(\nabla\cdot\mathbf{V}_{sw}\right)\frac{\partial f_0(\mathbf{r},p,t)}{\partial \ln p} + Q. \quad (2.15)$$

Here $f_0(\mathbf{r},p,t)$ is the omnidirectional cosmic-ray distribution function in terms of particle momentum p, and Q is a function denoting cosmic ray sources within the heliosphere itself, set to zero when only galactic cosmic rays are considered. The solar wind velocity is denoted by $\mathbf{V}_{sw}$ and $\mathbf{K}$ is the cosmic-ray diffusion tensor. The term $\mathbf{V}_{sw}\cdot\nabla f_0(\mathbf{r},p,t)$ describes the outward convection of cosmic-rays by the solar wind, whereas the term $1/3\left(\nabla\cdot\mathbf{V}_{sw}\right)\partial f_0(\mathbf{r},p,t)/\partial\ln p$ describes adiabatic energy changes the cosmic rays experience within the heliosphere. The remaining term, $\nabla\cdot(\mathbf{K}\cdot\nabla f_0(\mathbf{r},p,t))$, describes both cosmic-ray drift and diffusion.

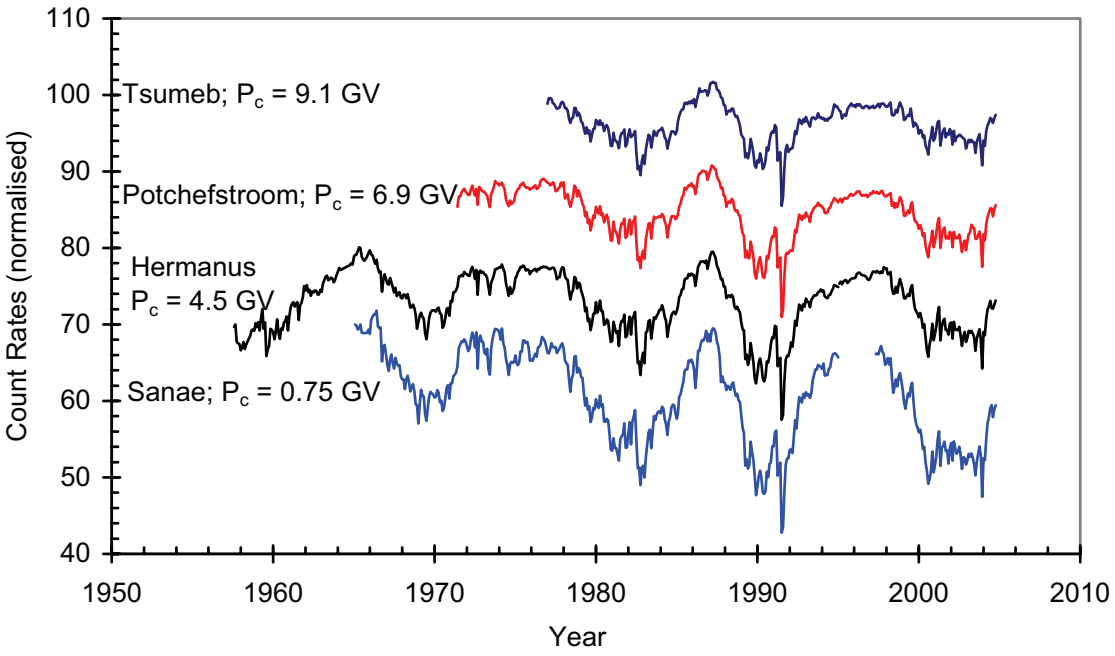

Figure 2.17: *Monthly counting rate of the neutron monitors at Sanae, Hermanus, Potchefstroom and Tsumeb normalised to March 1987 [Krüger, 2006].*

2.8 Cosmic-Ray Observations

There are two basic types of detectors for cosmic rays. Ground-based neutron monitors, developed by J. A. Simpson between 1948 - 1951, mainly record secondary showers in the atmosphere caused by incoming cosmic rays [*Simpson*, 2000]. Spacecraft-born detectors use mass and isotope spectrometers to measure particle composition and energy spectra.

When cosmic rays enter the Earth's atmosphere, they collide with atmospheric molecules and produce showers of secondary particles. Neutron monitors do not actually detect the primary cosmic rays, they detect these secondary particles. These detectors are sensitive and yield a high counting rate. Because of their basic simplicity they are fairly inexpensive to operate. They are used in a worldwide network for the study of long-term temporal variations, as well as short-term intensity changes [see, e.g., *McDonald*, 2000; *Krüger*, 2006]. Figure 2.17 shows the monthly averaged measurements of the four neutron monitors that are operated by the Centre For Space Research at the North-West University in Potchefstroom, South Africa. The long-term and short-term variations are clearly evident in counting rates. Long-term variations will be discussed in much more detail in the chapters to follow.

First launched in the late 50's and early 60's, spacecraft-born detectors provided new insights into the extraterrestrial environment. Numerous space missions since then have provided us with *in situ* observations that are crucial to understand and model the

structure and properties of the heliosphere and the particles that traverse it. In this work observations of the magnetic field, solar wind and cosmic-ray intensities are used, and a short description of selected spacecraft missions which are of importance to this study follows:

The *IMP 8* Mission

Launched in 1973, the *IMP 8* (International Monitoring Platform) spacecraft was the last in a series of ten proposed *IMP* missions to observe the Earth and Sun environments. There are three plasma experiments, a magnetometer and several energetic particle experiments on-board *IMP 8*. The *IMP 8* mission was officially terminated by NASA in 2001 [*Lockwood and Webber*, 1992; *Webber and Lockwood*, 1995; *Richardson et al.*, 2007; *Ahluwalia and Lopate*, 2007].

The *ACE* Mission

ACE (Advanced Composition Explorer) was launched by NASA in 1997. It carries six high-resolution sensors and three monitoring instruments, sampling low-energy particles of solar origin and high-energy galactic particles. Due to its array of instruments, *ACE* provides a prime view of the solar wind, interplanetary magnetic field and higher energy particles accelerated by the Sun, as well as particles accelerated in the heliosphere and the galactic regions beyond. *ACE* also provides near real-time continuous coverage of solar wind parameters and solar energetic particle intensities relevant to studies of space weather.

The *Voyager* Interstellar Mission

The *Voyager* Interstellar Mission consists of two spacecraft, launched about two weeks apart in 1977. *Voyager 1* and *Voyager 2* are exploring the northern and southern hemispheres of the heliosphere, respectively. They were intended to investigate the solar system beyond the neighbourhood of the outer planets to the outer heliosphere and possibly into the Local Interstellar Medium (LISM). A number of scientific instruments on-board the *Voyagers* are now defective and a few more have been switched off to save energy. *Voyager 1* crossed the solar wind termination shock in the northern hemisphere on December 2004 at a distance of 94 AU from the Sun and *Voyager 2* crossed in the southern hemisphere at 84 AU in August 2007, 10 AU closer to the Sun than *Voyager 1* [*Decker et al.*, 2005; *Stone et al.*, 2005; *Richardson et al.*, 2008; *Stone et al.*, 2008]. On 25 August 2012, at a distance of 121.7 AU from the Sun, *Voyager 1* recorded a sudden decrease in the intensity of low-energy protons and helium nuclei. At the same time, the intensity of galactic protons, helium, and electrons started to increase, and then remained essentially constant. *Webber and McDonald* [2013] argue that the suddenness of the changes is an indication that the spacecraft may have crossed the boundary

between the heliosphere and interstellar space. There is now little doubt that *Voyager 1* has indeed entered the LISM [see, e.g. *Burlaga et al.*, 2015]. The two *Voyager* spacecraft have travelled farther from Earth than any other human-made object, and are expected to be operational until 2020 [*Gurevitz*, 2005].

2.9 Summary

The purpose of this introductory chapter is to provide some context for the present study. In what follows, the focus is on the heliospheric current sheet and modulation. We will make extensive use of the theoretical description of the current sheet and observations related to it as outlined in Section 2.6. The cosmic-ray transport equation (Equation 2.15), in a slightly different form, will be used to model cosmic-ray modulation.

CHAPTER 3

Theoretical Description Of Cosmic-Ray Drift In The Heliosphere

3.1 Introduction

In the previous chapter, it has been shown that long-term neutron monitor observations of cosmic rays indicate periodicities in particle intensity of around 11 years and also around 22 years. It has also been indicated that the latter periodicity, the same as that of the heliospheric magnetic field and about twice that of solar activity, suggests that a charge-sign dependent transport process occurs. Since gradient- and curvature drifts depend on the charge of the particle, they are usually assumed to be the leading (and typically the only) cause of charge-sign dependent modulation [see, e.g., *Fisk et al.*, 1998].

When dealing with drifts in the heliosphere, the following needs to be taken note of: Firstly, cosmic rays that reach Earth can come from any direction, and their distribution function in phase space is expected to be nearly isotropic [see, e.g., *Jokipii and Parker*, 1970]. Secondly, there are significant gradients in the magnetic field, especially at the current sheet [see, e.g., *Jokipii et al.*, 1977], that affect drifts. Thirdly, it is not yet known how the drift coefficient, which characterises drift similar to how a diffusion coefficient characterises diffusion, is affected by turbulence [*Engelbrecht and Burger*, 2015].

In this chapter the approaches of *Burger et al.* [1985], *Burger* [1987, 2012], and references in these papers, are largely followed to derive an expression for drift of a nearly isotropic particle distribution in a heliosphere that includes a wavy current sheet. In the

derived expressions, a drift coefficient appears. Its form is well-known in the absence of turbulence [see, e.g., *Fisk et al.*, 1998], but as indicated above, a form for it when turbulence is taken into account, is currently a matter of debate, and a choice will be made in Chapter 4.

In the first section that follows, the case of a flat current sheet is discussed and it is shown that the drift velocity along it is finite, and also that the drift speed away from the current sheet cannot exceed the particle speed when viewed on the scale of a Larmor radius. A general expression for drift velocity along a wavy current sheet is derived, which is then discussed in some detail in the following section. Note that the term "neutral sheet" is often used instead of "current sheet". The former term reflects that the field is zero along the surface across which it changes direction, while the latter term reflects the fact that currents are needed to set up such a field.

3.2 Drift In The Presence Of A Current Sheet

A magnetic field that switches sign across a current sheet at $\theta = \theta_{\rm ns}$ can be represented as

$$\mathbf{B} = \mathbf{B}_m \left[1 - 2H\left(\theta - \theta_{\rm ns}\right)\right], \tag{3.1}$$

where $\mathbf{B}_m$ is the magnetic field on one side of the current sheet and H is the Heaviside step function defined by *Abramowitz and Stegun* [1972], as

$$H(x) = \begin{cases} 0 & x < 0 \\ \dfrac{1}{2} & x = 0 \\ 1 & x > 0 \end{cases}, \tag{3.2}$$

such that $\mathbf{B} = +\mathbf{B_m}$ if $\theta < \theta_{\rm ns}$, $\mathbf{B} = -\mathbf{B_m}$ if $\theta > \theta_{\rm ns}$, and $\mathbf{B} = 0$ if $\theta = \theta_{\rm ns}$. The change in direction in the field will have a major effect on the particle. The fact that it crosses a surface where the field is zero will by itself have virtually no effect, as the particle spends only an infinitesimally small time exactly at this surface. One can therefore assume that

$$B = |\mathbf{B}| \equiv |\mathbf{B}_m| = B_m. \tag{3.3}$$

The general expression for the drift velocity of a nearly-isotropic particle distribution is given by [see, e.g., *Isenberg and Jokipii*, 1979]

$$\mathbf{v}_D = \nabla \times \kappa_A \mathbf{e}_B. \tag{3.4}$$

In the case when scattering due to turbulence can be neglected, the so-called weak-scattering coefficient becomes [see, e.g., *Fisk et al.*, 1998]

$$\kappa_A = \frac{v R_L}{3}, \tag{3.5}$$

where is v the particle speed, $R_L = \frac{p}{qB} = \frac{P}{cB}$ is the Larmor radius with $P = \frac{pc}{q}$ the particle rigidity (such that $\kappa_A = \frac{vp}{3qB} = \frac{\beta P}{3B}$ with $\beta = \frac{v}{c}$), and $\mathbf{e}_B$ is a unit vector in the direction of the magnetic field. Substituting Equation 3.1 into Equation 3.4, and using the vector identity $\nabla \times \phi\mathbf{A} = \phi\nabla \times \mathbf{A} + \nabla\phi \times \mathbf{A}$, yields [see, e.g., *Hattingh*, 1998]

$$\begin{aligned}
\mathbf{v}_D &= \nabla \times \kappa_A \mathbf{e}_B \\
&= \nabla \times \left(\kappa_A \frac{\mathbf{B}_m}{B} \left[1 - 2\mathrm{H}(\theta - \theta_{\mathrm{ns}})\right] \right) \\
&\equiv \nabla \times \left(\kappa_A \frac{\mathbf{B}_m}{B_m} \left[1 - 2\mathrm{H}(\theta - \theta_{\mathrm{ns}})\right] \right) \\
&= \left(\nabla \times \kappa_A \frac{\mathbf{B}_m}{B_m} \right) \left[1 - 2\mathrm{H}(\theta - \theta_{\mathrm{ns}})\right] \\
&\quad + 2\delta(\theta - \theta_{\mathrm{ns}}) \kappa_A \frac{\mathbf{B}_m}{B_m} \times \nabla(\theta - \theta_{\mathrm{ns}}).
\end{aligned} \tag{3.6}$$

The first term of the last line of Equation 3.6 represents gradient and curvature drift away from the current sheet, which switches sign across the sheet. The second term represents drift along current sheet. The Dirac delta function was originally interpreted literally as meaning an infinitely fast drift along the current sheet. This is in fact not the case, but to see this requires a further analysis.

Consider now a flat current sheet at $\theta_{ns} = \frac{\pi}{2}$, and a Parker magnetic field, with unit vector $\mathbf{e}_{BM} = \cos\psi \mathbf{e}_r - \sin\psi \mathbf{e}_\phi$ (i.e. $\mathbf{e}_B = \cos\psi \mathbf{e}_r - \sin\psi \mathbf{e}_\phi$ is above the sheet and $\mathbf{e}_B = -\cos\psi \mathbf{e}_r + \sin\psi \mathbf{e}_\phi$ below it). Here ψ is the spiral angle, defined here without the source surface radius that appears in Equation 2.2, as $\tan\psi = r \sin\theta \frac{\Omega}{V_{sw}}$. We assume that the field can be considered to be uniform on the scale of a particle Larmor radius. In general, for a wavy current sheet we have that the vector normal to it is given by

$$\nabla(\theta - \theta_{ns}) = -\frac{\partial \theta_{ns}}{\partial r}\mathbf{e}_r + \frac{1}{r}\mathbf{e}_\theta - \frac{1}{r\sin\theta}\frac{\partial \theta_{ns}}{\partial \phi}\mathbf{e}_\phi, \tag{3.7}$$

and in this case of a flat sheet only the second term is not zero. In the case where scattering can be neglected, the second term of Equation 3.6, denoted by $\mathbf{v}_{Dns}$, becomes

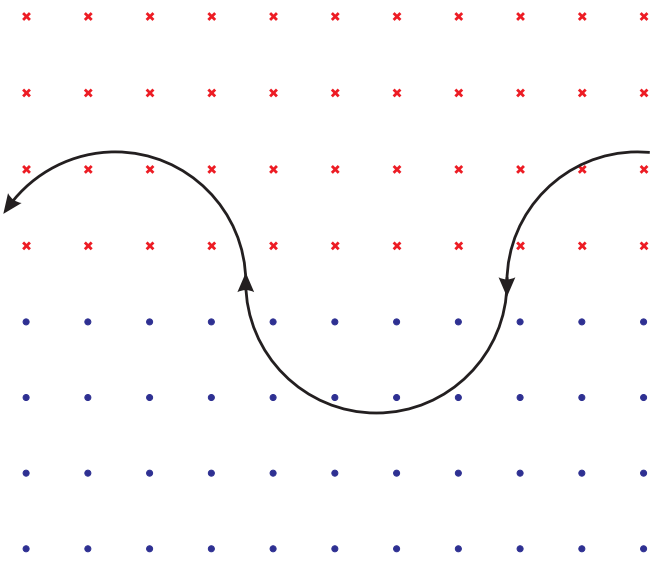

Figure 3.1: *Drift of a positively charged particle along a (flat) current sheet. The dots and crosses indicate the outwards and inwards directions of the magnetic field, respectively.*

$$\begin{aligned}\mathbf{v}_{Dns} &= 2\delta(\theta-\frac{\pi}{2})\kappa_A \mathbf{e}_{BM}\times\nabla(\theta-\frac{\pi}{2}) \\ &= 2\delta(\theta-\frac{\pi}{2})\frac{vR_L}{3}\left(\cos\psi\mathbf{e}_r-\sin\psi\mathbf{e}_\phi\right)\times\left(\frac{1}{r}\mathbf{e}_\theta\right) \\ &= 4\frac{R_L}{r}\delta(\theta-\frac{\pi}{2})\frac{v}{6}\left(\sin\psi\mathbf{e}_r+\cos\psi\mathbf{e}_\phi\right).\end{aligned} \tag{3.8}$$

It is easy to see graphically that a particle will drift along a flat current sheet with a finite speed, as shown in Figure 3.1. Clearly, there is no reason why the drift speed should be infinitely large; in fact, it has to be smaller than the particle speed. The approach of Burger and co-workers is to view drifts from the particle perspective and not to resort to using guiding centres. In the latter case the guiding centre jumps instantaneously from one position to the next. Drift speeds are here calculated for some distribution of particles consistent with the fact that the cosmic-ray transport equation is solved for particle phase space density and not for that of guiding centres.

Physically the drift along a current sheet affects particles that are up to two Larmor radii away from the neutral plane where the field switches direction. We now calculate the average value of the drift velocity (Equation 3.8) across a surface in the (θ, ϕ)-plane at a fixed radial distance, keeping in mind that this drift only occurs over a limited range of polar angles. The angle $\Delta\theta_{ns}$ subtending $2R_L$ at a distance r follows from $\tan\left(\frac{\Delta\theta_{ns}}{2}\right)=\frac{R_L}{r}$ and since typically $\frac{R_L}{r}\ll 1$ for the heliosphere where we apply our results, we have that

$$\Delta\theta_{ns} \simeq \frac{2R_L}{r}. \tag{3.9}$$

The average of the magnitude of the current sheet drift velocity then is [*Burger*, 1987]

$$\begin{aligned}\langle \mathrm{v}_{Dns}\rangle_{\theta,\phi} &= \frac{1}{2\pi r}\frac{1}{4R_L}\int_0^{2\pi} r\; d\phi \int_{\frac{\pi}{2}-\Delta\theta_{ns}}^{\frac{\pi}{2}+\Delta\theta_{ns}} 4\frac{R_L}{r}\delta(\theta-\frac{\pi}{2})\frac{v}{6}\; r\; \sin\theta d\theta \\ &= \frac{v}{6}.\end{aligned} \tag{3.10}$$

A Dirac function by itself lacks physical significance. As the above result shows, when a suitable average is calculated, it becomes clear that the average drift speed of a particle, viewed on the scale of a Larmor radius, is indeed less than the particle speed. As an aside, note that the average over ϕ is actually superfluous because the drift is independent of azimuth, and we get exactly the same result when the integration over ϕ is neglected:

$$\begin{aligned}\langle \mathrm{v}_{Dns}\rangle_{\theta} &= \frac{1}{4R_L}\int_{\frac{\pi}{2}-\Delta\theta_{ns}}^{\frac{\pi}{2}+\Delta\theta_{ns}} 4\frac{R_L}{r}\delta(\theta-\frac{\pi}{2})\frac{v}{6}\; r\; d\theta \\ &= \frac{v}{6}.\end{aligned} \tag{3.11}$$

We now return to the gradient- and curvature drift term in Equation 3.6. If the scale length for changes in the magnetic field is smaller than the particle's Larmor radius, the local, instantaneous drift velocity is not necessarily physically meaningful. The particle must be allowed to complete a full gyration and therefore sample the field conditions over its entire orbit before the actual drift velocity will become apparent. When the average drift speed is viewed on the scale of a Larmor radius one can easily show that the average drift speed is less than the particle's speed. Note that the following derivations contain an assumption of weak scattering. It seems reasonable to assume that the presence of turbulence will actually reduce drift speeds [see, e.g., *Minnie et al.*, 2007a], and the derivation therefore represents an extreme scenario.

Consider a spherical volume V of radius $R_{\max}$, where $R_{\max}$ is the maximum Larmor radius that any particle initially inside a volume element d^3x will acquire during its completion of a gyration. This implies that

$$R_{\max} = \frac{p}{qB_{\min}} \tag{3.12}$$

where $B_{\min}$ is the minimum value of the magnetic field within the volume V. If $R_{\max}$ must be finite, this requires that the field is not allowed to change direction inside this volume. Let $\mathbf{w}$ be the average value of the drift velocity throughout the volume V. Then

$$\begin{aligned}\mathbf{w} &= \frac{3}{4\pi R_{\max}^3}\int_V \langle \mathbf{v}_D\rangle_\Omega dV \\ &= \frac{3}{4\pi R_{\max}^3}\int_V \frac{pv}{3q}\nabla\times\left(\frac{\mathbf{B}}{B^2}\right)dV \\ &= \frac{3}{4\pi R_{\max}^3}\int_S \frac{pv}{3q}d\mathbf{S}\times\left(\frac{\mathbf{B}}{B^2}\right),\end{aligned} \tag{3.13}$$

where $\mathbf{S}$ is the spherical surface that bounds the volume V. Now, if θ is the angle between $\mathbf{B}$ and $d\mathbf{S}$ on the surface,

$$\begin{aligned}\left|\int_S d\mathbf{S}\times\left(\frac{\mathbf{B}}{B^2}\right)\right| &= \int_S \sin\theta\left(\frac{dS}{B}\right) \\ &\le \frac{1}{B_{\min}}\int_S \sin\theta dS \\ &= \frac{R_{\max}^2}{B_{\min}}\int_S \sin\theta d\Omega \\ &= \frac{R_{\max}^2}{B_{\min}}\int_0^{\pi}\int_0^{2\pi}\sin\theta d\theta d\phi \\ &= \frac{\pi^2 R_{\max}^2}{B_{\min}}.\end{aligned} \tag{3.14}$$

Therefore

$$\begin{aligned}|\mathbf{w}| &\le \frac{3}{4\pi R_{\max}^3}\frac{pv}{3q}\frac{\pi^2 R_{\max}^2}{B_{\min}} \\ &= \frac{\pi}{4}v.\end{aligned} \tag{3.15}$$

This derivation is given in *Burger* [1987] and is a variation of one by *Isenberg and Jokipii* [1979], who obtain a slightly different result since they consider a surface area rather than a volume.

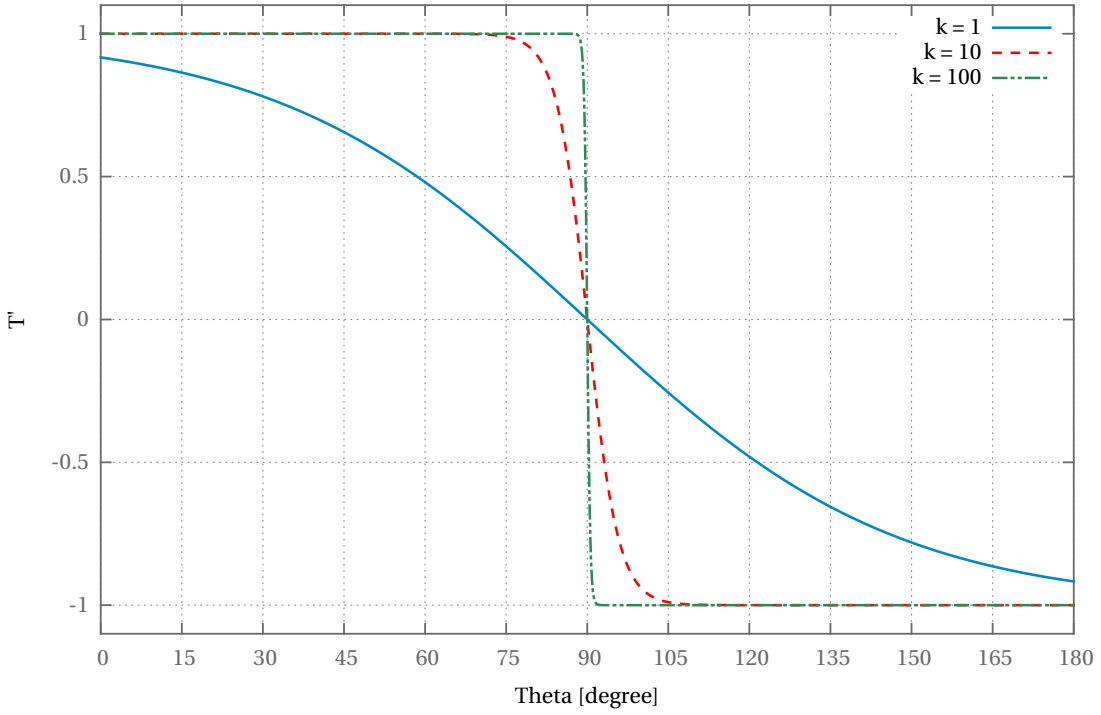

Figure 3.2: *The function* $T' = \tanh\left[k\left(\frac{\pi}{2} - \theta\right)\right]$ *as function of* θ *for* $k = 1, k = 10$ *and* $k = 100$.

3.2.1 Implementing Drift Expressions For A Generic Current Sheet

To avoid numerical instabilities in grid-based finite difference methods, the Heaviside step function must be replaced by a smooth transition. In this case we use a function $\tanh\left[k\left(\theta_{ns} - \theta\right)\right]$ (shown in Figure 3.2) to replace $\left[1 - 2H\left(\theta - \theta_{ns}\right)\right]$. Note that the order of θ and θ_{ns} is changed, and that for increasing values of k the transition function becomes more like the Heaviside function. Technically, we have to argue that we replace κ_A with $\kappa_A \tanh\left[k\left(\theta_{ns} - \theta\right)\right]$ as in Equation 3.6, rather than using Equation 3.1 with $\tanh\left[k\left(\theta_{ns} - \theta\right)\right]$ replacing $\left[1 - 2H\left(\theta - \theta_{ns}\right)\right]$. For the latter case we will get a completely different result. By replacing κ_A with $\kappa_A \tanh\left[k\left(\theta_{ns} - \theta\right)\right]$ in Equation 3.4 we ensure that the drift velocity field is divergence free. For reasons that will become clear later, we also multiply the argument of the hyperbolic tangent function with a term $\cos\nu$, so that

$$\kappa_A \rightarrow \kappa_A \tanh[k\left(\theta_{\mathrm{ns}} - \theta\right)\cos\nu] \tag{3.16}$$

with ν the angle between the normal to the current sheet and the θ-direction. There is no *a priori* reason against this as the drift velocity field remains divergence-free. With

this assumption, the drift velocity in Equation 3.4 for the case of a generic wavy current sheet becomes [*Burger*, 2012]

$$\begin{aligned}\mathbf{v}_D &= \nabla \times \kappa_A \mathbf{e}_B \\ &= \left(\nabla \times \kappa_A \frac{\mathbf{B}_m}{B_m}\right) \tanh\left[k\left(\theta_{\rm ns}-\theta\right)\cos\nu\right] \\ &\quad - \frac{k\cos\nu}{\cosh^2\left[k\left(\theta_{\rm ns}-\theta\right)\cos\nu\right]} \kappa_A \frac{\mathbf{B}_m}{B_m} \times \nabla(\theta_{\rm ns}-\theta) \\ &\quad - \frac{k(\theta_{\rm ns}-\theta)}{\cosh^2\left[k\left(\theta_{\rm ns}-\theta\right)\cos\nu\right]} \kappa_A \frac{\mathbf{B}_m}{B_m} \times \nabla\cos\nu.\end{aligned} \tag{3.17}$$

The first term, which is zero at the current sheet, represents gradient and curvature drift away from the sheet, while the second term represents current sheet drift. The third term, which is zero at the current sheet, depends on the gradient of the $\cos\nu$ term, and will be discussed later.

Now, specifying a flat sheet at $\theta_{ns} = \frac{\pi}{2}$ and a Parker magnetic field, with a weak-scattering drift coefficient $\kappa_A = \frac{vR_L}{3}$, Equation 3.17 with $\cos\nu = 1$ becomes

$$\begin{aligned}\mathbf{v}_{Dns} &= -\frac{k}{\cosh^2\left[k\left(\frac{\pi}{2}-\theta\right)\right]} \frac{vR_L}{3} \left(\cos\psi\mathbf{e}_r - \sin\psi\mathbf{e}_\phi\right) \times \left(-\frac{\mathbf{e}_\theta}{r}\right) \\ &= \frac{2R_L}{r} \frac{k}{\cosh^2\left[k\left(\frac{\pi}{2}-\theta\right)\right]} \frac{v}{6} \left(\sin\psi\mathbf{e}_r + \cos\psi\mathbf{e}_\phi\right).\end{aligned} \tag{3.18}$$

To show that this equation gives approximately the same result as Equation 3.10 we perform the same average, and find

$$\begin{aligned}\langle \mathrm{v}_{Dns}\rangle_\theta &= \frac{1}{4R_L} \int_{\frac{\pi}{2}-\Delta\theta_{ns}}^{\frac{\pi}{2}+\Delta\theta_{ns}} \frac{2R_L}{r} \frac{k}{\cosh^2\left[k\left(\frac{\pi}{2}-\theta\right)\right]} \frac{v}{6}\, r d\theta \\ &\simeq -\frac{1}{2}\frac{v}{6} \tanh\left[k\left(\frac{\pi}{2}-\theta\right)\right]\Big|_{\frac{\pi}{2}-\Delta\theta_{ns}}^{\frac{\pi}{2}+\Delta\theta_{ns}} \\ &= \frac{v}{6}\tanh\left[k\Delta\theta_{ns}\right].\end{aligned} \tag{3.19}$$

The result in the second step is approximate: we neglect the θ-dependence of R_L in order to find a form that can easily be interpreted. This can be done provided that θ_{ns} is small enough, so that the difference between the exact and the approximate result is then only a few percent at the highest rigidity. Now, provided that the argument of the hyperbolic tangent function is large enough, the result will be approximately the same as Equation 3.10.

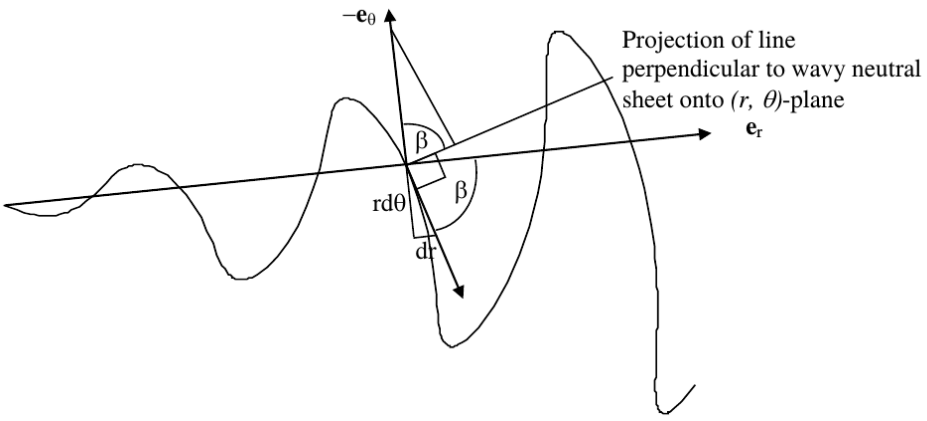

Figure 3.3: *A cut through the wavy current sheet in the* $(r,\ theta)$*-plane. Note that* $-\frac{\pi}{2} < \beta < \frac{\pi}{2}$*. In this figure* $\beta > 0$*.*

3.3 Wavy Current Sheet

We now consider the current sheet described in Section 2.6 and here provide details provided by the author that were not given explicitly in the published derivation of *Burger* [2012]. We first find the tangent to a cut through the wavy current sheet in the (r, θ)-plane, as shown in Figure 3.3. Clearly

$$\tan\beta = \frac{r\Delta\theta_{ns}}{\Delta r} \tag{3.20}$$

where $r\Delta\theta_{ns}$ is the infinitesimal distance in the θ-direction as r changes by Δr. The expression for the current sheet is given in Equation 2.14, repeated here for ease of reference:

$$\theta_{ns} = \frac{\pi}{2} - \tan^{-1}\left(\tan\alpha\sin\phi^*\right); \quad \phi^* = \phi + \phi_0 + r\frac{\Omega}{V_{sw}}. \tag{3.21}$$

It readily follows that

$$\begin{aligned}\tan\beta &= \frac{r\partial\theta_{ns}}{\partial r} \\ &= -\frac{r\dfrac{\Omega}{V_{sw}}\tan\alpha\cos\phi^*}{1+\tan^2\alpha\sin^2\phi^*},\end{aligned} \tag{3.22}$$

such that

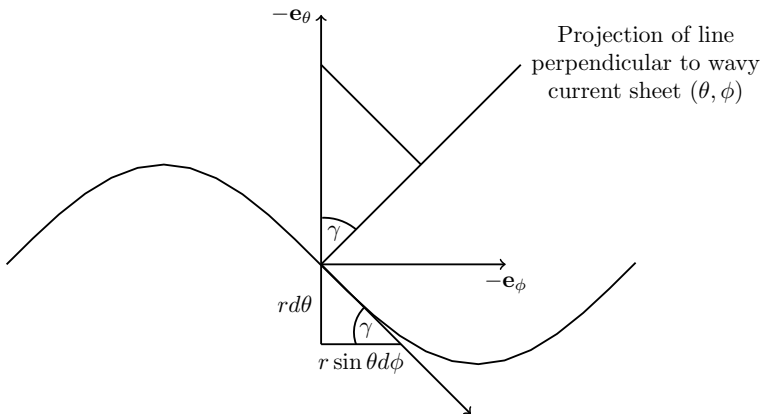

Figure 3.4: *A cut through the wavy current sheet in the (θ, ϕ)-plane. Note that $-\frac{\pi}{2} < \gamma < \frac{\pi}{2}$. In this figure $\gamma > 0$.*

$$\begin{aligned}\cos\beta &= \frac{1}{\sqrt{1+\tan^2\beta}} \\ &= \frac{1}{\sqrt{1+\dfrac{r^2(\Omega/V_{sw})^2\tan^2\alpha\cos^2\phi^*}{\left(1+\tan^2\alpha\sin^2\phi^*\right)^2}}}.\end{aligned} \tag{3.23}$$

For small values of the tilt angle, this reduces to

$$\cos\beta \approx \frac{1}{\sqrt{1+r^2\left(\dfrac{\Omega}{V_{sw}}\right)^2\alpha^2\cos^2\phi^*}} \tag{3.24}$$

in agreement with *Caballero-Lopez and Moraal* [2003]. We also need the tangent to a cut through the wavy current sheet in the (θ, ϕ)-plane, as shown in Figure 3.4. Again, it readily follows that

$$\tan\gamma = \frac{r\Delta\theta_{ns}}{r\sin\theta\Delta\phi}. \tag{3.25}$$

For a current sheet described by Equation 3.21, it follows that

$$\begin{aligned}\tan\gamma &= \frac{r\partial\theta_{ns}}{r\sin\theta\,\partial\phi} \\ &= -\frac{\tan\alpha\cos\phi^*}{\sin\theta\left(1+\tan^2\alpha\sin^2\phi^*\right)}.\end{aligned} \tag{3.26}$$

For a Parker field, the angles γ and β are related through the spiral angle ψ:

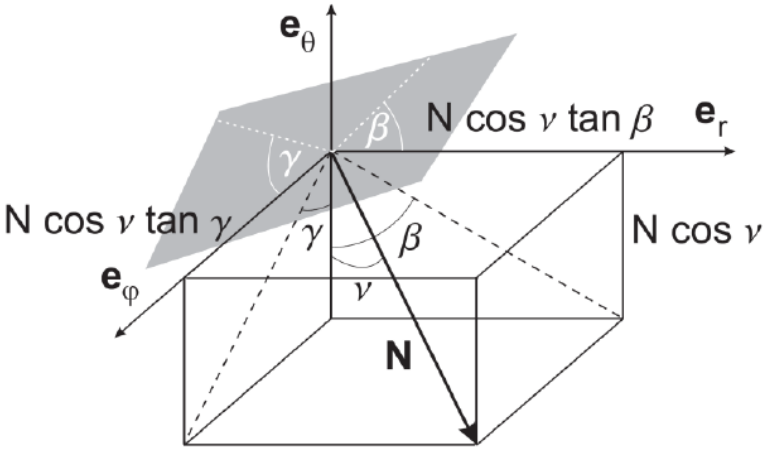

Figure 3.5: *Vector normal to the wavy current sheet* $\mathbf{N}$ *and its components in terms of* γ*,* β *and* ν*. Here all three angles are positive. The gray surface is tangential to* $\mathbf{N}$*, and the white dashed lines are intersections of this plane with* (θ, ϕ)*-plane and the* (r, θ)*-plane. Note that the white dashed line in each plane is perpendicular to the black dashed line in the same plane [Burger, 2012].*

$$\begin{aligned} \frac{\tan\beta}{\tan\gamma} &= r\sin\theta\frac{\Omega}{V_{sw}} \\ &\equiv \tan\psi. \end{aligned} \tag{3.27}$$

Note that since the right-hand side of Equation 3.27 is always positive, γ and β have the same sign. What we need is the angle between the normal $\mathbf{N}$ to the wavy current sheet and the θ-direction. From the left-hand panel of Figure 3.5 it follows that

$$\begin{aligned} \tan\nu &= \pm\sqrt{\tan^2\beta + \tan^2\gamma} \\ &= \pm\sqrt{\tan^2\beta + \frac{\tan^2\beta}{\tan^2\psi}} \\ &= \frac{\tan\beta}{\sin\psi} \end{aligned} \tag{3.28}$$

such that

$$\cos\nu = \frac{1}{\sqrt{1 + \tan^2\beta + \tan^2\gamma}}. \tag{3.29}$$

The drift velocity (for positively charged particles) is as usual given by Equation 3.17, repeated here for ease of reference:

$$
\begin{aligned}
\mathbf{v}_D &= \nabla \times \kappa_A \mathbf{e}_B \\
&= \left(\nabla \times \kappa_A \frac{\mathbf{B}_m}{B_m} \right) \tanh\left[k \left(\theta_{\rm ns} - \theta \right) \cos\nu \right] \\
&\quad - \frac{k \cos\nu}{\cosh^2\left[k \left(\theta_{\rm ns} - \theta \right) \cos\nu \right]} \kappa_A \frac{\mathbf{B}_m}{B_m} \times \nabla(\theta_{\rm ns} - \theta) \\
&\quad - \frac{k(\theta_{\rm ns} - \theta)}{\cosh^2\left[k \left(\theta_{\rm ns} - \theta \right) \cos\nu \right]} \kappa_A \frac{\mathbf{B}_m}{B_m} \times \nabla \cos\nu .
\end{aligned}
\tag{3.30}
$$

For a Parker field during an $A > 0$ solar polarity epoch, the second (current sheet drift) term becomes

$$
\begin{aligned}
\mathbf{v}_{Dns} &= -\frac{k \cos\nu}{\cosh^2\left[k \left(\theta_{\rm ns} - \theta \right) \cos\nu \right]} \kappa_A \\
&\quad \times \left(\cos\psi \mathbf{e}_r - \sin\psi \mathbf{e}_\phi \right) \left[\frac{\partial \theta_{ns}}{\partial r} \mathbf{e}_r - \frac{1}{r} \mathbf{e}_\theta + \frac{1}{r \sin\theta} \frac{\partial \theta_{ns}}{\partial \phi} \mathbf{e}_\phi \right] \\
&= \frac{k \cos\nu}{\cosh^2\left[k \left(\theta_{\rm ns} - \theta \right) \cos\nu \right]} \kappa_A \\
&\quad \times \left[\frac{\sin\psi}{r} \mathbf{e}_r + \left(\frac{\cos\psi}{r \sin\theta} \frac{\partial \theta_{ns}}{\partial \phi} + \sin\psi \frac{\partial \theta_{ns}}{\partial r} \right) \mathbf{e}_\theta + \frac{\cos\psi}{r} \mathbf{e}_\phi \right] \\
&= \frac{k \cos\nu}{r \cosh^2\left[k \left(\theta_{\rm ns} - \theta \right) \cos\nu \right]} \kappa_A \\
&\quad \times \left[\sin\psi \mathbf{e}_r + \left(\frac{\cos\psi}{\sin\theta} \frac{\partial \theta_{ns}}{\partial \phi} + r \sin\psi \frac{\partial \theta_{ns}}{\partial r} \right) \mathbf{e}_\theta + \cos\psi \mathbf{e}_\phi \right] \\
&= \frac{k \cos\nu}{r \cosh^2\left[k \left(\theta_{\rm ns} - \theta \right) \cos\nu \right]} \kappa_A \left[\sin\psi \, \mathbf{e}_r + \tan\nu \, \mathbf{e}_\theta + \cos\psi \, \mathbf{e}_\phi \right] \\
&= \frac{k}{r \cosh^2\left[k \left(\theta_{\rm ns} - \theta \right) \cos\nu \right]} \kappa_A \left[\sin\psi \cos\nu \, \mathbf{e}_r + \sin\nu \, \mathbf{e}_\theta + \cos\psi \cos\nu \, \mathbf{e}_\phi \right] .
\end{aligned}
\tag{3.31}
$$

The second-last step follows from the relation between ψ and the three angles γ, β and ν,

$$
\begin{aligned}
\frac{\cos\psi}{\sin\theta} \frac{\partial \theta_{ns}}{\partial \phi} + r \sin\psi \frac{\partial \theta_{ns}}{\partial r} &= \cos\psi \tan\gamma + \sin\psi \tan\beta \\
&= \cos\psi \frac{\tan\beta}{\tan\psi} + \sin\psi \tan\beta \\
&= \frac{\tan\beta}{\sin\psi} \\
&\equiv \tan\nu .
\end{aligned}
\tag{3.32}
$$

Note that neglecting the third term (gradient of the $\cos\nu$-term) in Equation 3.30, the term in square brackets in the last line of Equation 3.31 is a unit vector in the direction

of the current sheet drift velocity. Note also that no assumption about local flatness of sheet is made.

Finally then, the total drift velocity field for a nearly-isotropic particle distribution in the presence of a wavy current sheet is

$$\begin{aligned}\mathbf{v}_D &= \nabla \times \kappa_A \mathbf{e}_B \\ &= \left(\nabla \times \kappa_A \frac{\mathbf{B}_m}{B_m}\right) \tanh\left[k\left(\theta_{\text{ns}} - \theta\right)\cos\nu\right] \\ &\quad + \frac{k}{r\cosh^2\left[k\left(\theta_{\text{ns}} - \theta\right)\cos\nu\right]}\kappa_A \\ &\quad \times \left[\sin\psi\cos\nu\,\mathbf{e}_r + \sin\nu\,\mathbf{e}_\theta + \cos\psi\cos\nu\,\mathbf{e}_\phi\right].\end{aligned} \tag{3.33}$$

The meaning of the last term of Equation 3.30 neglected here, is not clear. It turns out that the cross product appearing in it has a θ-component only, and this component alternates between positive and negative values. Differences between the absolute values of the positive and negative peaks are most pronounced in the inner heliosphere but become negligible beyond about 10 AU. This drift therefore moves particles up and down in latitude but does not contribute significantly to the drift flux in a realistic sized heliosphere. It is therefore neglected. However, the magnitude of this term is often comparable to that of current sheet drift, a fact not stated in *Burger* [2012]. Whereas the meridional component of current sheet drift changes sign as the particles follow the contours of the current sheet, the $\nabla\cos\nu$ term changes sign at the peaks and troughs of the current sheet, and also where the meridional component of current sheet drift attains a maximum about half-way between peak and trough. If this drift is real and not just a mathematical artefact due to a less than perfect implementation of the current sheet, it would lead to interesting drift patterns close to the current sheet.

We can now show why the argument of the hyperbolic tangent in the expression 3.16 for κ_A required the $\cos\nu$ term. Without it, the result would have been

$$\begin{aligned}\widetilde{\mathbf{v}}_{Dns} &= \frac{k}{r\cosh^2\left[k\left(\theta_{\text{ns}} - \theta\right)\right]}\kappa_A\left[\sin\psi\,\mathbf{e}_r + \tan\nu\,\mathbf{e}_\theta + \cos\psi\,\mathbf{e}_\phi\right] \\ &= \frac{k}{r\cos\nu\cosh^2\left[k\left(\theta_{\text{ns}} - \theta\right)\right]}\kappa_A \\ &\quad \times \left[\sin\psi\cos\nu\,\mathbf{e}_r + \sin\nu\,\mathbf{e}_\theta + \cos\psi\cos\nu\,\mathbf{e}_\phi\right].\end{aligned} \tag{3.34}$$

The $\cos\nu$ in the denominator is problematic because it would lead to average drift speeds exceeding particle speed:

$$\begin{aligned}\langle \mathrm{v}_{Dns} \rangle_\theta &= \frac{1}{4R_L} \int_{\theta_{ns}-\Delta\theta_{ns}}^{\theta_{ns}+\Delta\theta_{ns}} R_L \frac{k}{r\cosh^2\left[k\left(\theta_{ns}-\theta\right)\right]\cos\nu} \frac{v}{3}\, r d\theta \\ &= \frac{v}{6\cos\nu} \tanh\left[k\Delta\theta_{ns}\right].\end{aligned} \tag{3.35}$$

3.4 Summary And Conclusions

In this chapter expressions that describe the gradient- and curvature drift experienced by a nearly-isotropic cosmic-ray distribution are derived [see also *Burger*, 2012]. The expressions are valid throughout a heliosphere that includes a wavy current sheet. They are easy to implement because they depend on only one angular distance from the current sheet, and have been shown to agree very well with published results [*Burger*, 2012]. A more realistic and accurate description of drift along and near a wavy current will almost certainly require single-particle simulations that would need enormous computing resources. In contrast, the numerical model used in the present study runs easily on a laptop computer.

The problematic drift coefficient that appears in the drift expressions will be discussed in the next chapter.

CHAPTER 4

Turbulence And The Diffusion Tensor

4.1 Introduction

To better understand the diffusion of cosmic rays, one needs to consider the underlying turbulence in the solar wind plasma. The aim of this chapter is to give a short introduction to the concepts and quantities found in turbulence theory that are directly relevant to this study, and to introduce the models selected for elements of the diffusion tensor in this study.

4.2 Turbulence Properties

In general, the phenomenon of turbulence is considered to be the presence of random fluctuations in a physical process [see, e.g., *Davidson*, 2004]. The chaotic motion of smoke from a flame and the dynamics of mixing fluids are simple examples of turbulence in every day life.

Being a statistically random process, turbulence can only be described by general models that provide a good description for its overall evolution in time and space. These models are not capable of predicting properties such as the exact shape of the turbulent flow's structural geometry at a particular position in space and time or a path traced by a charged particle in a turbulent magnetic field [see, e.g., *Davidson*, 2004].

Consider a uniform background magnetic field B_o, taken to be directed along the z-axis of a right-handed Cartesian coordinate system. A turbulent magnetic field can be written in terms of this background field and a fluctuating component $\delta\mathbf{b}$, chosen to be only transverse to the field in the present study, thus

$$\mathbf{B} = B_o\mathbf{e}_z + \delta\mathbf{b}(x, y, z). \tag{4.1}$$

The properties of this fluctuating component depend on the choice of turbulence model. The total energy in the fluctuations is denoted by the variance δB^2. Turbulent fluctuations that are only perpendicular to the background field can be represented by three models, slab or one dimensional (1D) turbulence, two-dimensional (2D) turbulence, or composite (two-component) turbulence, which is a combination of these two [see, e.g., *Bieber et al.*, 1994]. We proceed with a brief description of these models.

4.2.1 Slab Turbulence

Slab turbulence consists of fluctuations that are synchronized going from one magnetic field line to any other one. For the same z coordinate the magnitude and direction of the fluctuations are identical for all magnetic field lines. As a consequence flux tubes beginning at the same position along the background field, but at arbitrary positions in the (x,y) plane, will in essence remain identical, due to their fluctuating component being only a function of z, as illustrated in the left-hand panel of Figure 4.1. The total field can be expressed by

$$\begin{aligned}\mathbf{B} &= B_o\mathbf{e}_z + \delta\mathbf{b}_{slab}(z),\\ &= B_o\mathbf{e}_z + \delta b_{slab,x}(z)\mathbf{e}_x + \delta b_{slab,y}(z)\mathbf{e}_y,\end{aligned} \tag{4.2}$$

with the variance given by

$$\delta B^2_{slab} = \delta b^2_{slab,x} + \delta b^2_{slab,y}. \tag{4.3}$$

For turbulence that is axisymmetric with respect to mean magnetic field direction z, the x and y components of fluctuations are identical, thus

$$\delta B^2_{slab} = 2\delta b^2_{slab,x} = 2\delta b^2_{slab,y}. \tag{4.4}$$

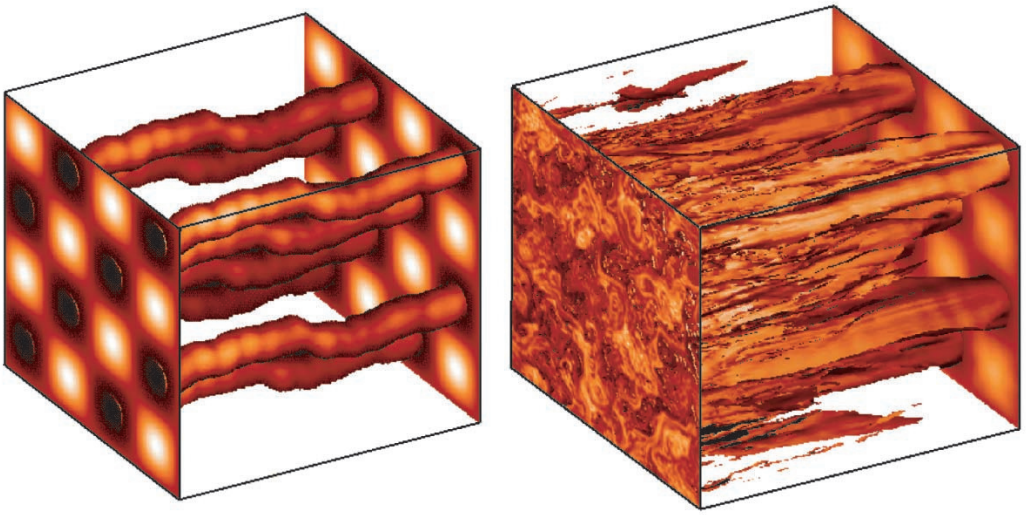

Figure 4.1: *Magnetic flux tubes for pure slab turbulence (left-hand panel) and 80/20 composite 2D/slab turbulence (right-hand panel). Note that flux tubes are initially circular on the right-hand side of the figure, and that the field lines that define the flux tubes are followed from right to left [Matthaeus et al., 2003].*

4.2.2 2D Turbulence

For the 2D model, fluctuations are assumed to be functions of transverse coordinate (x, y) only, such that the total magnetic field can be written as

$$\begin{aligned} \mathbf{B} &= B_o \mathbf{e}_z + \delta \mathbf{b}_{2D}(x, y), \\ &= B_o \mathbf{e}_z + \delta b_{x,2D}(x, y)\mathbf{e}_x + \delta b_{y,2D}(x, y)\mathbf{e}_y. \end{aligned} \tag{4.5}$$

and the fluctuations are assumed perpendicular to the uniform component, similar to the case for slab turbulence. In contrast to the case for slab turbulence, the 2D fluctuations are a function of coordinates perpendicular to the uniform background magnetic field only, and thus remain constant for any particular value of coordinate z, while varying in any given (x, y) plane. This leads to "braiding and shredding" [*Matthaeus et al.*, 2003] of the magnetic flux tubes. The consequence is that flux tubes starting at different (x, y) positions would evolve differently, in contrast to the case for slab turbulence.

The 2D variance is given by

$$\delta B_{2D}^2 = \delta b_{2D,x}^2 + \delta b_{2D,y}^2. \tag{4.6}$$

and again for turbulence that is axisymmetric with respect to mean magnetic field direction, we have

$$\delta B_{2D}^2 = 2\delta b_{2D,x}^2 = 2\delta b_{2D,y}^2. \tag{4.7}$$

4.2.3 Composite Turbulence

Often used to describe turbulence in the solar wind, the composite model represents a superposition of fluctuations of the slab and 2D turbulence models. These field fluctuations are expressed as

$$\delta \mathbf{b} = \delta \mathbf{b}_{slab}(z) + \delta \mathbf{b}_{2D}(x, y). \tag{4.8}$$

Observations suggest a composite turbulence model with some $70\% - 90\%$ of turbulence in the inertial energy range consisting of 2D turbulence, and the remainder as slab turbulence [see, e.g., *Matthaeus et al.*, 1990; *Bieber et al.*, 1996]. The right-hand panel of Figure 4.1 shows the composite turbulence model where the magnetic field lines are braided and shredded due to the dominant 2D turbulence in the model. The total variance can be written as [*Matthaeus et al.*, 1995]

$$\delta B^2 = \delta B_{slab}^2 + \delta B_{2D}^2. \tag{4.9}$$

Assuming axisymmetric turbulence, it then follows for composite turbulence that

$$\delta B^2 = 2\delta b_{slab,x}^2(z) + 2\delta b_{2D,x}^2(x, y). \tag{4.10}$$

4.2.4 Correlation Scale

Another important property to consider when dealing with a turbulent environment, is how the turbulence in one particular region of the system relates to that in a neighboring region. It is enough for the purpose of this study to simply state that the correlation length is a measure of the range over which fluctuations in one region of space relate to those in another region. Two points which are separated by a distance larger than the correlation length will each have fluctuations that are essentially independent, and will in essence be uncorrelated [*Choudhuri*, 1998].

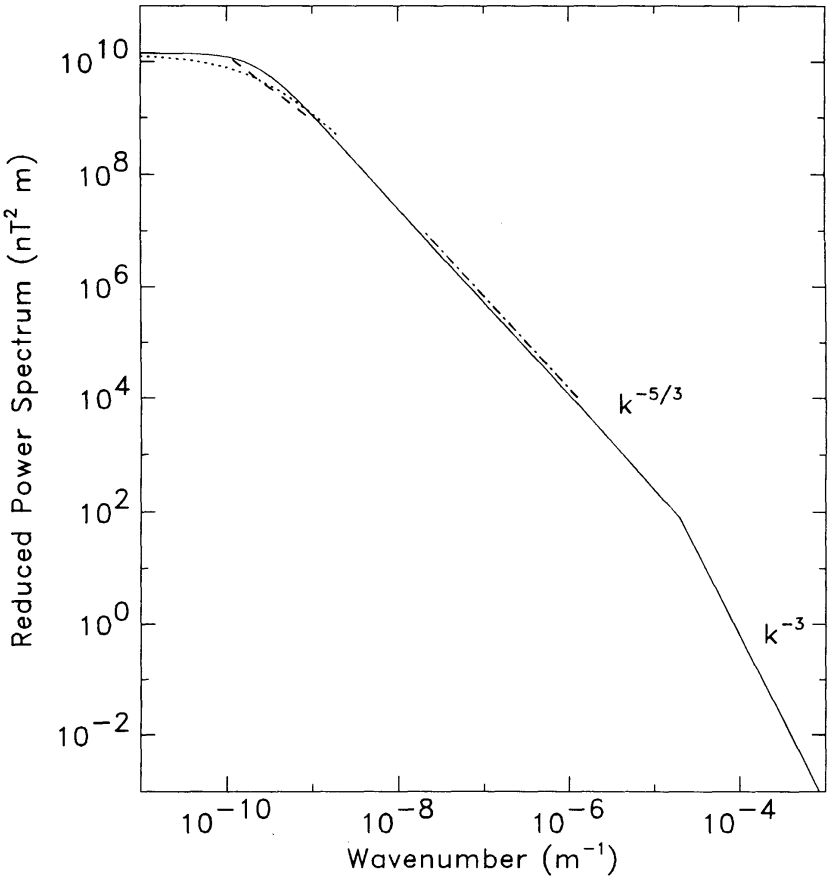

Figure 4.2: *Reduced perpendicular power spectrum of the slab model. The dotted, dashed and dot-dashed lines show spacecraft observations [Bieber et al., 1994].*

4.2.5 Turbulence Power Spectrum

The solid in Figure 4.2 line denotes the reduced perpendicular power spectrum of the slab model, while the dotted, dashed and dot-dashed lines denote spacecraft survey observations [*Bieber et al.*, 1994]. The main feature that is clearly visible is the gradual decrease in the energy per wavenumber as one moves to higher wavenumbers. Three regions can be identified from left to right, namely the energy range, the inertial range and the dissipation range.

At the lowest wavenumbers, the energy range occurs, representing scales at which energy is added to the spectrum and at which the driving of the turbulent eddies occurs. This region cannot extend to zero wavenumber, as this would imply fluctuations of infinite extent. Also note that the integral of this spectrum over wavenumber yields the total energy in that system, and this must be finite. This determines the behaviour of the spectrum at small wavenumbers.

The middle region is the inertial range and represents the Kolmogorov cascade, where the main decay of turbulence takes place. In this region the energy in the fluctuations per wavenumber as predicted by *Kolmogorov* [1941] is propotional to $k^{-5/3}$. The spectral break between the energy range and the inertial range is represented as k_{min} and gives a rough indication of the smallest perturbations that are externally driven in the whole turbulence range [see, e.g., *Bieber et al.*, 1994; *Goldstein et al.*, 1995].

The third region is the dissipation range. Here the energy per wavenumber decreases more rapidly than in the inertial range and the behaviour of real-fluid turbulence strongly deviates from the ideal-fluid case where Kolmogorov's law continues even for very large wavenumbers [see, e.g., *Coleman*, 1968; *Bieber et al.*, 1994]. Interactions with the background fluid on the molecular level inhibits further propagation and evolution of the fluctuations and their energy is lost as heat to the surrounding medium [*Coleman*, 1968; *Zank et al.*, 1996; *Leamon et al.*, 2000].

4.2.6 Radial Dependence Of Variance And Correlation Scales

Solutions of the two-component *Oughton et al.* [2011] turbulence transport model are shown in Figure 4.3. The top panel shows the variances associated with the wavelike and quasi-2D components, as well as the total variance, with *Voyager 1* and *2* data from *Zank et al.* [1996], and one point from the results presented by *Smith et al.* [2006]. The bottom panel shows the various correlation lengthscales, with observations from *Matthaeus et al.* [1999], *Smith et al.* [2001], *Weygand et al.* [2009], and *Weygand et al.* [2011]. The variance associated with the quasi-2D component monotonically decreases with increasing radial distance. The wavelike component initially decreases steadily as a function of radial distance, but then flattens out at radial distances associated with ionization cavity, beyond which pickup ion energy is injected into the fluctuations. The total variance is calculated as the sum of the quasi-2D and wave-like variances, and follows the trend of the *Zank et al.* [1996] data rather well.

In the bottom panel both the parallel and perpendicular correlation lengthscales at Earth agree well with observational data reported by *Weygand et al.* [2011]. The monotonically increasing perpendicular correlation scales are consistent with the decaying quasi-2D variance in the top panel. The action of pickup ions on the behaviour of the parallel lengthscale in the outer heliosphere can clearly be seen, where it displays a marked decrease as function of radial distance. This decrease starts at approximately the same radial distance as the increase noted in the wavelike variance. The parallel lengthscale relaxes in the outer heliosphere to the resonant scale, causing it to increase again.

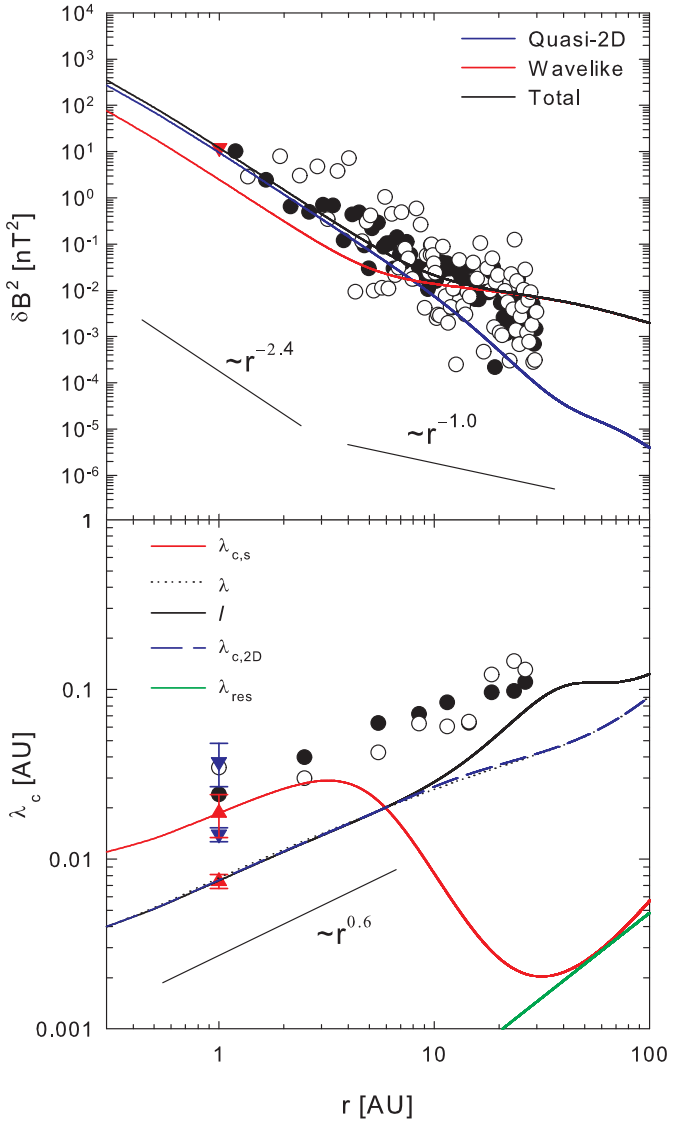

Figure 4.3: *Solutions of the two-component Oughton et al. [2011] turbulence transport model. The top panel shows the variance solutions along with Voyager data from Zank et al. [1996], and one point from the results presented by Smith et al. [2006]. The bottom panel shows the associated correlation lengthscales, with observations from Matthaeus et al. [1999], Smith et al. [2001], Weygand et al. [2009], and Weygand et al. [2011], as function of radial distance in the solar ecliptic plane. Adapted from Engelbrecht [2013].*

In the present study single, double and triple power laws were applied to the turbulence model results of *Engelbrecht* [2013], so as to replicate the spatial dependence of the model results presented in Figure 4.3. Note that in what follows, the wavelike component will be associated with slab turbulence, and the quasi-2D with 2D turbulence.

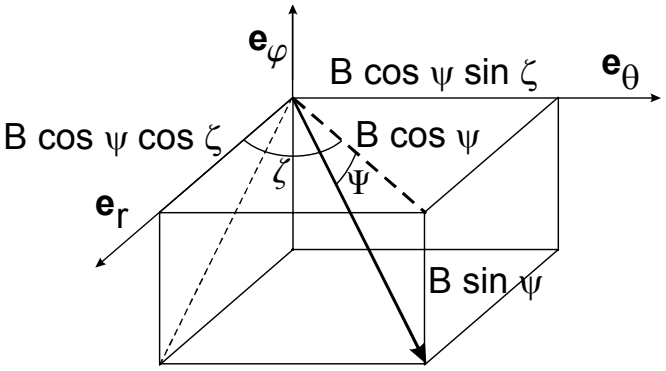

Figure 4.4: *Components of the magnetic field in terms of ψ and ζ (see text for details) [Burger et al., 2008].*

4.3 Diffusion- And Drift Coefficients

The diffusion tensor $\mathbf{K}$ that appears in the *Parker* [1965] cosmic-ray transport equation (Equation 2.15) can be written in spherical coordinates as

$$\mathbf{K} = \begin{bmatrix} \kappa_{rr} & \kappa_{r\theta} & \kappa_{r\phi} \\ \kappa_{\theta r} & \kappa_{\theta\theta} & \kappa_{\theta\phi} \\ \kappa_{\phi r} & \kappa_{\phi\theta} & \kappa_{\phi\phi} \end{bmatrix}, \tag{4.11}$$

whereas in a field-aligned coordinate system the diffusion tensor becomes

$$\mathbf{K}' = \begin{bmatrix} \kappa_{\parallel} & 0 & 0 \\ 0 & \kappa_{\perp,2} & \kappa_A \\ 0 & -\kappa_A & \kappa_{\perp,3} \end{bmatrix}, \tag{4.12}$$

where $\kappa_{\parallel}$ describes diffusion parallel to the mean magnetic field, the anisotropic terms κ_A denote the drift coefficient, and $\kappa_{\perp,2}$ and $\kappa_{\perp,3}$, respectively describe diffusion in the two directions perpendicular to the mean magnetic field. Note that for completeness the above tensor allows for non-axisymmetric perpendicular diffusion. The present study assumes axisymmetric turbulence and consequently axisymmetric perpendicular diffusion, so that $\kappa_{\perp,2} = \kappa_{\perp,3}$.

The coefficients in the field-aligned tensor can be related to those of the tensor in heliocentric spherical coordinates by [*Burger et al.*, 2008]

$$
\begin{aligned}
\kappa_{rr} &= (\kappa_{\parallel}\cos^2\psi + \kappa_{\perp,3}\sin^2\psi)\cos^2\zeta + \kappa_{\perp,2}\sin^2\zeta \\
\kappa_{r\theta} &= (\kappa_{\parallel}\cos^2\psi + \kappa_{\perp,3}\sin^2\psi - \kappa_{\perp,2})\sin\zeta\cos\zeta - \kappa_A\sin\psi \\
\kappa_{r\phi} &= (-\kappa_{\parallel} + \kappa_{\perp,3})\sin\psi\cos\psi\cos\zeta - \kappa_A\cos\psi\sin\zeta \\
\kappa_{\theta r} &= (\kappa_{\parallel}\cos^2\psi + \kappa_{\perp,3}\sin^2\psi - \kappa_{\perp,2})\sin\zeta\cos\zeta + \kappa_A\sin\psi \\
\kappa_{\theta\theta} &= (\kappa_{\parallel}\cos^2\psi + \kappa_{\perp,3}\sin^2\psi)\sin^2\zeta + \kappa_{\perp,2}\cos^2\zeta \\
\kappa_{\theta\phi} &= (-\kappa_{\parallel} + \kappa_{\perp,3})\sin\psi\cos\psi\sin\zeta + \kappa_A\cos\psi\cos\zeta \\
\kappa_{\phi r} &= (-\kappa_{\parallel} + \kappa_{\perp,3})\sin\psi\cos\psi\cos\zeta + \kappa_A\cos\psi\sin\zeta \\
\kappa_{\phi\theta} &= (-\kappa_{\parallel} + \kappa_{\perp,3})\sin\psi\cos\psi\sin\zeta - \kappa_A\cos\psi\cos\zeta \\
\kappa_{\phi\phi} &= \kappa_{\parallel}\sin^2\psi + \kappa_{\perp,3}\cos^2\psi
\end{aligned}
\tag{4.13}
$$

with the angles ψ and ζ from Figure 4.4, defined as

$$
\begin{aligned}
\sin\psi &= -\frac{B_\phi}{B}; & \cos\psi &= \frac{\sqrt{B_r^2 + B_\theta^2}}{B} \\
\cos\zeta &= \frac{B_r}{\sqrt{B_r^2 + B_\theta^2}}; & \cos\zeta &= \frac{B_\theta}{\sqrt{B_r^2 + B_\theta^2}}
\end{aligned}
\tag{4.14}
$$

which implies that

$$
\tan\psi = -\frac{B_\phi}{\sqrt{B_r^2 + B_\theta^2}}. \tag{4.15}
$$

The above transformation assumes a general heliospheric magnetic field model with a finite meridional component. In the present study a Parker field is employed, with a zero meridional component, and thus Equations 4.13 and 4.15 reduce to the results of *Alania and Dzhapiashvili* [1979], *Kobylinski* [2001] and *Alania* [2002] such that

$$
\begin{aligned}
\kappa_{rr} &= \kappa_{\parallel} \cos^2\psi + \kappa_{\perp,3} \sin^2\psi \\
\kappa_{r\theta} &= -\kappa_A \sin\psi \\
\kappa_{r\phi} &= (-\kappa_{\parallel} + \kappa_{\perp,3}) \sin\psi \cos\psi \\
\kappa_{\theta r} &= \kappa_A \sin\psi \\
\kappa_{\theta\theta} &= \kappa_{\perp,2} \\
\kappa_{\theta\phi} &= \kappa_A \cos\psi \\
\kappa_{\phi r} &= (-\kappa_{\parallel} + \kappa_{\perp,3}) \sin\psi \cos\psi \\
\kappa_{\phi\theta} &= -\kappa_A \cos\psi \\
\kappa_{\phi\phi} &= \kappa_{\parallel} \sin^2\psi + \kappa_{\perp,3} \cos^2\psi
\end{aligned}
\tag{4.16}
$$

and

$$
\tan\psi = -\frac{B_\phi}{B_r}. \tag{4.17}
$$

For a generalised expression for the diffusion tensor that is also applicable when non-axisymmetric perpendicular diffusion is assumed see *Effenberger et al.* [2012]. The diffusion coefficients found in the tensor 4.12 can be written in terms of the mean free paths parallel and perpendicular to the mean HMF, such that

$$
\begin{aligned}
\kappa_{\parallel} &= \frac{v}{3}\lambda_{\parallel} \\
\kappa_{\perp} &= \frac{v}{3}\lambda_{\perp},
\end{aligned}
\tag{4.18}
$$

with v the particle speed.

4.3.1 The Parallel Mean Free Path

Teufel and Schlickeiser [2003] derive piecewise-continuous expressions for the parallel mean free paths from Quasilinear Theory (QLT), introduced by *Jokipii* [1966], for a full turbulence spectrum including an energy range, for both the damping and the random sweeping models of dynamical turbulence [*Bieber et al.*, 1994]. Here we follow *Engelbrecht* [2008] to construct a coefficient for diffusion parallel to the background magnetic field.

We assume that the power spectra for both slab- and 2D turbulence are flat in the energy range, and has a Kolmogorov range at smaller scales (larger wavenumbers or frequency) with a spectral index of $-5/3$, as stated in Chapter 1. At still larger wavenumbers

the spectrum steepens in the dissipation range as shown in Figure 4.2 [*Bieber et al.*, 1994]. However, since we are focusing on protons of relatively high energy, we neglect the dissipation range and effects like dynamical turbulence related to it.

Note however that the turbulence transport model employed in the present study differs from that employed by *Engelbrecht* [2008], and therefore the spatial dependences will be different to those discussed by *Engelbrecht* [2008], and be more similar to those of *Engelbrecht* [2013]. The general expression for the parallel mean free path derived by *Teufel and Schlickeiser* [2003] for the random sweeping model is given by

$$\lambda_{\parallel} = \frac{3s}{\sqrt{\pi}(s-1)} \frac{R^2}{bk_{min}} \frac{B_o^2}{\delta B_{slab}^2} K, \tag{4.19}$$

with s the spectral index of the inertial range (defined here to be positive, with a value of $+5/3$ for a Kolmogorov cascade), and

$$\begin{aligned} b &= \frac{v}{2\alpha_d V_A}, \\ R &= k_{\min} R_L, \\ Q &= k_D R_L, \end{aligned} \tag{4.20}$$

where α_d is a parameter determining the strength of dynamical effects [*Bieber et al.*, 1994; *Teufel and Schlickeiser*, 2002], $R_L = \frac{P}{cB_o}$ denotes the maximal Larmor radius (with $P = \frac{pc}{|q|}$ the particle rigidity), v the particle speed, and δB_{slab}^2 the total slab variance. The quantity k_{min} refers to the spectral break between the energy range and the inertial range, as discussed in Section 4.2.5. Since the slab turbulence spectrum has a flat energy range, there is a simple relation between the correlation scale and the inverse of the wavenumber where the break occurs, given by *Engelbrecht* [2013] as

$$k_{min} = \frac{\pi}{5\lambda_{c,slab}}. \tag{4.21}$$

The function K denotes an analytical solution most appropriate to a certain range of values of the parameters listed in Equation 4.20. These piece-wise solutions are listed in Table 4.1. Note that the quantity p in this table is the spectral index in the dissipation range, not to be confused with particle momentum. To determine which of these solutions are appropriate for particles interacting with only the energy- and the inertial range, we note that the denominator of the coefficient of K in Equation 4.19 for $\lambda_{\parallel}$ contains b, which includes the parameter α_d quantifying dynamical effects, which we neglect. Therefore any K that is not directly proportional to b should be neglected, as

Case no.	Case	K
1	$1 \ll b \ll R \ll Q$	$\frac{b}{4\sqrt{\pi}}$
2	$1 \ll R \ll Q \ll b$	$\frac{b}{4\sqrt{\pi}} + [\frac{1}{\Gamma(p/2)} + \frac{1}{\sqrt{\pi}(p-2)}]\frac{b^{p-1}}{Q^{p-s}R^s}$
3	$1 \ll R \ll b \ll Q$	$\frac{b}{4\sqrt{\pi}}$
4	$b \ll 1 \ll R \ll Q$	$\frac{2}{3}\frac{s}{2-\gamma s-2s\ln b/R}$
5	$b \ll R \ll Q \ll 1$	$\frac{2}{3}\frac{s}{2-\gamma s-2s\ln b/R}$
6	$b \ll R \ll 1 \ll Q$	$\frac{2}{3}\frac{s}{2-\gamma s-2s\ln b/R}$
7	$R \ll Q \ll 1 \ll b$	$[\frac{1}{\Gamma(p/2)} + \frac{1}{\sqrt{\pi}(p-2)}]\frac{b^{p-1}}{Q^{p-s}R^s}$
8	$R \ll Q \ll b \ll 1$	$\frac{2}{3\Gamma(p/2)}\frac{b^p}{Q^{p-s}R^s}$
9	$R \ll 1 \ll b \ll Q$	$\frac{2}{\sqrt{\pi}(2-s)(4-s)}\frac{b}{R^s}$
10	$R \ll 1 \ll Q \ll b$	$[\frac{1}{\Gamma(p/2)} + \frac{1}{\sqrt{\pi}(p-2)}]\frac{b^{p-1}}{Q^{p-s}R^s} + \frac{2}{\sqrt{\pi}(2-s)(4-s)}\frac{b}{R^s}$
11	$R \ll b \ll 1 \ll Q$	$\frac{2}{3\Gamma(s/2)}\frac{b^s}{R^s}$
12	$R \ll b \ll Q \ll 1$	$\frac{2}{3\Gamma(s/2)}\frac{b^s}{R^s}$

Table 4.1: *Analytical expressions for K for the random sweeping model, from Teufel and Schlickeiser [2003]. The quantity p is the spectral index in the dissipation range, not to be confused with particle momentum.*

well as terms that include the spectral index p of the dissipation range. This eliminates all but 1, 3, 9, and the second part of 10. The latter is identical to 9, and 1 to 3, so that we can use a combination of 1 and 9. As was discussed by *Engelbrecht* [2008], solutions numbered 1 and 9 can be used to construct a tractable, continuous expression for the proton parallel mean free path, given by

$$\lambda_{\parallel} = \frac{3s}{4\pi(s-1)}\frac{R^2}{k_{min}}\frac{B_o^2}{\delta B_{slab}^2}\left[1 + \frac{8}{(2-s)(4-s)}\frac{1}{R^s}\right]. \tag{4.22}$$

4.3.2 The Perpendicular Mean Free Path

Perpendicular diffusion has often been described via the Field Line Random Walk (FLRW) limit of the Quasilinear Theory [*Jokipii*, 1966], where the particle gyrocenters follow field lines which themselves spread diffusively, allowing for a net particle diffusive spread perpendicular to the mean magnetic field. This approach, however, is inconsistent with numerical simulations [*Giacalone and Jokipii*, 1999], being only accurate at high particle energies. *Matthaeus et al.* [2003] derive a Nonlinear Guiding Center Theory (NLGC) based on the assumption that perpendicular transport is governed by the velocities of the charged particles gyrating along the magnetic field lines, which in turn diffusively separate, but here due to the transverse structure of the field turbulence. This theory, when compared with test particle simulations, more closely approaches the simulation values than other existing theories describing perpendicular transport.

However, as enumerated by *Engelbrecht* [2008] there are several other reasons for choosing the NLGC perpendicular mean free paths to be applied in studies such as the present one. Firstly, the NLGC perpendicular mean free path expressions are functions of the particle parallel mean free path. This is important, as a coupling between these two quantities occurs in other non-linear theories as well [see, e.g., *Shalchi et al.*, 2004b]. Secondly, NLGC predicts a perpendicular mean free path which, in magnitude, is only of the order of one or a few percent of the input parallel mean free path, which is consistent with particle observations [*Palmer*, 1982]. Lastly, when the NLGC perpendicular mean free paths are compared to observational mean free paths from Jovian electrons, the values of the perpendicular mean free paths are in good agreement [*Bieber et al.*, 2004].

Shalchi et al. [2004a] provide analytical approximations for the results of the perpendicular mean free path from the NLGC theory. In the present study, the approximate analytical solution derived by *Shalchi et al.* [2004a], as presented by *Burger et al.* [2008] for a general ratio of slab to 2D variance, is used. This expression, is given by

$$\lambda_{\perp} = \left[\frac{2\nu - 1}{4\nu} a^2 F_2(\nu) \lambda_{c,2D} \sqrt{3} \frac{\delta B_{2D}^2}{B_o^2}\right]^{2/3} \lambda_{\parallel}^{1/3}, \tag{4.23}$$

where $a = 1/\sqrt{3}$ is a numerical factor, with $F_2(\nu) = 2\pi C(\nu) F_1(\nu)$, $F_1(\nu) = 2\nu/(2\nu - 1)$ and

$$C(\nu) = \frac{1}{2\sqrt{\pi}} \left[\frac{\Gamma(\nu)}{\Gamma\left(\nu - \frac{1}{2}\right)}\right]. \tag{4.24}$$

4.3.3 The Drift Coefficient

Gradient- and curvature drifts play a key role in the charge-dependent modulation of cosmic rays and appear explicitly or implicitly in most models for cosmic-ray modulation. *Forman et al.* [1974] and *Jokipii and Parker* [1970] show that in the weak-scattering limit, with little to no turbulence present, the *Parker* [1965] cosmic-ray transport equation (Equation 2.15) contains the drift coefficient

$$\kappa_A^{ws} = \frac{v R_L}{3}, \tag{4.25}$$

in the diffusion tensor, with v the particle speed, and R_L the Larmor radius as discussed in Section 3.2. Reduction in the drift coefficient due to turbulence has been

demonstrated unambiguously by means of direct numerical simulations [see, e.g., *Jokipii*, 1993; *Giacalone et al.*, 1999; *Candia and Roulet*, 2004; *Minnie et al.*, 2007b; *Tautz and Shalchi*, 2012]. However, there is yet as no generally accepted theoretical expression for this transport coefficient [see, e.g., *Burger and Visser*, 2010; *Engelbrecht and Burger*, 2015]. *Burger and Visser* [2010] introduce a parameterized form of the drift coefficient based on direct numerical simulations and show that good agreement with observed proton energy spectra at Earth can be found when it is used in a numerical modulation model.

Burger and Visser [2010] use, as a point of departure, the results of *Bieber and Matthaeus* [1997] who find that

$$\kappa_A = \frac{v}{3}\lambda_A = \frac{vR_L}{3}\frac{\Omega^2\tau^2}{1+\Omega^2\tau^2}, \tag{4.26}$$

with Ω the angular gyrofrequency of a charged particle and τ is the time associated with the rate at which the helical paths of the particles gradually become less helical because of unspecified interactions. By making various assumptions, *Bieber and Matthaeus* [1997] furthermore conclude that

$$\Omega\tau = \frac{2}{3}\frac{R_L}{D_\perp}, \tag{4.27}$$

where $D_\perp$ is the perpendicular field line random walk diffusion coefficient of a statistically homogeneous magnetic field and is given as [*Matthaeus et al.*, 1995]

$$D_\perp = \frac{1}{2}\left(D_{slab} + \sqrt{D_{slab}^2 + 4D_{2D}^2}\right). \tag{4.28}$$

Here D_{slab} and D_{2D} are the field line diffusion coefficients due to slab and 2D fluctuations, respectively and can be expressed as [*Matthaeus et al.*, 2007]

$$D_{slab} = \frac{1}{2}\frac{\delta B_{slab}^2}{B^2}\lambda_{c,slab}; \qquad D_{2D} = \frac{\sqrt{\delta B_{2D}^2/2}}{B}\lambda_{u,2D}, \tag{4.29}$$

with $\lambda_{c,slab}$ the slab correlation scale and $\lambda_{u,2D}$ the 2D ultrascale. *Visser* [2009] shows that the theoretical predictions of the drift coefficient derived by *Bieber and Matthaeus* [1997] does not give a good fit to the results of *Minnie et al.* [2007b]. *Burger and Visser* [2010] redefine the quantity $\Omega\tau$ and find that the form

$$\Omega\tau = \frac{11}{3}\frac{\sqrt{R_L/\lambda_{c,slab}}}{(D_\perp/\lambda_{c,slab})^g}; \qquad g = 0.3\log\left[\frac{R_L}{\lambda_{c,slab}}\right] + 1.0, \tag{4.30}$$

yields good fits to the direct numerical simulations for the drift coefficients performed by *Minnie et al.* [2007b].

4.4 Summary And Conclusions

In this chapter turbulence properties are introduced and a composite slab/2D structure described. The turbulence spectra are assumed to have flat energy range and a Kolmogorov inertial range, in wavenumber (or frequency) space. Since this study is focused on relatively high energy protons, the dissipation range and effects related to it are ignored.

The parallel mean free path expression of *Teufel and Schlickeiser* [2003] for the random sweeping model is used. It is shown that the assumption to neglect the dissipation range and effects related to it, leads to a natural selection of the appropriate piece-wise continuous functions derived by these authors. An analytical approximation from the Nonlinear Guiding Center Theory (NLGC) of *Matthaeus et al.* [2003] derived by *Shalchi et al.* [2004a] is used for the perpendicular mean free path.

The form of the drift coefficient is currently well-known only in the absence of turbulence, and there is no generally accepted form for it when turbulence is taken into account. This distracts from the *ab initio* approach of this study. The only reasonable alternative was to use the parameterized expression constructed by *Burger and Visser* [2010]. The form of this construction is based on direct numerical studies by *Minnie et al.* [2007b]. There is no guarantee that this form of the drift coefficient will resemble the form of the actual drift coefficient when and if it is derived. It is therefore expected that the cosmic-ray modulation model should give better results at high energies, where the weak-scattering limit comes into play.

CHAPTER 5

Neutron Monitor Data Analyses

5.1 Introduction

Any study of long-term galactic cosmic-ray modulation should include the heliospheric current sheet inclination. As discussed in Section 2.6, the current sheet tilt angle can be modelled as the angle between the solar rotation axis and the solar magnetic axis. Among the important early tests for the significance of the current sheet tilt angle in the overall modulation process was an observed anti-correlation between the intensity of high-energy galactic cosmic rays and the current sheet tilt angle [*Svalgaard and Wilcox*, 1974; *Smith and Thomas*, 1986; *Saito and Swinson*, 1986; *Lockwood et al.*, 1988; *Webber and Lockwood*, 1990; *Smith*, 1990]. Observations of galactic cosmic rays are available from Earth-based neutron monitors as well as spacecraft, as discussed in Chapter 2. Additional data have now become available including data spanning more polarity reversals making it possible to extend the earlier studies mentioned above to a longer time interval.

Figure 5.1 shows the average monthly cosmic-ray intensity from the Potchefstroom neutron monitor along with the average monthly "radial" current sheet tilt angle. The tilt angle values, which are averaged over Carrington rotations, were converted to monthly averages by interpolation. These tilt angle measurements extend over more than three solar-activity cycles which cover a complete 22-year solar-magnetic cycle plus data from 2000 to 2010 that can be used to examine the periodic nature of cosmic ray variations.

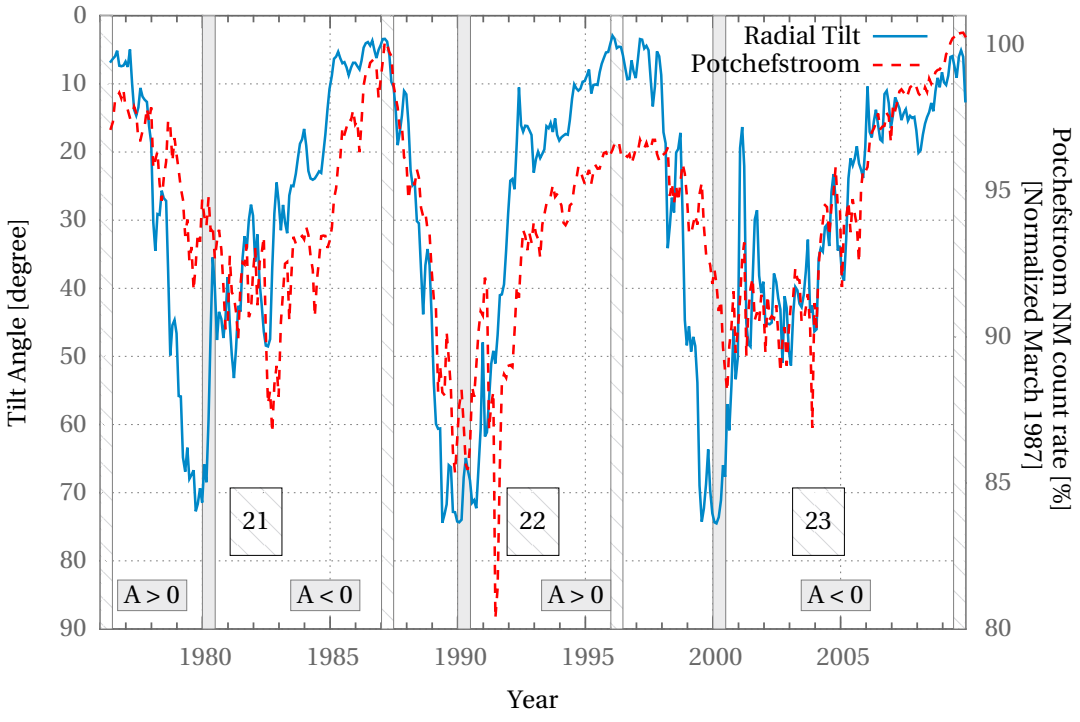

Figure 5.1: *The Potchefstroom cosmic-ray neutron monitor count rate compared to the tilt angle. The count rates are normalised to 100 % in March 1987. The shaded area represent a magnetic polarity change over. A clear 11-year cycle, anti-correlated to the tilt angle cycle, and a 22-year polarity cycle can be seen. Note that tilt angle increases from top to bottom while the neutron monitor count increases from bottom to top. According to the website* `http://wso.stanford.edu/Tilts.html`*, values above 70° should be considered lower limits.*

Apart from the anti-correlation between count rate and tilt angle, there is a distinctive asymmetry between the descending and ascending phases of the cosmic-ray modulation (corresponding to the increasing and decreasing phases of current sheet tilt angle). The long-term cosmic-ray intensity curve as measured by neutron monitors also appears to follow a 22-year cycle with alternate maxima being flat-topped or peaked [see, e.g., *Barnden and Bercovitch*, 1975; *Kóta*, 1979; *Jokipii and Thomas*, 1981; *Kóta and Jokipii*, 1983; *Smith*, 1990; *Lockwood et al.*, 2001]. This behaviour is predicted by drift models of cosmic-ray modulation based on the change of the solar magnetic field polarity every 11 years [see *Jokipii et al.*, 1977, and the numerous references to it].

This pattern in the cosmic-ray intensity curve has been interpreted as a manifestation of the different sensitivities of cosmic-ray intensity to the current sheet tilt angle in alternate solar magnetic polarity cycles [*Kóta and Jokipii*, 1983; *Potgieter and Moraal*, 1985; *Webber and Lockwood*, 1988; *Smith*, 1990; *Cliver and Ling*, 2001]. In the negative solar magnetic polarity cycle (denoted by $A < 0$ in Figure 5.1) when the cosmic-ray intensity curve is peaked, the north solar polar magnetic field is directed towards the

Sun. At this time the drift of the cosmic rays is inward from the heliospheric boundary along the current sheet toward Earth, shown in Figure 5.2a. When the solar magnetic field polarity reverses and becomes positive (denoted by $A > 0$ in Figure 5.1), cosmic rays drift from the solar polar regions to the Earth and out along the heliospheric current sheet to the boundary of the heliosphere, shown in Figure 5.2b.

Cane et al. [1999] examined the correlation between the tilt angle and the cosmic-ray neutron monitor counting rate throughout the 22 years from beginning 1976 to end 1997 and showed that an anti-correlation persisted for most of the cycle. However, the different response of cosmic rays to tilt angle changes for positive or negative solar magnetic field polarities is restricted to a range of smaller tilt angles around solar minimum. *Cliver and Ling* [2001] have also noted that the neutron monitor intensity-time curve lagged the current sheet tilt curve by a longer time at the time of the 1980 peak in solar activity compared to the 1990 peak of solar activity.

The current sheet tilt angle is considered to be an indicator of the large-scale magnetic fields on the Sun and in the heliosphere. The changeover of these fields from one magnetic polarity to the other generally occurs when this current sheet tilt angle is larger than $\sim 70^\circ$ and is shown as shaded bands in Figure 5.1. Note however that according to the website `http://wso.stanford.edu/Tilts.html`, values above 70° should be considered to be lower limits. This tilt angle interpretation is confirmed by magnetic field data from *Ulysses* [*Jones et al.*, 2003], which shows the main field changeover occurring during the same time period for which the tilt angle is larger than $\sim 70^\circ$. For a simple dipole model of the solar magnetic field, the tilt angle can reach 90° when the dipole flips over and northern and southern magnetic polarities are switched.

5.2 Idealized Steady-State Drift Description

To further investigate the dependence of cosmic-ray intensity on the tilt angle, *Smith* [2006] proposed a simple test to investigate each solar cycle such that the magnetic polarity change over occurs midway through the cycle. A possible result is shown in Figure 5.3, an idealized steady-state description showing what might be expected assuming that cosmic-ray intensity is more sensitive to changes in tilt angle during negative than positive magnetic polarity as predicted by drift models. For a comparison between idealized steady-state and time-dependent drift models, see *Le Roux and Potgieter* [1990].

For the positive/negative reversal, the intensity is at a maximum at solar minimum and decreases (linearly in this qualitative description) with increasing tilt angle. The magnetic polarity reverses at the maximum inclination of the current sheet and because

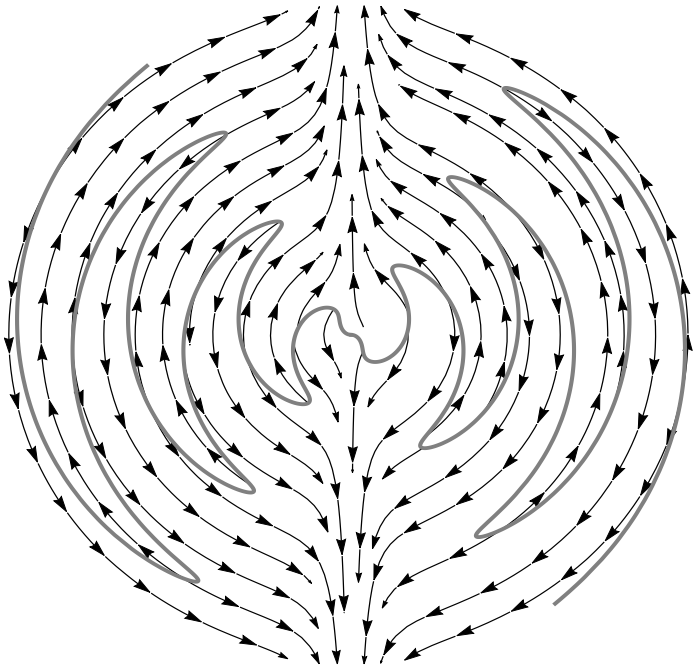

(a) *Drift pattern for an $A < 0$ solar polarity cycle. Although not shown, the drift direction along the wavy current sheet, denoted by the grey solid line, is inwards towards the Sun at the centre of the heliosphere.*

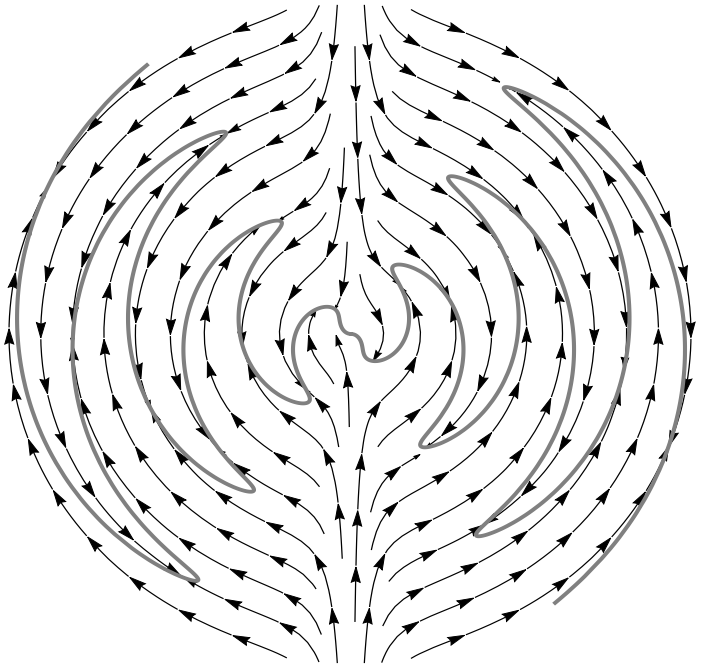

(b) *Drift pattern for an $A > 0$ solar polarity cycle. Although not shown, the drift direction along the wavy current sheet, denoted by the grey solid line, is outwards away from the Sun at the centre of the heliosphere.*

Figure 5.2: *Drift patterns for $A > 0$ and $A < 0$ solar polarity cycles, for a 20 AU heliosphere and a tilt angle of 60°.*

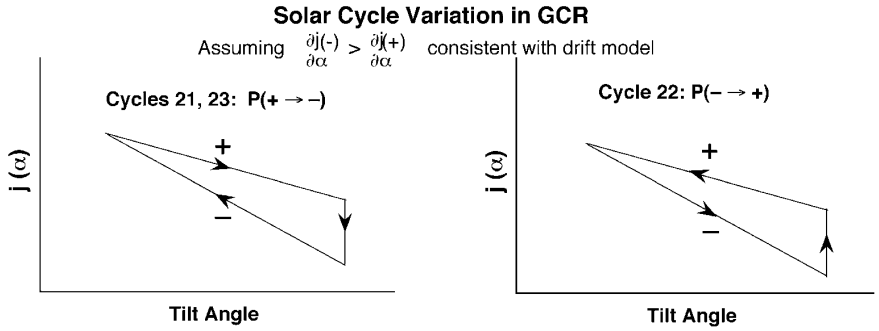

Figure 5.3: *Anticipated variation between galactic cosmic rays and tilt angle over the solar cycle. According to an idealized steady-state description of a drift model, the intensities j should be less sensitive to changes in tilt angle for positive magnetic polarity P(+) than for negative magnetic polarity P(-). Notable features are a clockwise traversal of the intensity-tilt loop for + to − polarity change and a counter-clockwise traversal of the intensity-tilt loop for a − to + change [Smith, 2006].*

the transition is from a positive polarity (gradient- and curvature drift direction towards Earth as shown in Figure 5.2b; easy drift access) to a negative one (gradient- and curvature drift direction away from current sheet as shown in Figure 5.2a, and only current sheet drift towards Earth, implying less easy access by drift), there is a drop in intensity. Thereafter, the intensity lies below the intensity during positive magnetic polarity as it returns to a maximum value at the next solar minimum. This results in an intensity-tilt loop that has a clock-wise rotation. For the negative/positive reversal, the conditions are reversed with the intensities following the lower trajectory during the descending phase, a jump upward during the polarity reversal and higher values for the positive magnetic polarity intensity during the recovery. While the intensity-tilt loop is assumed to have the same shape and size as for the positive/negative case, the apparent sense of change is now anti-clockwise.

In this clearly simplified description of the effect of particle drifts on long-term cosmic-ray modulation, two features occur: the intensity-tilt loops have the same size when the solar magnetic polarity changes from positive to negative, and from negative to positive. There is, however, a change in the sense in which the intensity changes. When the polarity changes from positive to negative, the change follows a clockwise direction, and when the polarity changes from negative to positive, the change follows an anti-clockwise direction. We will refer back to these two features in what follows.

5.3 Intensity-Tilt Observations

Turning now to observations, Figure 5.4 shows the Climax neutron monitor cosmic-ray count rate and the *IMP 8* >70 MeV cosmic-ray intensity for solar cycle 21 from

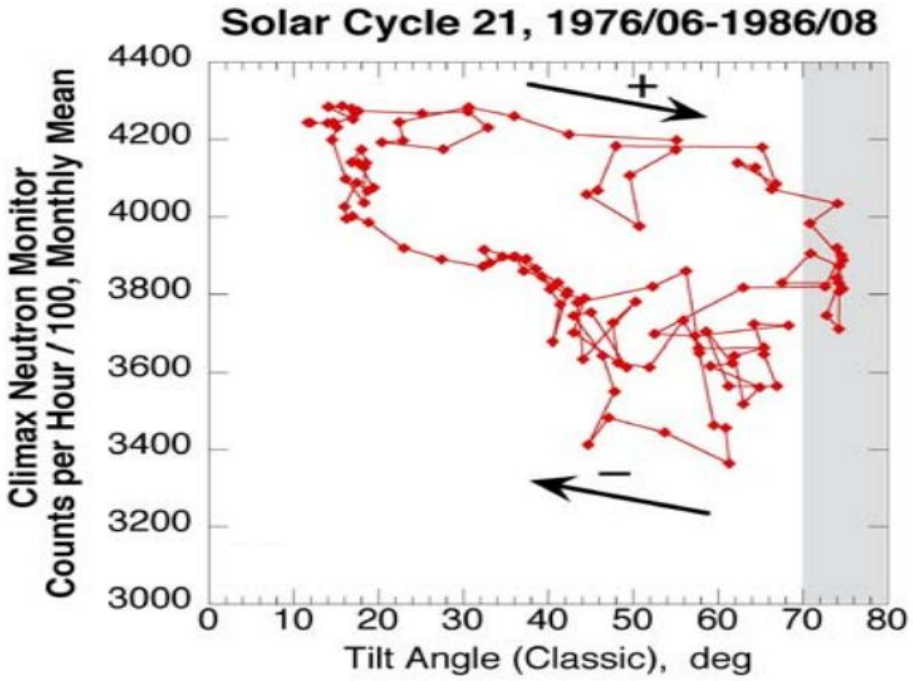

(a) Climax neutron monitor counts [Smith, 2006].

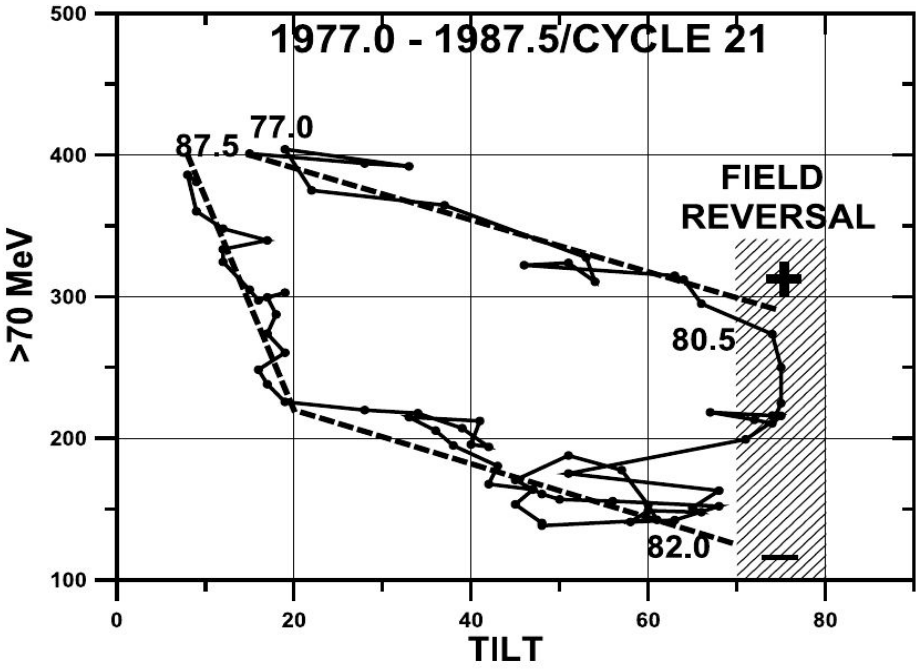

(b) IMP 8 >70 MeV intensities [Lockwood and Webber, 2005].

Figure 5.4: *Plots of intensity as a function of the tilt angle α for solar cycle 21, a positive/negative cycle. The +/- signs denote magnetic field polarity. The arrows indicate the progression during the descending and ascending phases in cosmic-ray modulation.*

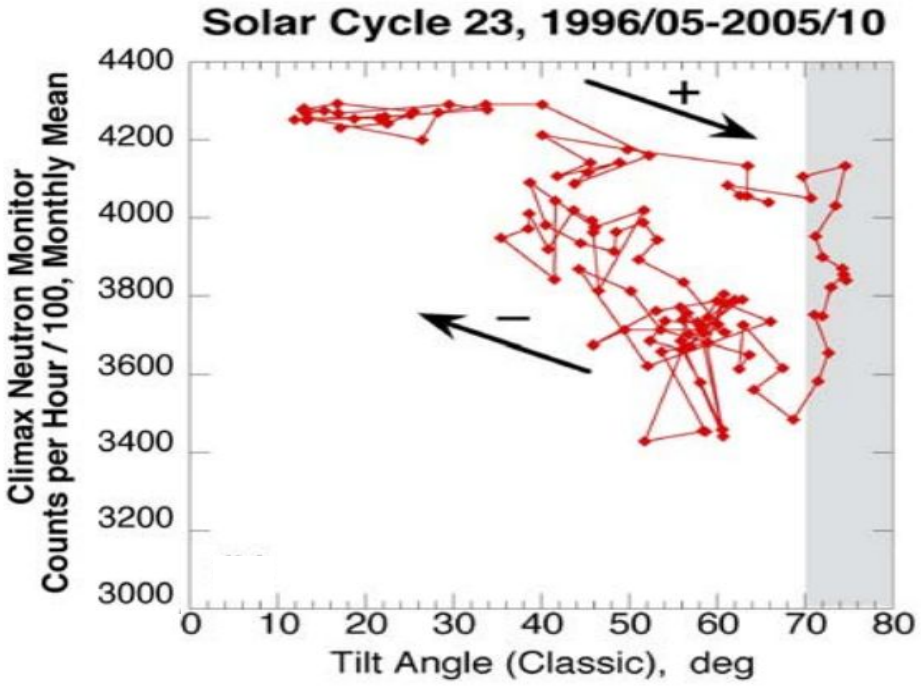

(a) Climax neutron monitor counts [Smith, 2006].

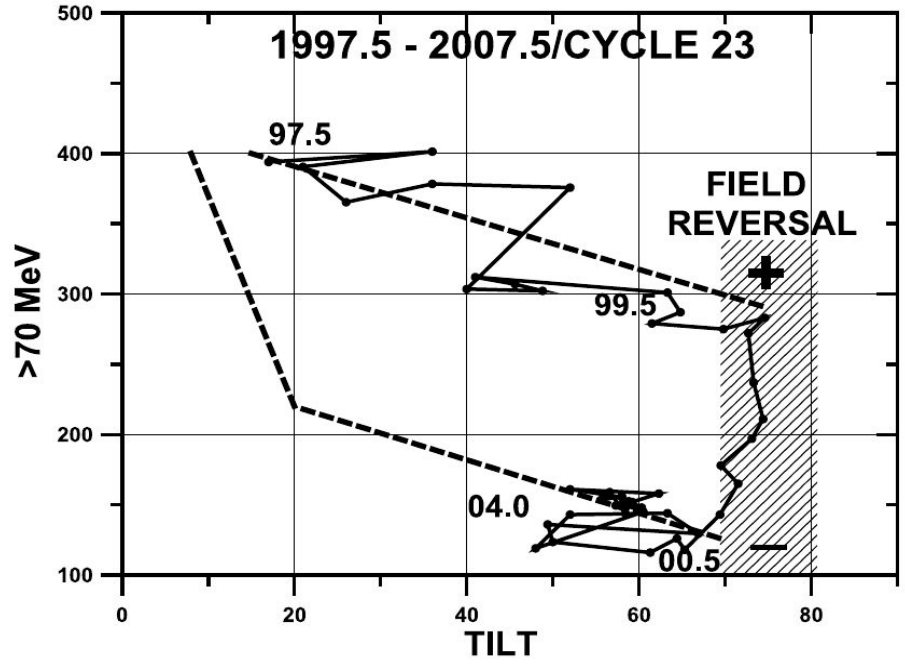

(b) IMP 8 >70 MeV intensities [Lockwood and Webber, 2005].

Figure 5.5: *Same as Figure 5.4, but for cycle 23.*

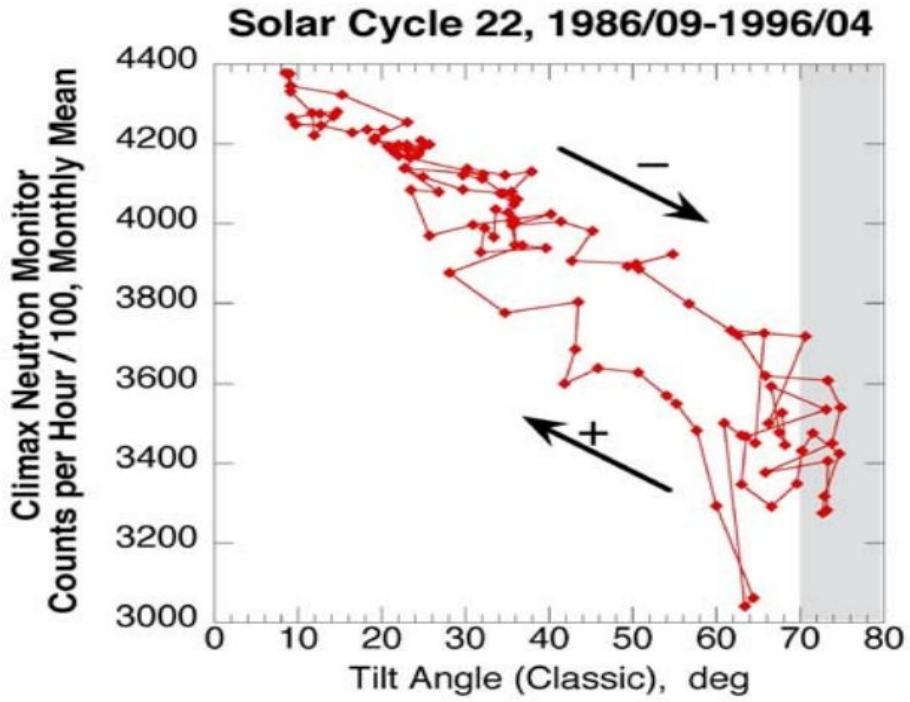

(a) Climax neutron monitor counts [Smith, 2006].

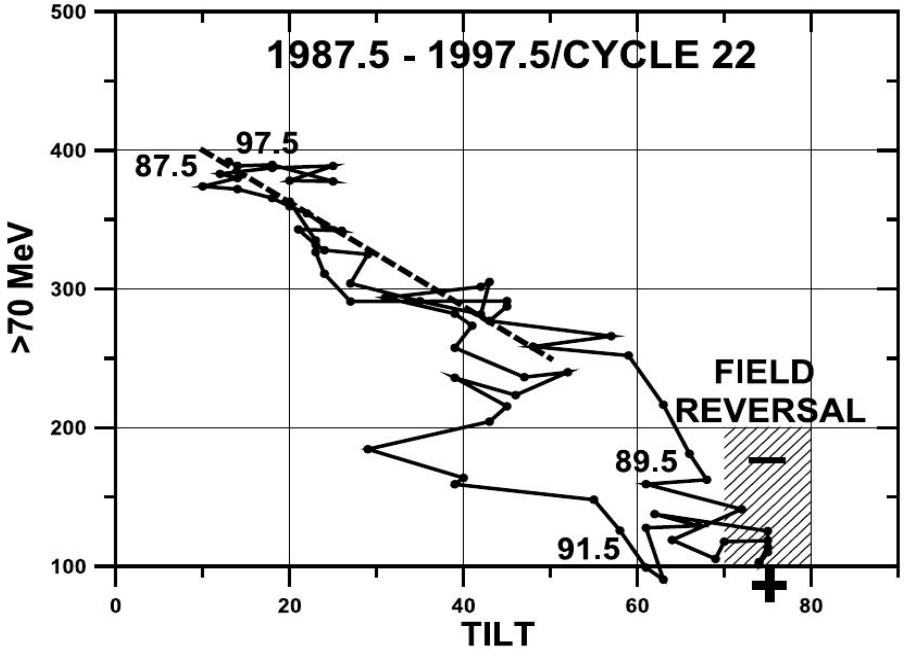

(b) IMP 8 >70 MeV intensities [Lockwood and Webber, 2005].

Figure 5.6: *Same as Figures 5.4 and 5.5, but for cycle 22, a negative/positive cycle.*

$\sim$1976 – 1986/7, a positive/negative polarity cycle. The top panel shows the Climax Neutron Monitor, with a cut-off rigidity of 2.99 GV [*Dorman*, 2006], while the bottom panel shows the *IMP 8* >70 MeV protons, with approximately 0.85 GeV (1.5 GV) median energy [*Webber and Lockwood*, 2001]. The shaded regions show where the tilt angle is above 70°. Except for absolute values, the general shape shown in the two panels is the same: starting at the top left of each figure, the intensity decreases slowly with increasing tilt angle until the tilt is $\sim$70°. At this time the overall solar magnetic polarity begins to change from positive to negative. During this period of maximum solar activity roughly 50 % of the overall intensity modulation occurs, and the tilt begins to decrease again. As the tilt angle becomes less than $\sim$20°, the intensities begin a rapid increase back to their maximum value. These observations are in qualitative agreement with Figure 5.3 and a clockwise intensity-tilt loop is formed. Figure 5.5 shows a part of cycle 23 from $\sim$ 1996/7 – 2005/7, another positive/negative cycle, again for neutron monitor data in the top panel and spacecraft data in the bottom panel. Again, the qualitative features are the same: although these data are incomplete, a general agreement with Figure 5.3 and 5.4 is evident. These two solar cycles behave as predicted by the drift model.

The situation is different, however, for the intervening cycle 22 from $\sim$ 1986/7 – 1996/7, a negative/positive polarity reversal cycle shown in Figure 5.6. The intensities decrease along a much steeper gradient until the field reversal from negative to positive begins. At this time more than 50 % of the overall modulation has already occurred and little additional decrease in intensities occurred during the period when the field polarity reverses. The intensities increase along roughly the same gradient line they followed during the decrease phase. Instead of rotating in an anti-clockwise sense, the intensities continue to rotate in a clockwise sense, contrary to expectation based on a simple drift picture, as shown in the right-hand panel of Figure 5.3.

5.4 Effective Tilt Angle And Data Binning

Most model predictions are generally based on steady-state numerical models because they are relatively easy to construct. However, the heliosphere as a whole is certainly not in a steady state for the duration of a solar activity cycle and a solar magnetic polarity cycle. During the time of over a year that it takes for the solar wind to reach the outer limits of the heliosphere, the heliospheric tilt angle, for example, can change significantly.

To account for the time dependence of the structure of the heliosphere, we use the concept of an effective tilt angle [see, e.g., *Nagashima and Morishita*, 1980]. This concept will be applied to other quantities as well in what follows. It takes the solar wind and the

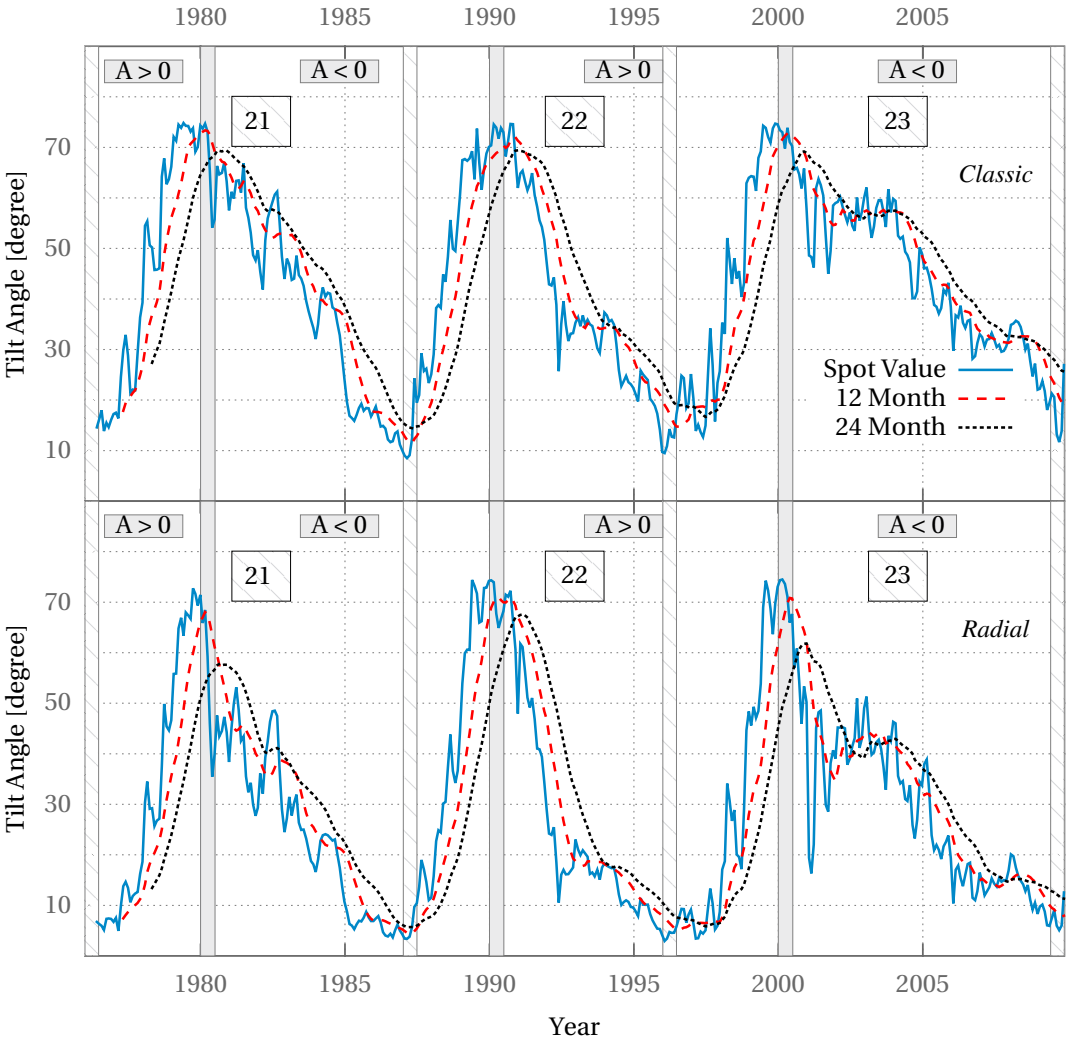

Figure 5.7: *The spot and effective tilt angle values for both the classic and radial tilt angle models, calculated with different windows, see text for details.*

HMF embedded in it well over a year to reach the outer limits of the heliosphere. Thus even if a cosmic-ray particle could transverse the whole heliosphere instantaneously it would still experience the last year's worth of the solar wind, magnetic fields and tilt angles. The intensity-tilt loops from *Lockwood and Webber* [2005] and *Smith* [2006] do not take this into account, as they associate cosmic-ray intensities with the tilt angle observed at the same time at or near Earth. What we propose is to associate the intensities measured at a certain time, with the average of at least the preceding year's worth of tilt angle values as measured at the Sun. This argument holds for any quantity that is measured at Earth and then propagates into the heliosphere embedded in the solar wind. Thus any intensity measured on a particular day must be associated with the running average of at least the previous year's worth of tilt angle, magnetic field and solar wind data.

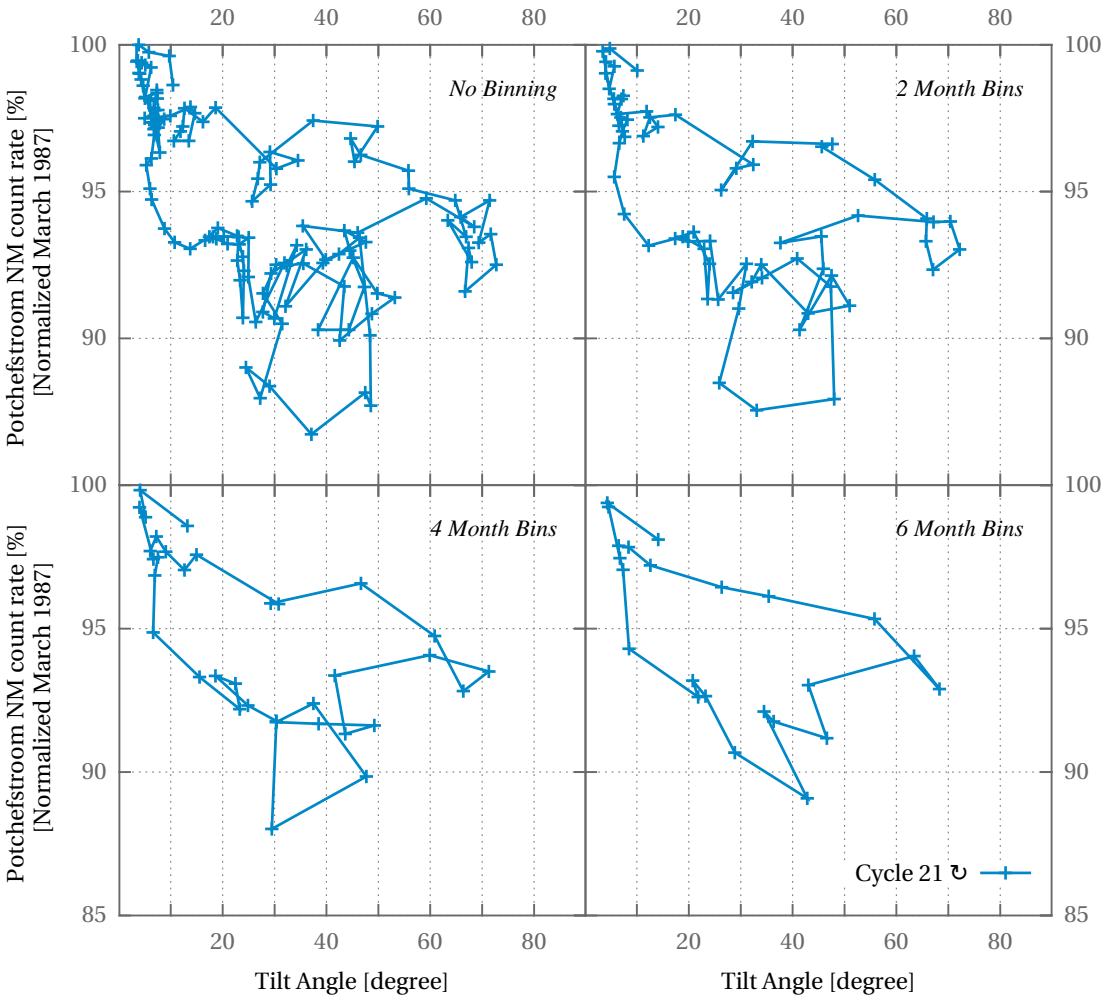

Figure 5.8: *Data binning of the Potchefstroom neutron monitor count rate as a function of tilt angle for solar cycle 21.*

Figure 5.7 shows the effective tilt angle for both the "classic" and "radial" tilt angle for three distinct cases. The spot value shows the tilt angle as it is measured, and the twelve and twenty four month effective tilt angles show the running average calculated over the twelve month and twenty four month window preceding the date shown, respectively. Both the "classic" and "radial" tilt angle exhibit the same behaviour in terms of the effective tilt angle values. The short-term variations in the tilt angle are smoothed out, which is to be expected since we are applying an average. A consequence of applying the effective tilt angle is that it leads to a time shift with respect to the original data (or a running average over the same period centred on the date shown in the graph). The time shift is one half of the period over which the effective tilt angle is calculated, thus taking a twelve month effective tilt angle is similar to taking a six month time shift. The reason for this factor of two difference is given in Appendix A.

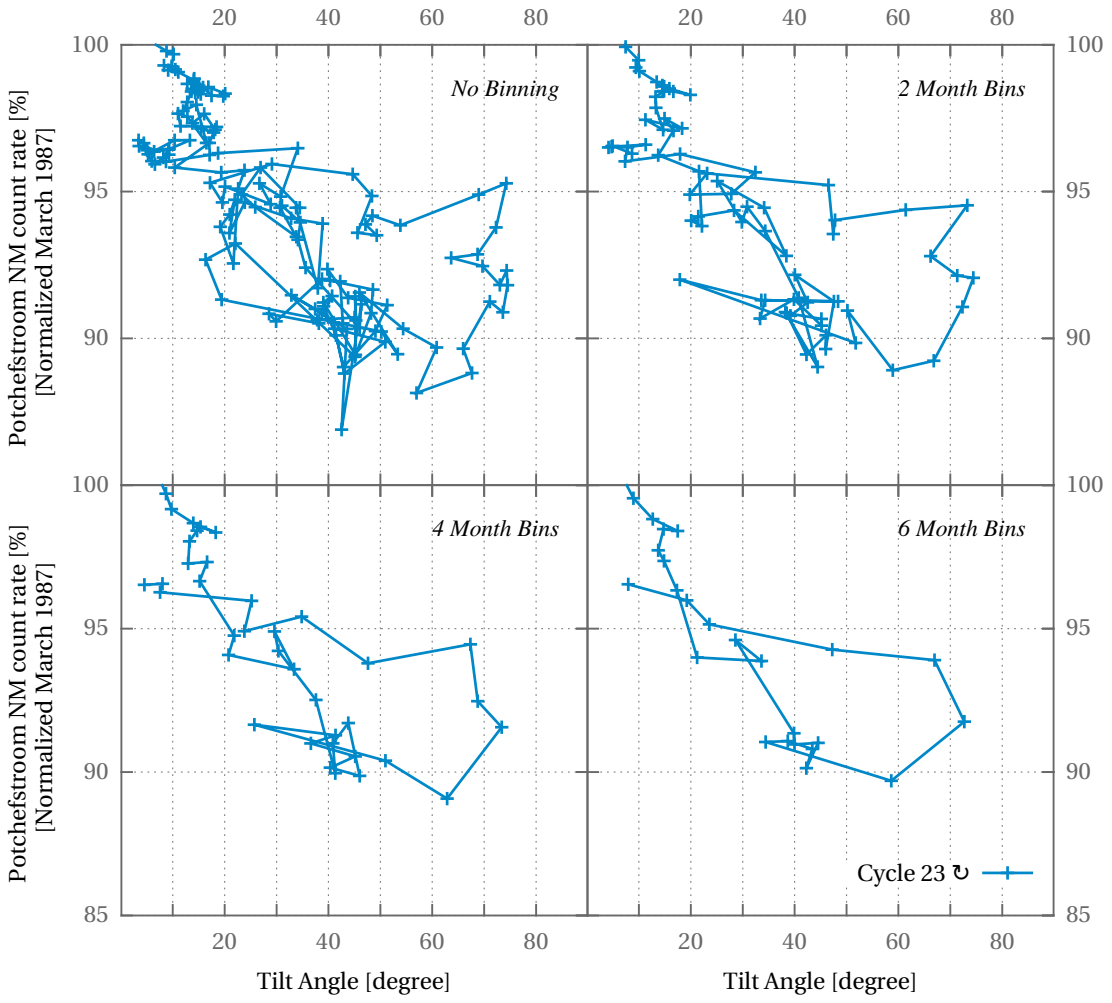

Figure 5.9: *Same as Figure 5.8 but for solar cycle 23.*

Since we are not interested in the short-term variations associated with Forbush and transient decreases, we bin the neutron monitor data to reduced such "noise" (which these phenomena are certainly not in other projects) and construct intensity-tilt loops that are easier to interpret. Figure 5.8 shows the Potchefstroom neutron monitor intensity-tilt loops for cycle 21. The top left-hand panel shows the data as is with no binning at all, and thus is our reference case. The top right-hand panel shows the two month data bins. The graph is much more clearer than the no-binning graph but still has a lot of features that can be associated with short-term decreases. The bottom left-hand panel shows the four month data bins. This graph is much clearer than both the no binning and the two month bins graphs. A lot of the short-term variations have been removed. The bottom right-hand panel shows the six month data bins. Almost all the information about the short-term variations has been removed and only the long-term variations remain.

Figure 5.9 shows data binning for cycle 23, a cycle similar in nature to cycle 21 shown in Figure 5.8. As we work through from the top left-hand panel to the bottom right-hand

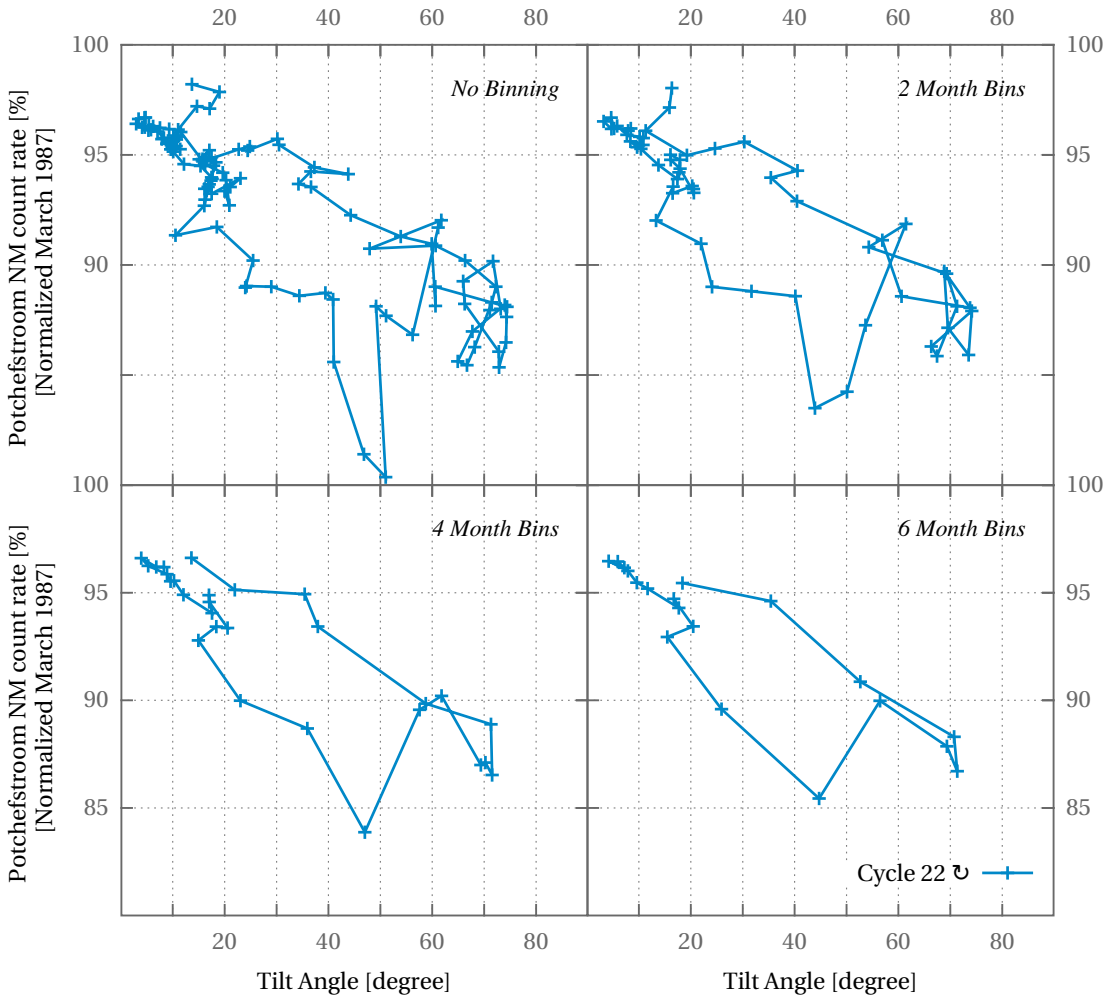

Figure 5.10: *Same as Figure 5.8 but for solar cycle 22.*

panel, we find that the behaviour is similar to that observed in Figure 5.8. There is a gradual reduction in noise and features that can be associated with short-term decreases as one moves from the two month data bins to the four month data bins and almost no short-term features left by the time we reach the six month data bins. Figure 5.10 shows the data binning for cycle 22. As in Figures 5.8 and 5.9 we find that there is reduced noise as we move from two month data bins to six month data bins. If we compare the data bins to each other through the different solar cycles, we find that two month data bins still have too many short term variations and the six month data bins run the risk of removing too much information. The four month data bins are the best suited for the present project, since they remove enough of the short-term variations but not so much as to risk changing the behaviour of the long-term variations.

Figure 5.11 shows the intensity-tilt loops for cycle 21. Each panel compares two different effective tilt angles. Each (intensity, tilt angle) datum is replaced by (intensity, effective tilt angle), and therefore moves horizontally. The top left-hand panel compares the spot

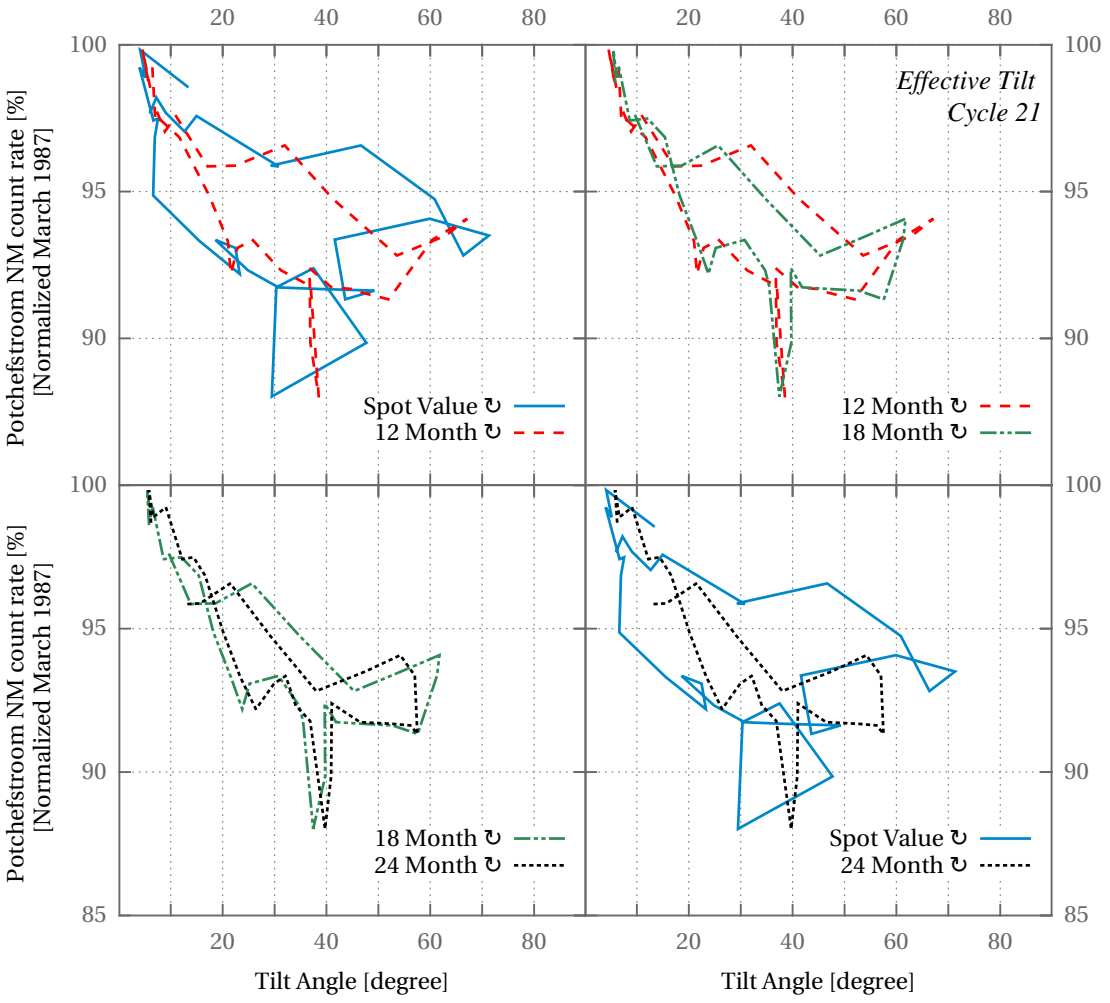

Figure 5.11: *Potchefstroom neutron monitor count rate as a function of effective tilt angle for solar cycle 21. The magnetic polarity change at solar maximum is from positive to negative. Note that there is a data gap at the start of the loop for a 24 month average of the tilt angle, because tilt angle data only became available in mid-1976, less that 24 months before the start of the cycle.*

value, which is the tilt angle as it is measured, with the 12 month effective tilt angle. The top right-hand panel compares the 12 month effective tilt angle with the 18 month effective tilt angle while the bottom left-hand panel compares the 18 month effective tilt angle with the 24 month effective tilt angle. The bottom right-hand panel compares the spot value to the 24 month effective tilt angle. Note that there is a data gap at the start of the loop for this average, because tilt angle data only became available in mid-1976, less than 24 months before the start of the cycle. Three features are apparent as we move from the spot value in the top left-hand panel to the 24 month effective tilt angle in the bottom right-hand panel. The first and simplest to explain is that there is smoothing of data, which is to be expected since the effective tilt angle is a running average. The second feature is that the larger the period over which the effective tilt

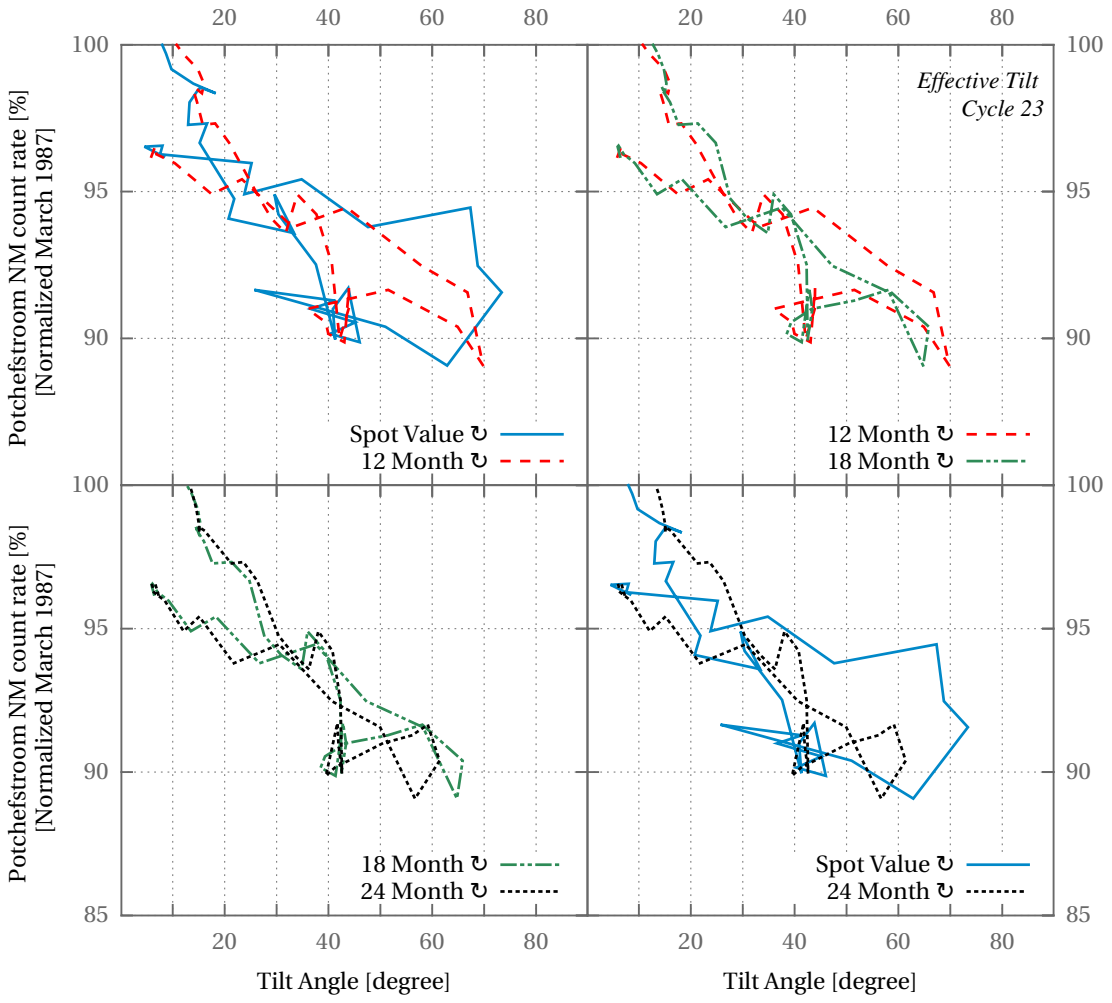

Figure 5.12: *Potchefstroom neutron monitor count rate as a function of effective tilt angle for solar cycle 23. The magnetic polarity change at solar maximum is from positive to negative.*

angle is calculated, the narrower the intensity loop. The third feature is that the loop progresses in a clockwise direction, as indicated in the legend.

Figure 5.12 shows the intensity-tilt loops for cycle 23, a cycle similar in nature to cycle 21 shown in Figure 5.11. The behaviour for cycle 23 when the effective tilt angle is applied, is the same as that for cycle 21 in that averaging the tilt angle over longer periods makes the loop narrower, and the net sense of rotation remains clockwise except in small secondary loops.

Cycle 22 shown in Figure 5.13, on the other hand, does not follow this behaviour. As the 12 month effective tilt angle is applied in the top left-hand panel, the intensity-tilt loop narrows, as in the case for cycles 21 and 23, but as the 18 month effective tilt angle is applied, the intensity-tilt loop crosses itself and effectively changes its sense of rotation from clockwise to anti-clockwise except for in the small secondary loop at large

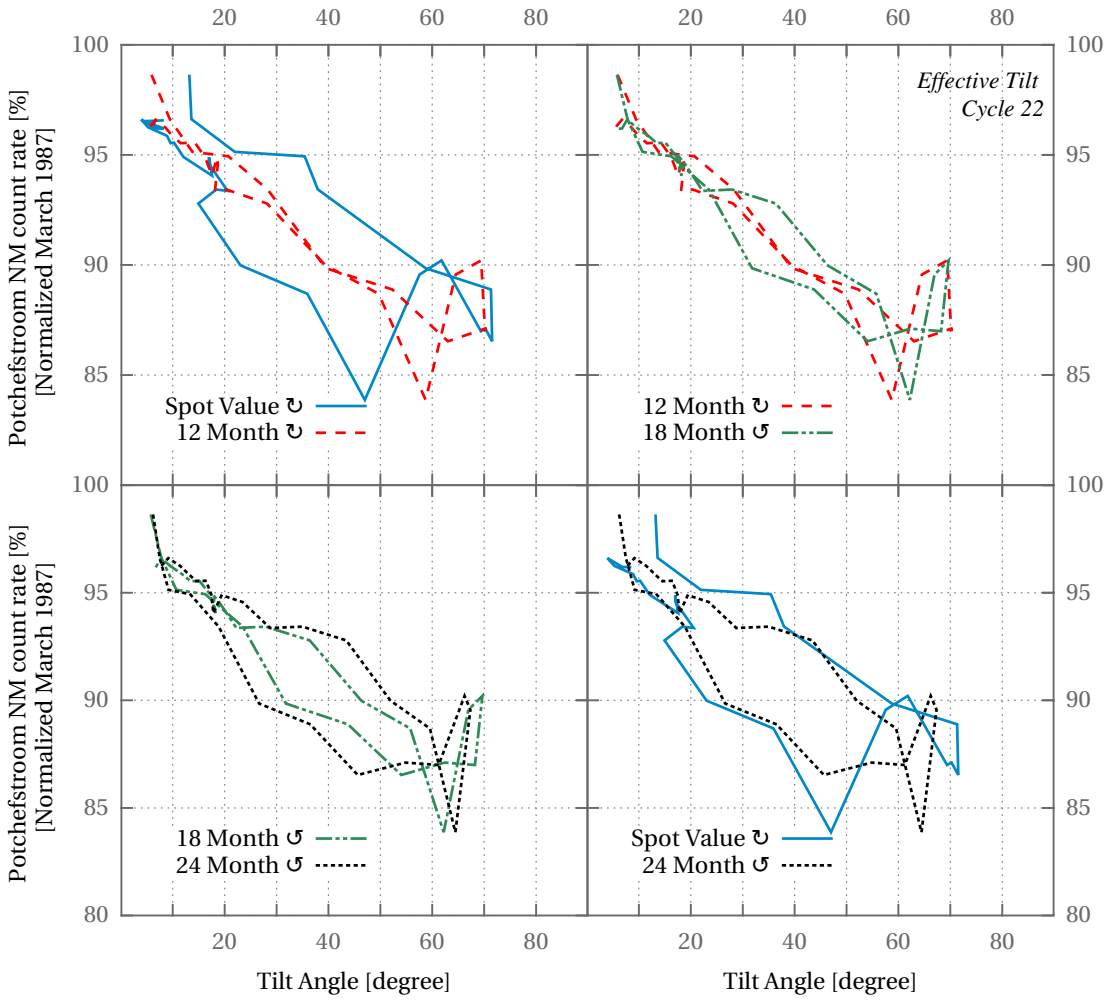

Figure 5.13: *Potchefstroom neutron monitor count rate as a function of effective tilt angle for solar cycle 22. The magnetic polarity change at solar maximum is from negative to positive. Note that in the top left panel at around 40°, the 12 month tilt angle average lines converge, overlap, and then diverge without crossing.*

tilt angles. Applying the 24 month effective tilt angle widens this new anti-clockwise intensity-tilt loop.

Results for the three solar cycles are now combined in Figure 5.14, so that their shapes and sizes are easily compared. While there are very obvious differences in the top left panel for spot values of the tilt angle, they become much less pronounced when an effective tilt is used. There is not that much to choose between the 12, 18, and 24 month graphs, but they seem to agree the most for 18 months, and this value will therefore be used in what follows. As shown in the individual Figures, the sense of rotation for 18 and 24 month is clockwise for odd cycles 21 and 23 when the polarity changes from positive to negative at solar maximum, and anti-clockwise for even cycle 22 when the polarity changes from negative to positive. Comparing this figure with Figure 5.3 for the predictions of a simple steady-state description of drifts, they are clearly not

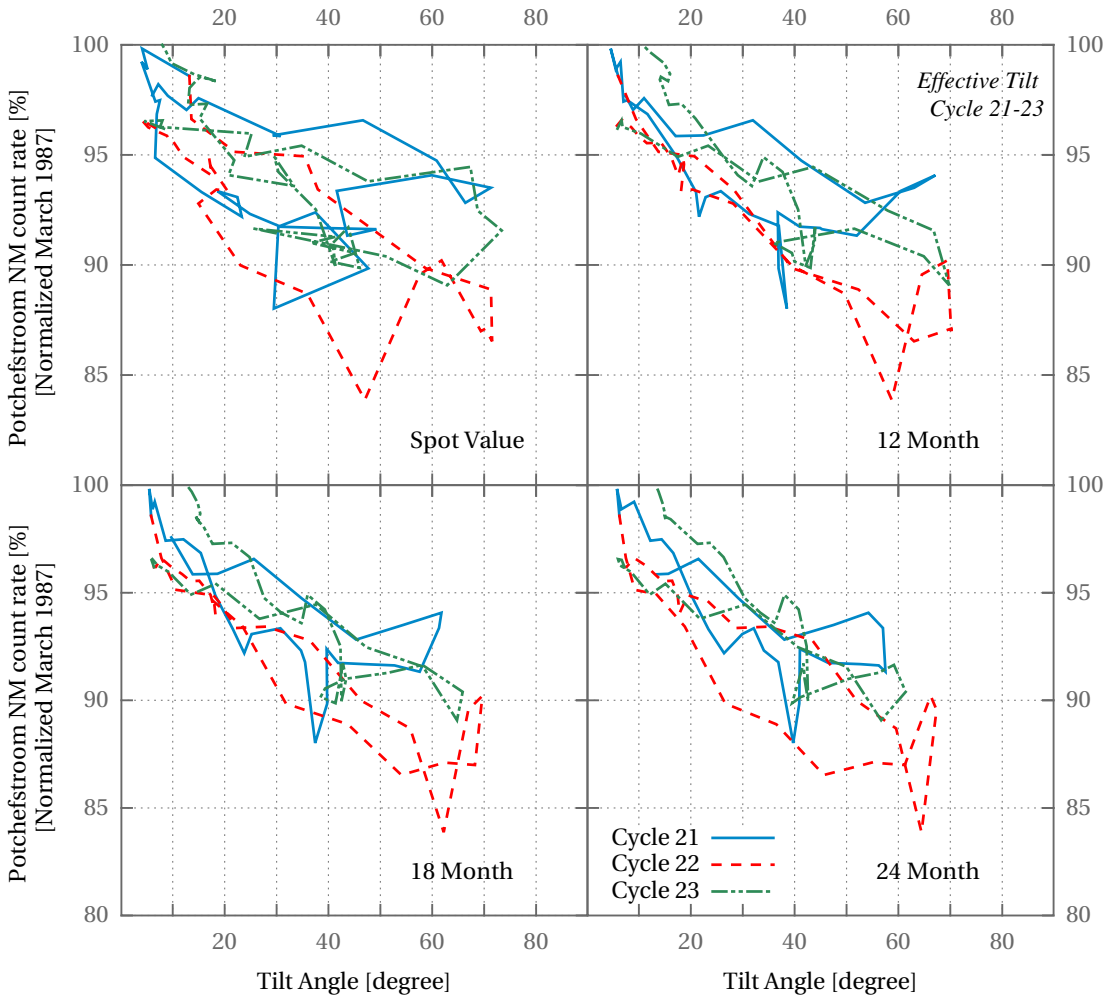

Figure 5.14: *Comparison of intensity-tilt loops for cycles 21, 22 and 23 for different effective tilt angle values. The solar magnetic polarity change is from positive to negative during odd cycles and from negative to positive during even cycles.*

identical, but are remarkably similar in terms of the general shape of the loops and their sense of rotation. This result suggests that if an appropriated cosmic-ray modulation model is used, either a time-dependent model or one that makes use of effective values of quantities that determine cosmic-ray modulation at Earth, intensity-tilt loops should agree with observations if the local values of the tilt angles are used, and with a simple steady-state drift model if effective values for the tilt angles are used.

To study the dependence of the intensity-tilt loops on cutoff rigidity, fourteen neutron monitors divided into four rigidity groups are studied. The original data were provided by Moraal [2012, private communication]. Figure 5.15 shows the comparison of four neutron monitors with a cutoff rigidity in the range of 0 GV to 1 GV. The top and bottom panels show the odd cycles 21 and 23, which are positive/negative magnetic polarity cycles and have a net clockwise sense of rotation. The middle panel shows

the even cycle 22, which is a negative/positive magnetic polarity cycle with a net anti-clockwise sense of rotation. Figures 5.16, 5.17 and 5.18 are the same as Figure 5.15 but for 1 GV to 4 GV, 4 GV to 7 GV and 7 GV to 14 GV cutoff rigidities, respectively. Considering the four figures as a whole, it is clear that the net sense of rotation follows the rule of being clockwise for odd cycles when the magnetic polarity changes from positive to negative at solar maximum, and anti-clockwise for even cycles when the polarity changes from negative to positive. There is however an indication that the agreement between the loops, for the chosen 18 month effective tilts, is best for the range 1 GV to 7 GV, and that the agreement is not as good for cutoff rigidities below and above this range. One would actually expect the time it takes for particles to reach Earth from interstellar space to depend on their energy. However, because of the limited scope of the present project, only a single period for averaging will be considered.

5.5 Summary And Conclusions

A simple idealized drift model is utilized to study cosmic-ray intensity dependence on tilt angle. The model shows what might be expected assuming that cosmic-ray intensities are more sensitive to changes in tilt angle during negative than positive magnetic polarity cycle. The intensity-tilt loops for this model have the same size when the solar magnetic polarity changes from positive to negative and from negative to positive. The only difference is the sense of rotation along the loop, with the positive to negative change being clockwise and the negative to positive change being anti-clockwise.

Contrary to the idealized steady-state drift model, intensity-tilt loops for observational data from the Climax neutron monitor [*Smith*, 2006] and the >70 MeV *IMP 8* proton data set [*Lockwood and Webber*, 2005] have the same sense of rotation for the positive to negative magnetic polarity change as for the negative to positive change. The loop sizes for the positive to negative change are different from those for the negative to positive change, with the positive to negative loops much wider than the negative to positive loops.

The concept of an effective tilt angle is introduced to emulate time dependence. The effective tilt angle approach associates the intensities measured at a certain time with the average of at least the preceding year's worth of tilt angles. The effective tilt angle computed over a 18 month window is found to be the most appropriate for the current study.

Intensity-tilt loops for neutron monitors, using the effective tilt angle, are found to become narrower for the odd cycles 21 and 23 but become wider for the even cycle 22.

The sense of rotation for cycles 21 and 23 are clockwise while that for cycle 22 becomes anti-clockwise, if the effective tilt angle is calculated for a window of 18 months or longer. There is an indication that this single window is not appropriate for all rigidities.

The fact that observed intensity-tilt loops resemble that for an idealized steady-state drift model when an appropriate effective tilt angle is used, is a new result that helps to improve our understanding of the role of the heliospheric current sheet. It is, for example, difficult to understand why intensities should decrease for both positive to negative and negative to positive magnetic polarity changes, as shown in Figures 5.4 to 5.6, where the local tilt angle is used. While Figure 5.2 should be adjusted to account for propagation time of tilt angles, it does show that one would expect intensities to decrease when going from a positive polarity (gradient- and curvature drift direction towards Earth implying easy access by means of drift) to a negative one (gradient- and curvature drift direction away from current sheet and only current sheet drift towards Earth implying less easy drift access). Conceptually, one would then expect intensities to increase for the opposite polarity change, and this becomes apparent in data if the effective tilt angle and not the local value at Earth is used.

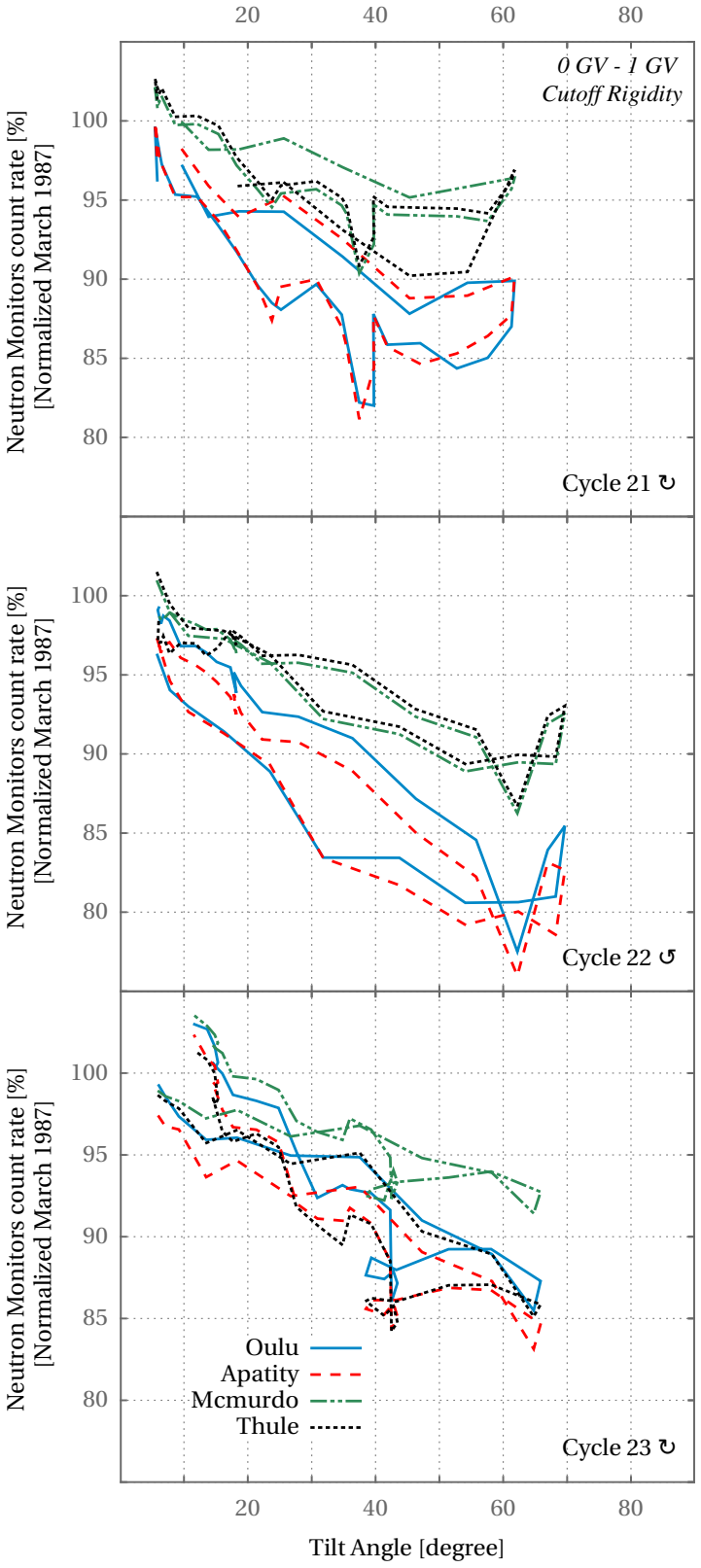

Figure 5.15: *Comparison of intensity-tilt loops for neutron monitors with cutoff rigidities between 0 GV to 1 GV for an effective tilt angle taken over 18 months. The solar magnetic polarity change is from positive to negative during odd cycles and from negative to positive during even cycles.*

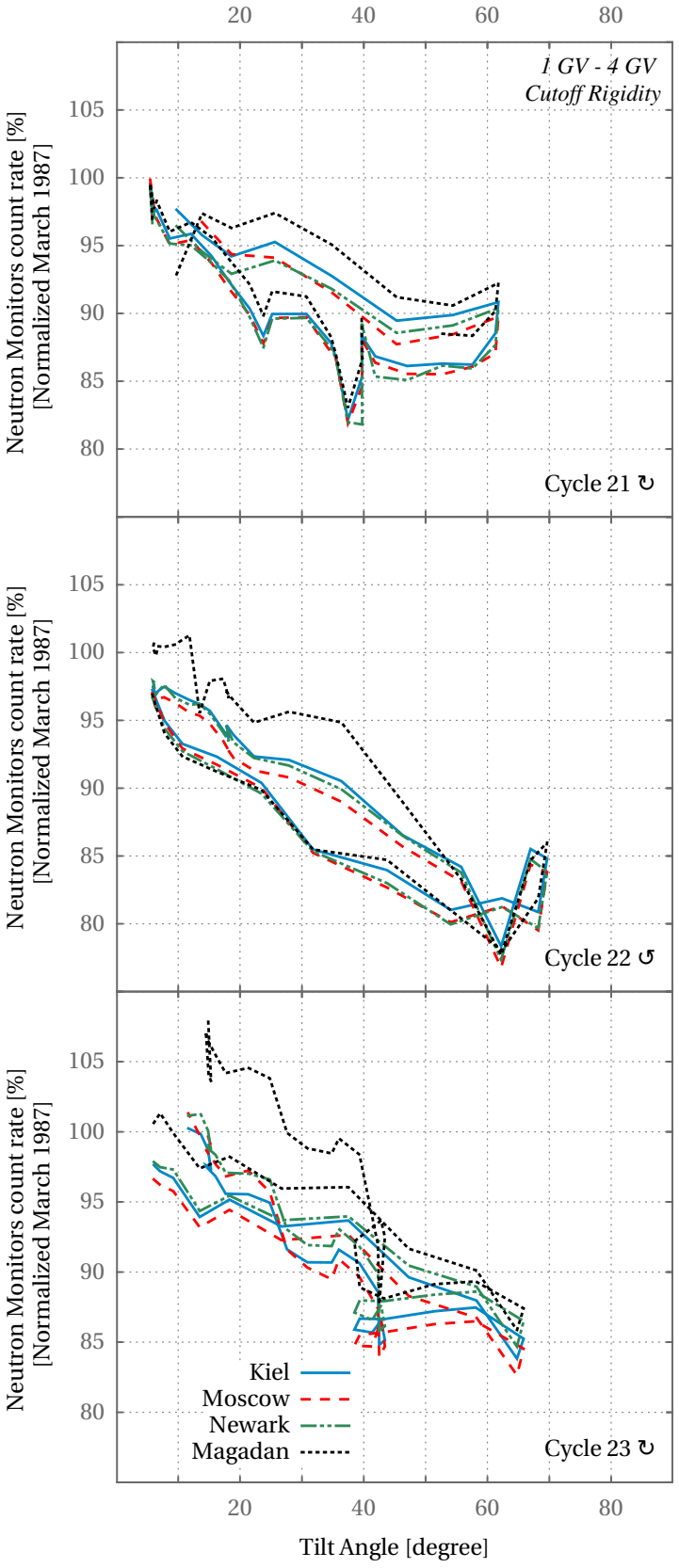

Figure 5.16: *Same as Figure 5.15 but for cutoff rigidities between 1 GV to 4 GV.*

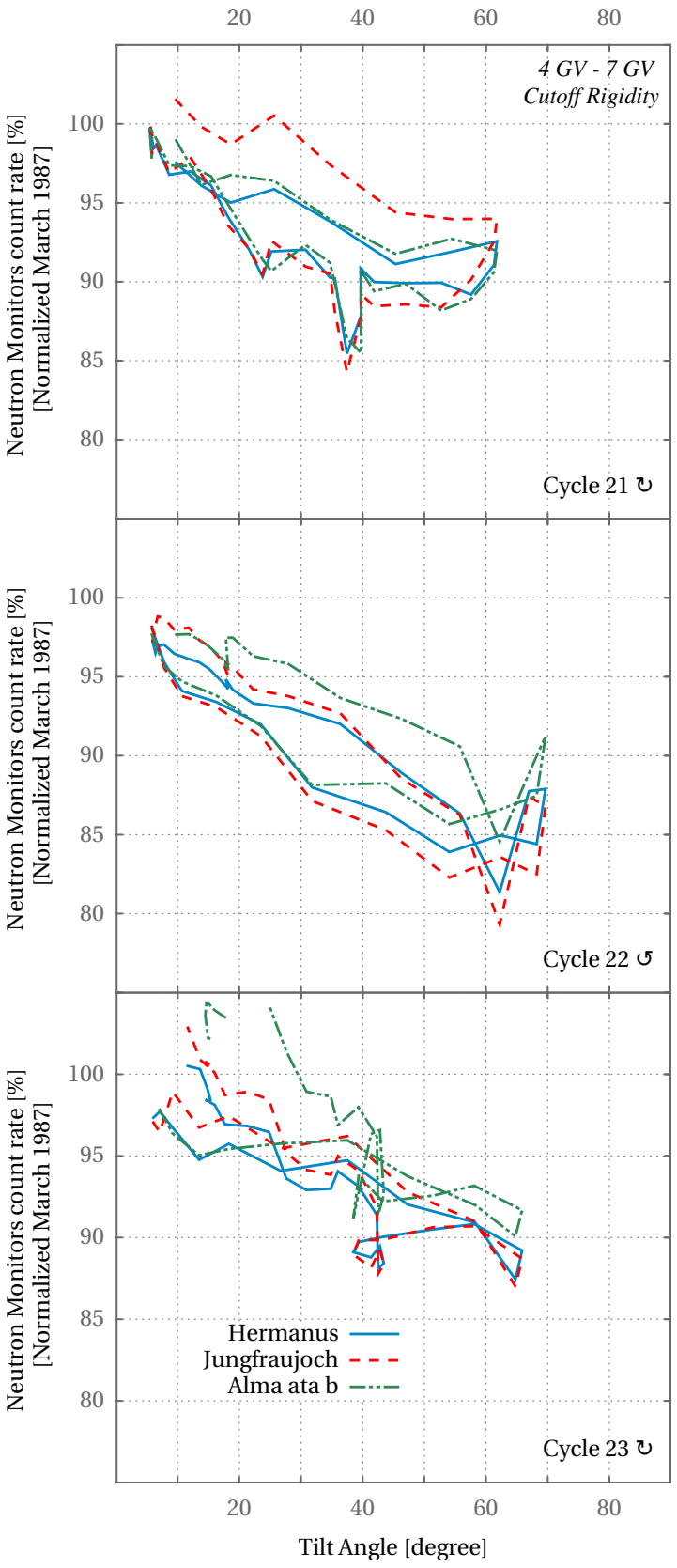

Figure 5.17: *Same as Figure 5.15 but for cutoff rigidities between 4 GV to 7 GV.*

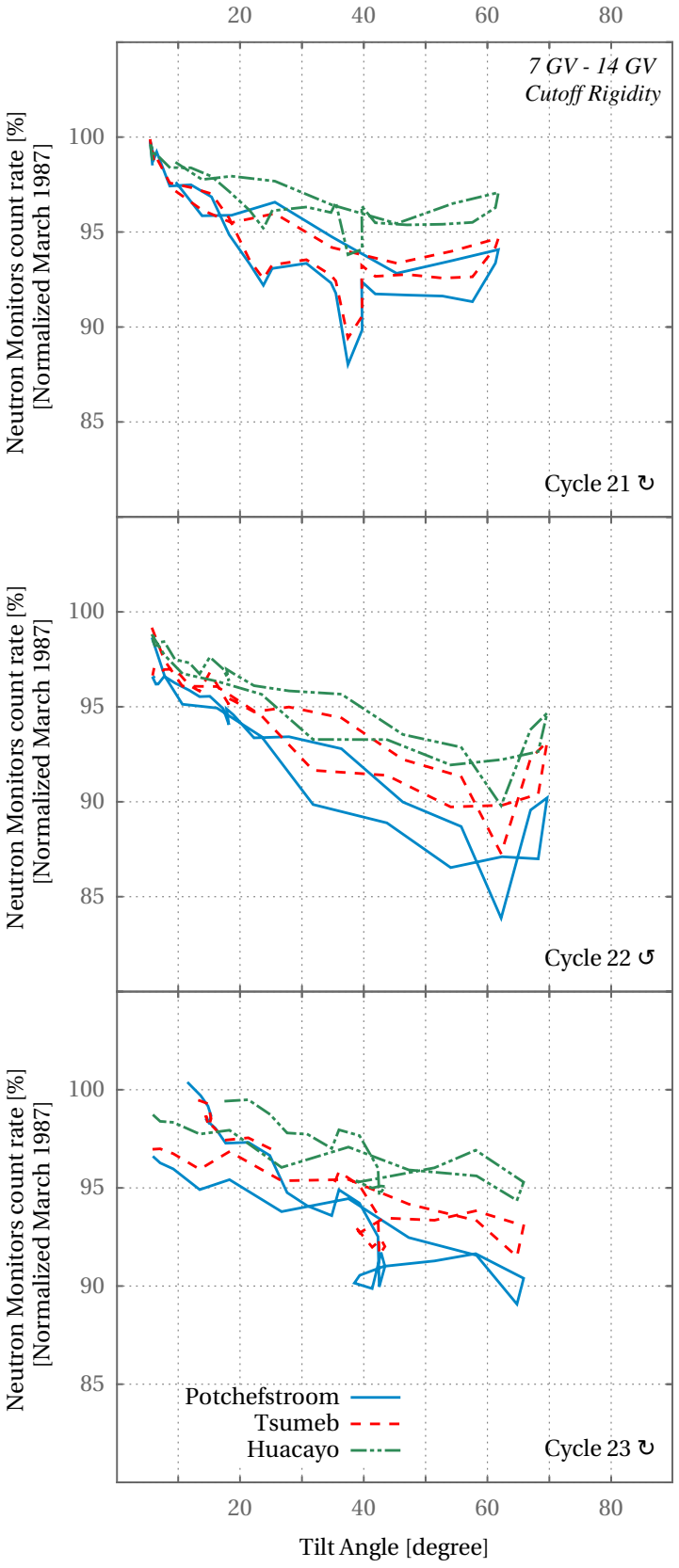

Figure 5.18: *Same as Figure 5.15 but for cutoff rigidities between 7 GV to 14 GV.*

CHAPTER 6

Modelling Long-Term Cosmic-Ray Modulation

6.1 Introduction

In this chapter, a three-dimensional, cosmic-ray modulation code, described by *Hattingh and Burger* [1995], *Burger and Hattingh* [1995], and *Hattingh* [1998] is applied to solve the *Parker* [1965] cosmic-ray transport equation (Equation 2.15) for galactic cosmic rays, neglecting local sources. The equation is solved in a frame corotating with the solar equator, using the relation [*Kóta and Jokipii*, 1983]

$$\frac{\partial f_0}{\partial t} + (\mathbf{\Omega} \times \mathbf{r}) \cdot \nabla f_0 = 0. \tag{6.1}$$

to eliminate the explicit time dependence. This procedure yields a steady-state form

$$\nabla \cdot (\mathbf{K} \cdot \nabla f_0) - (\mathbf{v}_d + \mathbf{V}^*) \cdot \nabla f_0 + \frac{1}{3} (\nabla \cdot \mathbf{V}^*) \frac{\partial f_0}{\partial \ln p} = 0, \tag{6.2}$$

with $\mathbf{V}^* = \mathbf{V}_{sw} - \mathbf{\Omega} \times \mathbf{r}$ the solar wind speed in the corotating frame, and $\mathbf{\Omega}$ the solar equatorial rotation rate, assumed to be constant.

While this equation is solved for the omnidirectional cosmic-ray distribution function $f_0(\mathbf{r}, p, t)$, cosmic-ray energy spectra are usually specified in terms of the differential intensity j_T with respect to kinetic energy, with the dimensions of particles per unit

area, per unit time, per unit solid angle, per unit kinetic energy per nucleon [e.g. *Moraal*, 2011]. The differential intensity is related to the omnidirectional distribution function by $j_T = p^2 f_0(\mathbf{r}, p, t)$. Note that if the transport equation is written in terms of particle rigidity P, then $j_T = P^2 f_0(\mathbf{r}, P, t)$ [e.g. *Moraal*, 2011].

The local interstellar spectrum (LIS) for protons used in the present study, is that proposed by *Burger et al.* [2008], and is given as a function of rigidity (in GV) in units of particles.m^{-2}.s^{-1}.sr^{-1}.MeV^{-1} such that

$$j_{LIS} = 19.0 \frac{(P/P_0)^{-2.78}}{1 + (P_0/P)^2}, \tag{6.3}$$

with $P_0 = 1\,\mathrm{GV}$. Note that throughout what is to follow, the parallel mean free path, perpendicular mean free path, and drift scale discussed in Section 4.3 were used (Equations 4.22; 4.23; and 4.26 with 4.28 – 4.30, respectively). For the required turbulence quantities, simplified expressions for results obtained by *Engelbrecht* [2013], where the *Oughton et al.* [2011] turbulence transport model was used, were employed. The procedure to find the spatial dependence of the turbulence quantities by means of parametrized fits will be described in Section 6.2.

The present study assumes a radius of 100 AU for a spherical heliosphere, neglecting both the termination shock and heliosheath. *Caballero-Lopez et al.* [2004] studied solutions of the Parker transport equation with and without a termination shock. They conclude that the effects of a termination shock on galactic cosmic rays are not dramatic, even in the heliosheath. While their modelling of the heliosheath may not be fully realistic, their results do show that the intensities near Earth are affected very little if at all by the inclusion of a termination shock and a heliosheath. Observations of galactic cosmic rays by the *Voyager 1* spacecraft from early 2002 to mid-2005, including its crossing of the termination shock in mid-December 2004 at a heliocentric distance of 94 AU, are shown in Figure 6.1 [*Stone et al.*, 2005]. High-energy galactic protons do not appear to be greatly affected by the termination shock crossing, confirming the predictions of e.g. *Caballero-Lopez et al.* [2004]. While there is significant modulation within the heliosheath [see, e.g., *Stone et al.*, 2013], knowledge about turbulence quantities in this region is incomplete, and observations are only available in the region traversed by the two *Voyager* spacecraft. The bulk of the heliosheath will never be explored, and one would have to rely on models that describe it. As was pointed out in Section 2.4, results from such models can differ dramatically. An *ab initio* approach to describe modulation in the heliosheath is not yet possible, and neglecting this region if one is studying mainly neutron monitor data, seems justified at the time of writing.

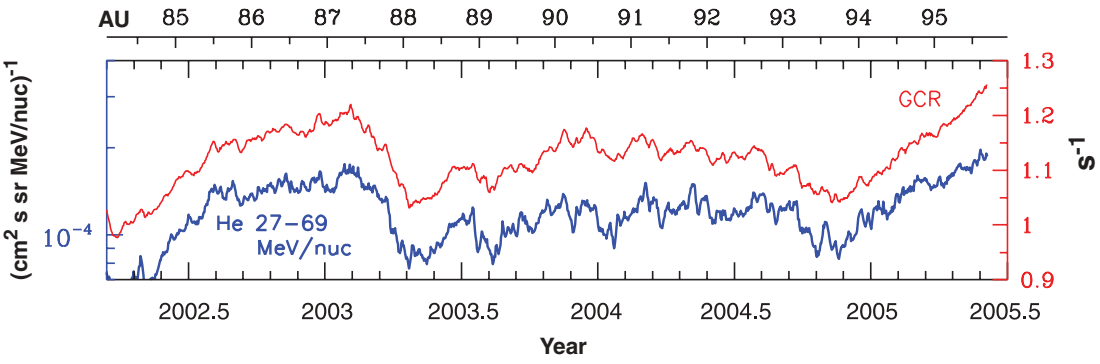

Figure 6.1: *Five-day moving averages of He ion and of galactic cosmic-ray intensity, the latter with $E > 70\,MeV/nucleon$, adapted from Stone et al. [2005]. The He intensity is due to anomalous cosmic rays. Voyager 1 crossed the termination shock and entered the heliosheath at a heliocentric distance of 94 AU.*

A *Parker* [1958a] HMF is assumed, and the effective values for the tilt angle and solar wind speed as described in Section 5.4 are used. As for the turbulence quantities, the procedure is to find parametric fits to the variances and correlation scales modelled by *Engelbrecht* [2013], shown in Figure 4.3, as well as for the 2D ultrascale. For the latter quantity, the approach of *Burger and Visser* [2010] was used. The parameters that describe these quantities were then adjusted to find best fits for cosmic-ray energy spectra at Earth for three solar minimum periods. In the next section, we first show the fits obtained for the cosmic-ray energy spectra, since they acted as motivation for the required turbulence quantities, and then describe the turbulence quantities themselves.

6.2 Energy Spectra For Successive Solar Minima

Figure 6.2 shows computed galactic proton energy spectra as function of kinetic energy at Earth for the solar minimum periods of 1987, 1997 and 2009 during periods of positive, negative and positive solar magnetic polarity, respectively. Fairly accurate data fits can be achieved for all three solar minimum periods. To put this result into perspective, one should keep in mind that an energy spectrum for an $A > 0$ solar minimum at Earth that is larger than the energy spectrum for an $A < 0$ solar minimum at low energy was viewed for many decades as a characteristic of a drift model [see, e.g., *Potgieter*, 1984; *Hattingh*, 1998; *Langner*, 2004; *Krüger*, 2006, and references therein]. This is indeed the case for the 1997 $A > 0$ and the 1987 $A < 0$ solar minimum spectra for all energies below 0.3 GeV. Note that these two spectra cross at around 0.3 GeV, leading to higher intensities during $A < 0$ minima than during $A > 0$ minima, as observed at neutron monitor energies (see Figure 2.6). The fact that the observed intensity at low energies is clearly higher for the 2009 $A < 0$ solar minimum than for the 1997 $A > 0$

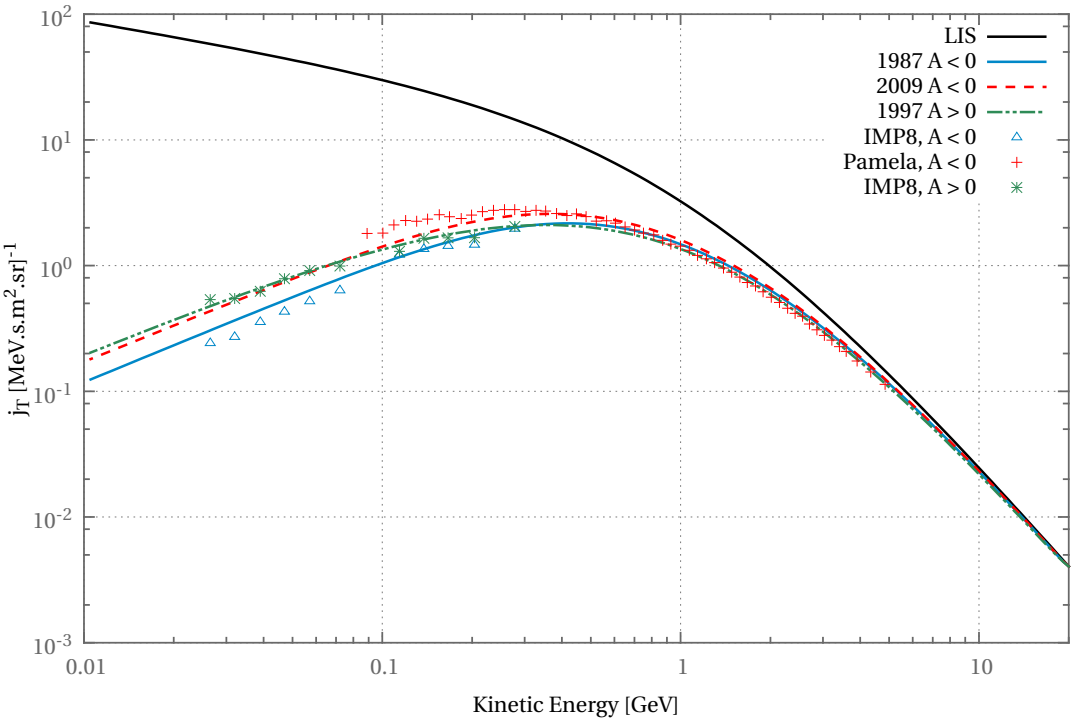

Figure 6.2: *Computed galactic proton energy spectra as function of kinetic energy. Spacecraft data are shown for 1987, 1997 and 2009 solar minima, where the former two were measured by IMP 8 [McDonald et al., 1992] and BESS97 [Shikaze et al., 2007], respectively, and the latter by PAMELA [Adriani et al., 2013]. Fits for the three different periods are shown with the lines of the same colour as the symbols that denote the observations.*

solar minimum is unusual, and the 2009 solar minimum is often referred to as such. Of the three, the fit for this spectrum is the worst. However, the modelled 2009 spectrum is above the other two for energies above about 0.07 GeV. As will be shown in what follows, the turbulence input to the present modulation model is based on reasonable assumptions and guided by observations. We can therefore conclude that the higher than expected cosmic-ray intensity during the 2009 solar minimum can be qualitatively linked to turbulence parameters that differ from solar minimum to solar minimum.

6.2.1 Magnetic Variance

When one considers the magnetic variances shown in Figure 4.3, it seems that a simple but reasonable fit should be possible if power laws are used. The spatial dependence of the variance will therefore be modelled as a two-stage power law as function of radial distance r, as

	Magnetic field [nT]	Variance [nT^2]	Solar wind [km s^{-1}]	Tilt angle [degree]
1987	5.8	8.3	462	4.1
1997	5.7	9.4	416	4.5
2009	4.4	5.7	402	11.2

Table 6.1: *Effective values at Earth for the magnetic field, total variance, solar wind speed and the tilt angle. Observational values for the magnetic field and variance were supplied by Nel [2013, preliminary results, private communication]. The solar wind and tilt angle values were obtained as described in Section 5.4.*

$$\chi = \chi_0 \left(\frac{r}{r_0}\right)^{\epsilon_1} \left[\frac{1+\left(\frac{r}{r_c}\right)^f}{1+\left(\frac{r_0}{r_c}\right)^f}\right]^{\frac{(\epsilon_2-\epsilon_1)}{f}}, \tag{6.4}$$

where χ is the value of either the slab or the 2D variance throughout the heliosphere, χ_0 is its value at Earth at a radial distance r_0, ϵ_1 and ϵ_2 are the exponents of the two different radial dependencies, r_c is the radial distance where the dependence on r changes from r^{ϵ_1} to r^{ϵ_2} and $f\,(\geq 0)$ determines how sharp this transition is. Large values for f result in abrupt transitions, while smaller values result in smoother transitions.

Parametric fits to the two-component turbulence transport model are shown in Figure 6.3 for the three selected periods of solar minimum activity. The current approach is to model the turbulence quantities as if they were independent of latitude. This means that values are often closer to the high-latitude fast solar wind results modelled by *Engelbrecht* [2013] rather than the ecliptic values. Table 6.1 shows the effective values at Earth used for the magnetic field, variance, solar wind speed and the current sheet tilt angle for the three periods. The turbulence quantities in Table 6.1 were supplied by Nel [2013, preliminary results, private communication]. Note that these values may differ somewhat from those used in Section 6.3 for long-term modulation: to find fits to cosmic-ray energy spectra during a few solar minima is rather different from finding a fit to variations in the cosmic-ray intensity at a few energies, but spanning a period of close to four decades.

The top panel of Figure 6.3 shows the total variance for the 1987, 1997 and 2009 solar minima, while the middle and bottom panels show the 2D and slab variances, respectively. Table 6.2 shows the values used in Equation 6.4, as well as the respective slab and 2D fractions. As can be seen from Tables 6.1 and 6.2, the 1987 and 1997 solar minimum energy spectra in Figure 6.2 can be fitted if the spatial dependence of both the slab and the 2D variance are the same, as well as the slab to 2D ratio, although the magnitudes differ slightly due to the different values required at Earth. For the 2009

		χ_0	ϵ_1	ϵ_2	f	r_c [AU]
δB^2_{slab}	1987	$20\,\% \times \delta B^2$	-3.0	-1.0	8.0	7.0
	1997	$20\,\% \times \delta B^2$	-3.0	-1.0	8.0	7.0
	2009	$15\,\% \times \delta B^2$	-3.0	-1.0	8.0	10.0
δB^2_{2D}	1987	$80\,\% \times \delta B^2$	-3.0	-3.6	6.0	25.0
	1997	$80\,\% \times \delta B^2$	-3.0	-3.6	6.0	25.0
	2009	$85\,\% \times \delta B^2$	-3.0	-3.6	6.0	30.0

Table 6.2: *Values used in Equation 6.4 to obtained parametric fits of the variances shown in Figure 4.3.*

minimum, a smaller slab fraction is used, but the same power law indices can be used, although the transition from one power law to the other now occurs at larger radial distances. Note that the transition of the slab variance to a flatter radial dependence occurs at a radial distance related to the size of the ionization cavity, which is about 10 AU, and beyond which pick-up ion formation injects energy into the slab component [see, e.g., *Engelbrecht*, 2013]. This flattening leads to the slab component dominating in the outer heliosphere, whereas the 2D component dominates in the inner heliosphere. The smaller total variance compared to the other two minima leads to a significantly lower variance throughout the heliosphere for the 2009 minimum compared to the other two solar minima.

6.2.2 Correlation Scales And 2D Ultrascale

The spatial dependence of the slab correlation scale is the most complicated of all the turbulence quantities considered. Similar to the variance, it is modelled as a combination of power laws as function of radial distance, but now in three stages, each with its own power-law index:

$$\lambda_{c,slab} = 2.5\lambda^{Earth}_{c,2D}\left(\frac{r}{r_0}\right)^{\epsilon_1}\left[\frac{1+\left(\frac{r}{r_{c1}}\right)^{f_1}}{1+\left(\frac{r_0}{r_{c1}}\right)^{f_1}}\right]^{\frac{(\epsilon_2-\epsilon_1)}{f_1}}\left[\frac{1+\left(\frac{r}{r_{c2}}\right)^{f_2}}{1+\left(\frac{r_0}{r_{c2}}\right)^{f_2}}\right]^{\frac{(\epsilon_3-\epsilon_2)}{f_2}}, \tag{6.5}$$

where $\lambda^{Earth}_{c,2D}$ is the value of the 2D correlation at Earth, at radial distance r_0, in AU; ϵ_1, ϵ_2 and ϵ_3 are the exponents of the three different radial dependencies; r_{c1} and r_{c2} are the radial distance where the dependence on radial distance changes from r^{ϵ_1} to r^{ϵ_2} to r^{ϵ_3}; and $f_1\,(\geq 0)$ and $f_2\,(\geq 0)$ determine how sharp these transitions are. Large values for f result in abrupt transitions, while smaller values result in smoother transitions. Note

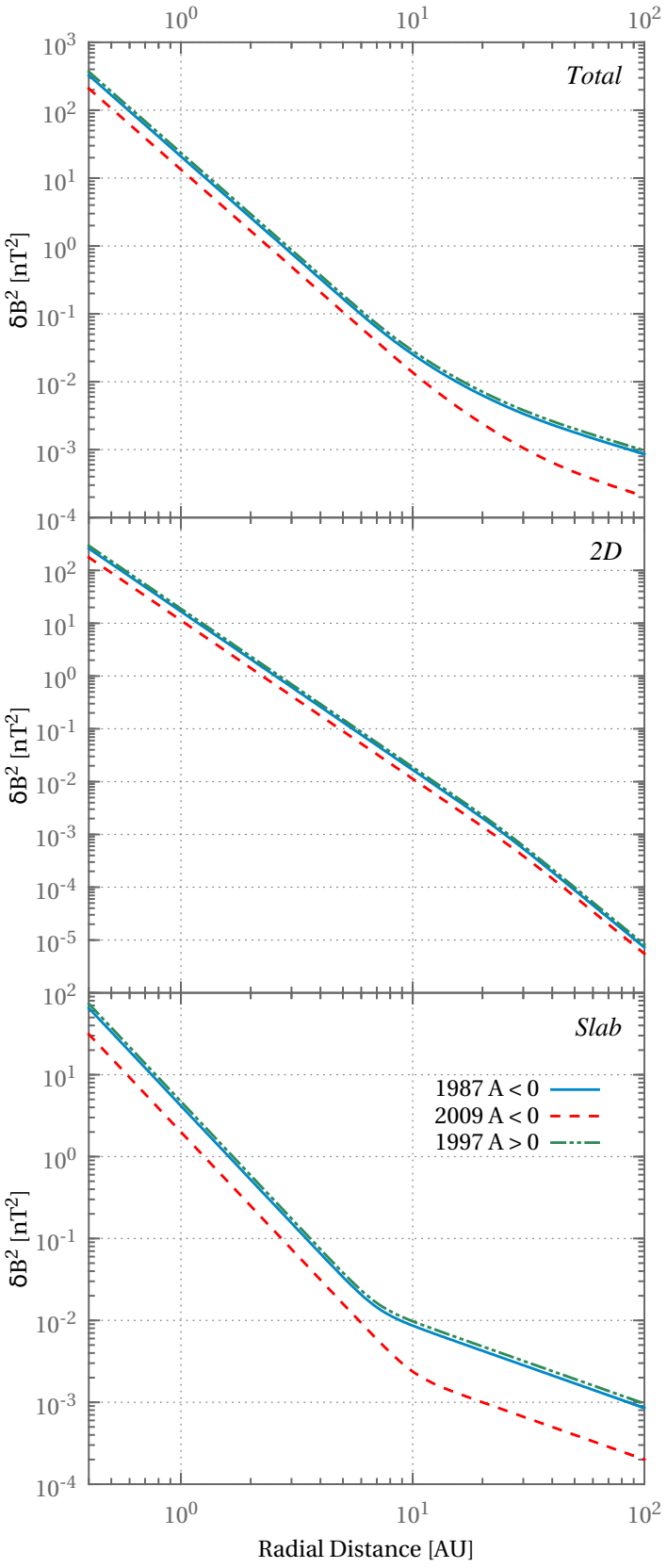

Figure 6.3: *Variances associated with the slab and 2D components, as well as the total variance, for the 1987, 1997 and 2009 solar minima.*

	$\lambda_{c,2D}^{Earth}$ [AU]	ϵ_1	ϵ_2	ϵ_3	f_1	f_2	r_{c1} [AU]	r_{c2} [AU]
1987	3.7×10^{-3}	0.4	−2.5	1.2	3.0	2.50	7.0	25.0
1997	5.0×10^{-3}	0.4	−2.5	1.2	3.0	2.50	7.0	25.0
2009	5.6×10^{-3}	0.4	−2.5	1.2	3.0	2.50	10.0	30.0

Table 6.3: *Values used in Equations 6.5 to obtained parametric fits of the correlation scales shown in Figure 4.3.*

that to reduce the number of parameters (if only by one) the value of the slab correlation scale at Earth is set at 2.5 times the value of the 2D correlation scale at Earth, motivated by observational results [*Weygand et al.*, 2009]. Values for the parameters used for the three solar minima are given in Table 6.3.

In contrast to the slab correlation scale, the 2D correlation scale is modelled as a single power law, with index 0.5 [*Burger et al.*, 2008]. Its value in AU is given by

$$\lambda_{c,2D} = \lambda_{c,2D}^{Earth} \sqrt{\frac{r}{r_0}}, \tag{6.6}$$

with its value at Earth for the three solar minima given in Table 6.3. These same values also appear in the expression for the 2D ultrascale, which is modelled as

$$\lambda_{u,2D} = \sqrt{180 \lambda_{c,2D}^{Earth} \lambda_{c,2D}}, \tag{6.7}$$

with units AU. This expression for the ultrascale is based on an approximation by *Burger and Visser* [2010], and implies that the scale at which the 2D spectrum starts to decrease at small wavenumbers is 500 times larger than the 2D correlation scale. As was noted in Subsection 4.3.1 we assume turbulence spectra that are flat in the energy range. The decrease in the 2D spectrum is therefore in contradiction to this assumption, but is necessary to ensure that the ultrascale does not diverge [*Matthaeus et al.*, 2007]. *Burger and Visser* [2010] state that the effect of the decrease in the 2D spectrum on the perpendicular mean free path, for parameter values close to those used in the present project, is around 30 %. Given all the other uncertainties, this is a reasonable value.

Figure 6.4 shows the slab and the 2D correlation scales, and the 2D ultrascale. Values of the constants used in the expressions above are given in Table 6.3. The top panel shows the slab correlation scale. The increase of this scale in the inner heliosphere is consistent with the decay of the slab fluctuation energy in the bottom panel of Figure 6.3. At the same radial distance as the noted increase in the radial profile of the slab variance, the fit shows the influence of the pickup-ions on the behaviour of the slab correlation scale in the outer heliosphere, where it displays a marked decrease as function of radial distance.

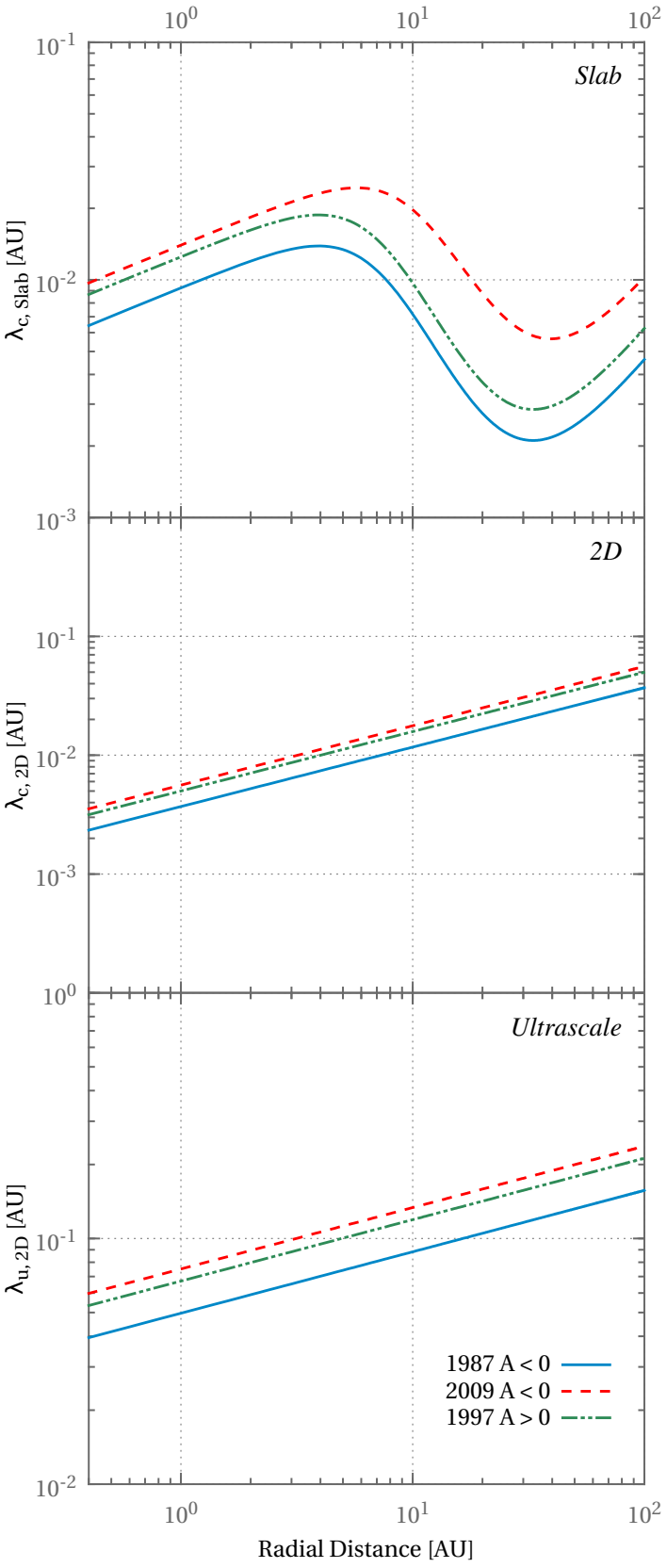

Figure 6.4: *Correlation length scales associated with the slab and 2D components, as well as the ultrascale, for the 1987, 1997 and 2009 solar minima.*

The fit also takes into account that the slab correlation scale modelled by *Engelbrecht* [2013] relaxes in the outer heliosphere to the resonant scale, the scale corresponding to the wavenumber at which energy due to the formation of pickup-ions is injected into the slab fluctuation spectrum [see, e.g., *Engelbrecht*, 2013]. The middle panel shows the monotonically increasing 2D correlation scale, which is consistent with the consistently decreasing 2D variance shown in the middle panel of Figure 6.3. The bottom panel shows the 2D ultrascale for an omnidirectional energy spectrum with a flat energy range [*Engelbrecht*, 2013; *Engelbrecht and Burger*, 2013]. Note that the 2D ultrascale is by construction always larger than the 2D correlation scale.

As noted above, in this simplified approach we assume that all the turbulence quantities are independent of heliographic latitude. While data in the ecliptic plane can be analysed over periods spanning several continuous solar activity cycles, such data are simply not available at high latitudes, excluding the few latitude scans by the *Ulysses* spacecraft. If a latitude dependence for the turbulence quantities is required, (strong) assumptions will in any case have to be made. We do, however, have a solar wind speed and magnetic field magnitude that varies with solar heliographic latitude, and consequently the mean free paths and drift scale discussed in the next section do vary with latitude.

6.2.3 Mean Free Paths And Drift Scale

The top panel of Figure 6.5 shows the parallel mean free paths for the three solar minimum periods for protons at Earth, as function of rigidity, calculated from Equation 4.22. The magnetic field magnitude in this expression is given in Table 6.1 and Equation 6.4 is used to model the spatial dependence of slab variance. The wavenumber k_{min} follows from Equation 4.21, with the spatial dependence of the slab correlation scale given by Equation 6.5. As illustrated in the figure, the general behaviour of the parallel mean free path is a $P^{1/3}$ dependence at low rigidities, changing to P^2 at high rigidities. This transition occurs where the magnitude of the second term in square brackets of the parallel mean free path Equation 4.22 is equal to one. The rigidity dependence is $P^{1/3}$ if the second term is much larger than one, which is when R given in Equation 4.20 is small. This in turn occurs where the rigidity is sufficiently small and/or the magnetic field magnitude is sufficiently large. Conversely, the rigidity dependence is P^2 if the second term is much smaller than one, which is when R given in Equation 4.20 is large. This in turn occurs where the rigidity is sufficiently large and/or the magnetic field magnitude is sufficiently small. The parallel mean free paths for 1987 and 1997 are very similar for rigidities up to about 6 GV with $\lambda_{\parallel}$ in 1997 ∼5 % larger than during 1987 at the lowest rigidity. Above 6 GV the 1987 parallel mean free path becomes ∼25 % larger than that for 1997. The parallel mean free path for 2009 is always larger than for

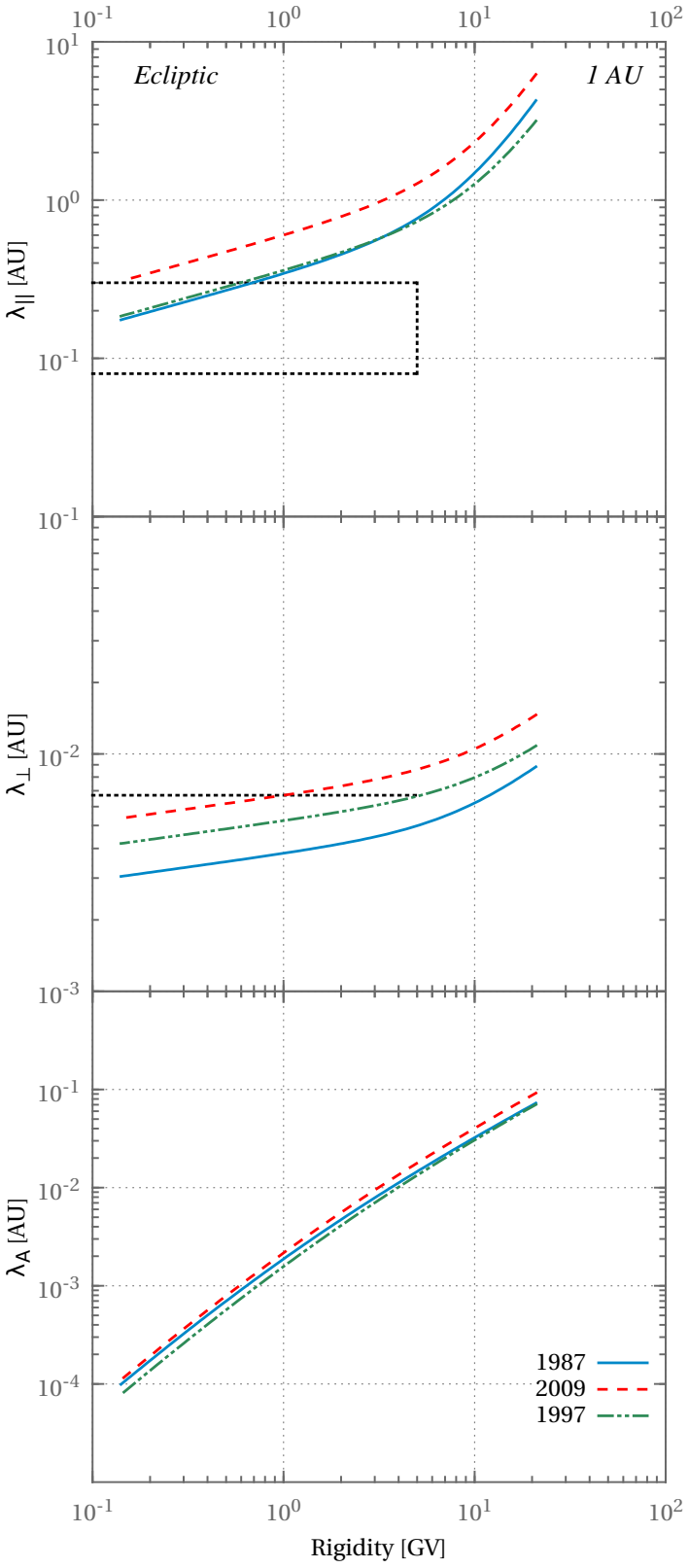

Figure 6.5: *Parallel and perpendicular mean free paths, along with the drift scale, shown as function of rigidity at 1 AU. The Palmer (1982) consensus ranges for the parallel and perpendicular mean free paths are indicated by the dotted box and dotted line in the top and middle panels, respectively.*

the other two periods, by ∼66 % at low rigidities, increasing to ∼97 % compared with 1997 at 20 GV, and being ∼46 % higher than 1987. The 1987 and 1997 parallel mean free paths are within the Palmer consensus range below ∼0.7 GV.

The middle panel of Figure 6.5 shows the perpendicular mean free paths at Earth, calculated from Equation 4.23. The parallel mean free path discussed above is used in this expression. The magnetic field magnitude is again given in Table 6.1, while the 2D variance for the three solar minima is given in Equation 6.6. The figure shows that the perpendicular mean free paths remain relatively flat for low rigidities, scaling as $\sim P^{0.1}$, this changing to $\sim P^{0.5}$ at high rigidities. Note that the rigidity dependence of $\lambda_\perp$ follows from the cube root of $\lambda_\parallel$, and consequently the dependence at higher rigidities than those shown in the figure will approach $P^{2/3}$. They are within the Palmer consensus range and are in qualitative agreement with the findings of *Burger et al.* [2000]. Unlike the parallel mean free paths there is a clear difference between the 1987 and 1997 perpendicular mean free paths, with the 1997 perpendicular mean free path being ∼38 % larger than the 1987 one at low rigidities and ∼22 % larger at high rigidities. The 2009 perpendicular mean free path is again always larger than those for the two other periods. It is larger by ∼76 % at low rigidities and by ∼65 % at high rigidities compared to 1987. It is ∼30 % larger than the 1997 perpendicular mean free path for all rigidities.

The bottom panel shows the drift scale λ_A, calculated from Equation 4.26 with inputs from Equations 4.28 – 4.30. The ultrascale required in Equation 4.29 is given in Equation 6.7, all other quantities used are referred to above. At low rigidities, where reduction due to turbulence is significant, it scales as $\sim P^{1.6}$. It approaches the weak-scattering limit (Equation 4.25) at the highest rigidities, where the scaling is $\sim P$. The 1987 drift scale is ∼28 % larger than the 1997 one at low rigidities and the difference decreases to ∼3 % larger at high rigidities. The 2009 drift scale is ∼40 % larger than the 1997 drift scale at low rigidities and ∼30 % larger at high rigidities.

The top panel of Figure 6.6 shows the parallel mean free paths at 100 AU, where they all display a P^2 rigidity dependence, due to the small magnetic field magnitude in the outer heliosphere (see discussion above). The 2009 parallel mean free path at low rigidities is ∼100 % and 200 % larger than the 1987 and 1997 parallel mean free paths, respectively, with the differences decreasing to ∼80 % and ∼180 % larger at high rigidities, respectively.

The middle panel shows the perpendicular mean free paths, which display a $\sim P^2$ rigidity dependence below ∼0.2 GV, beyond which they flatten out to display a $\sim P^{0.6}$ rigidity dependence. The 2009 perpendicular mean free path below ∼0.2 GV is ∼170 % and 120 % larger than the 1987 and 1997 perpendicular mean free paths, respectively, and this difference decreases to ∼95 % and 65 % larger at high rigidities. The exact turning

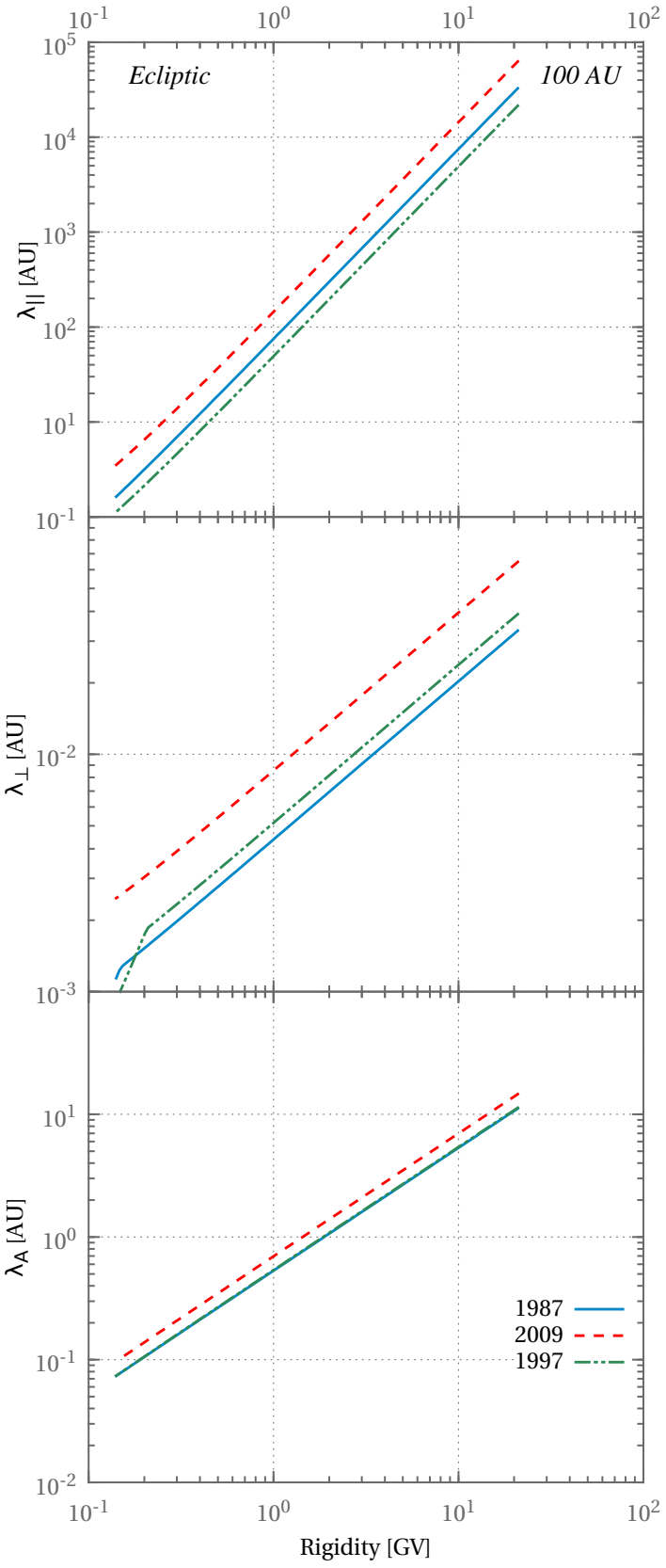

Figure 6.6: *Parallel and perpendicular mean free paths, along with the drift scale, as function of rigidity at 100 AU.*

point for the changeover in rigidity dependence depends on the 2D correlation scale. This is in line with the analysis *Shalchi et al.* [2004] did of the NLGC perpendicular mean free paths they derived. They showed that when $\lambda_\perp \lambda_\parallel \ll 3\lambda_{c,2D}^2$, their perpendicular mean free path would be proportional to the parallel mean free path. When $\lambda_\perp \lambda_\parallel \ll 3\lambda_{c,2D}^2$ they showed that $\lambda_\perp \approx \lambda_\parallel^{1/3}$.

The drift scales in the bottom panel of Figure 6.6 display a $\sim P$ dependence, in line with the weak scattering approximation, due to the low levels of turbulence in the outer heliosphere. The difference between the 1987 and 1997 drift scale is only a few percent, with the value during 1997 the larger one. The 2009 drift scale is ∼30 % larger than during the other two periods for all rigidities.

Figure 6.7 shows the mean free paths as function of radial distance. The 2009 and 1997 parallel mean free paths shown in the top panel have a $\sim r^{1.4}$ radial dependence within 30 AU, beyond which they start to flatten out. The 1987 parallel mean free path has a $\sim r^{1.4}$ radial dependence within 6 AU, beyond which this increases to $\sim r^{1.6}$ before flattening out beyond ∼30 AU. The 1997 parallel mean free path is ∼5 % larger than the 1987 parallel mean free path at Earth, but is ∼52 % smaller at 100 AU. The 2009 parallel mean free path is ∼75 % larger than the 1987 parallel mean free path at Earth, and ∼93 % and 194 % larger than the 1987 and 1997 parallel mean free paths at 100 AU, respectively. Note that the changes in the slope of these lines occur where there are changes in the slope of the slab correlation scale, up to and around 10 AU, and around 30 AU, as shown in Figure 6.4. The smaller radial distances referred to above are also where the slab variance has a change in slope.

The middle panel of Figure 6.7 shows the perpendicular mean free path. Below 5 AU all perpendicular mean free paths display a $\sim r^{0.4}$ radial dependence. At larger radial distances, the 2009 and 1987 perpendicular mean free path display a $\sim r^{0.17}$ radial dependence, while during 1997 $\lambda_\perp$ has a $\sim r^{0.1}$ dependence. Beyond 40 AU all perpendicular mean free paths display a $\sim r^{-0.7}$ dependence. The 2009 perpendicular mean free path is about 28 % and 76 % larger than the 1997 and 1987 perpendicular mean free paths at Earth, respectively. This increases to about 66 % and 95 % at 100 AU, respectively.

In the bottom panel of Figure 6.7, we have the drift scale which shows an $\sim r^2$ dependence close to Earth, which relaxes to an $\sim r$ dependence beyond 5 AU. At Earth the 2009 drift scale is ∼15 % and 38 % larger than the 1987 and 1997 drift scales. At 100 AU it is ∼30 % larger than the 1987 and 1997 drift scales. Note that the slight depressions between 20 AU and 30 AU are where the slope of the slab correlation scale changes.

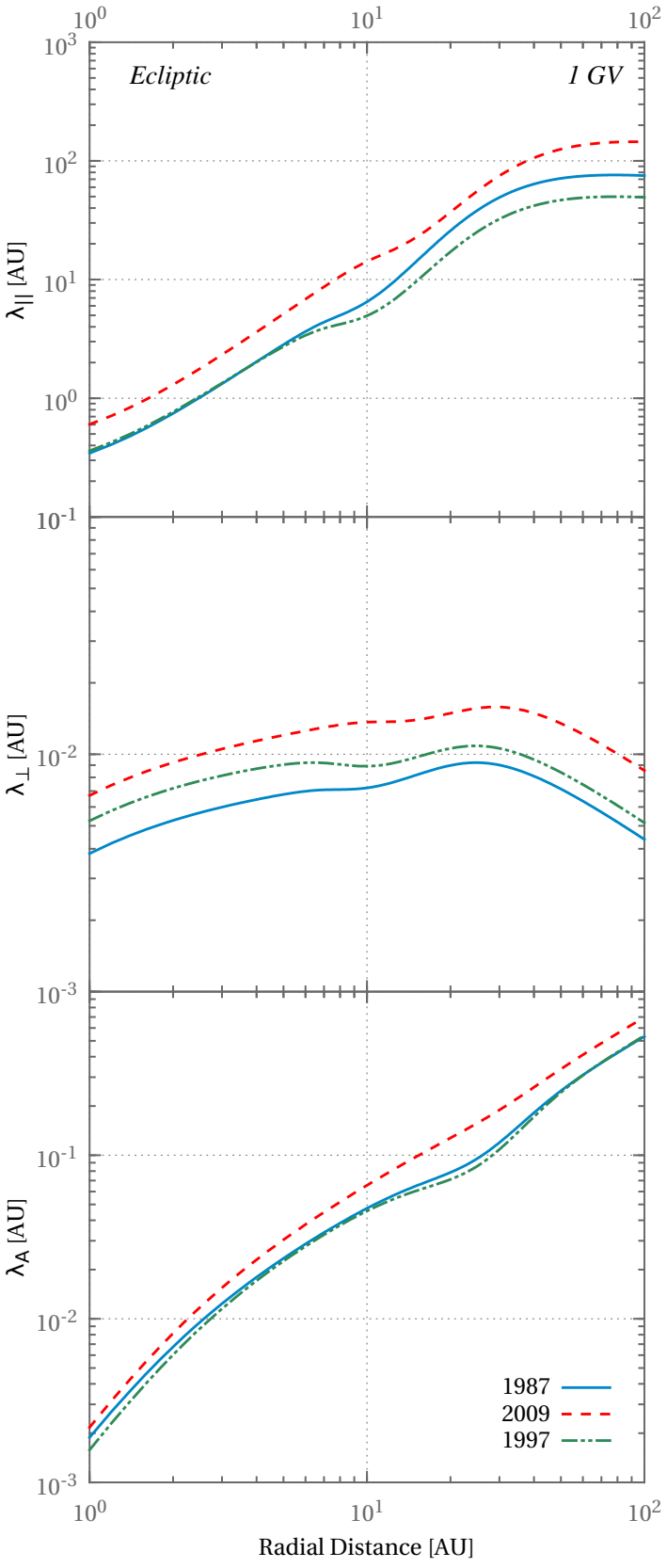

Figure 6.7: *Parallel and perpendicular mean free paths, along with the drift scale, as function of radial distance in the ecliptic plane.*

6.3 Long-Term Modulation

It has been increasingly recognised that the large-scale structure of the heliospheric magnetic fields, including a wavy current sheet, must be taken into account in models describing the modulation of galactic cosmic rays over the 11-year solar activity and 22-year solar magnetic cycle [see, e.g., *Svalgaard and Wilcox*, 1974; *Kóta and Jokipii*, 1983; *Hoeksema*, 1989; *Smith*, 1990; *Le Roux and Potgieter*, 1992; *Ferreira and Potgieter*, 2003]. Model predictions are often based on steady-state models. However, the structure of the heliosphere and the HMF are anything but stationary, as discussed in Section 2.6 and 5.4. During the time of over a year that it takes the solar wind to reach the outer limits of the heliosphere, the inclination of the HCS can change significantly, especially during periods of high solar activity. Furthermore, the increase in tilt angle during periods of increasing solar activity is more rapid than the decrease during periods of decreasing solar activity, as shown in Figure 5.1 and 5.7, and discussed in Section 5.1.

The objective in this section is to model the long-term behaviour of high-energy cosmic-ray intensities at Earth qualitatively, without considering energy spectra explicitly. This means that we will not attempt to match the intensities obtained in Section 6.2 for the three solar minima considered there, and consequently values that we employ for turbulence quantities may also differ from those presented in that section, although not significantly. To study the problem of long-term modulation in detail and self-consistently requires a time-dependent approach with more knowledge of turbulence throughout the heliosphere and at all phases of solar activity than is currently available. We must therefore make assumptions.

Three parameters for which long-term observations at Earth are available are the tilt angle, magnetic field and solar wind speed. For each of the three, effective values were calculated by means of 18-month running averages for the period preceding each cosmic-ray observation, as was done for the tilt angle as shown in Figure 5.7. However, we also need turbulence quantities as discussed in Section 6.2. We have a good idea how the magnetic variance behaves as function of solar cycle [see, e.g., *Smith et al.*, 2006], but such analyses are not available for the correlation scales and ultrascale as used in the present study. To model the temporal behaviour of these three quantities at Earth, we first consider the magnetic variance. *Bieber et al.* [1993] find that the low-frequency spectral level follows the mean magnetic field squared remarkably closely. We assume that this is valid at all frequencies, and model the total variance at Earth as

$$\delta B_o^2 = 0.15 B_o^2 \tag{6.8}$$

ϵ_1	ϵ_2	ϵ_3	f_1	f_2	r_{c1} [AU]	r_{c2} [AU]
0.4	−2.4	1.2	4.0	3.0	10.0	30.0

Table 6.4: *Values used in Equations 6.5 to obtained parametric fits for the long term slab correlation scale.*

To model the temporal dependence of the correlation lengths is more problematic. Figure 4.3 shows that the correlation scales increase as the magnetic variance decreases. This is obviously a spatial dependence and not a temporal one. However, lacking more guidance we assume that the temporal dependence will show a similar inverse relationship as the spatial dependence. We therefore model the 2D correlation scale at Earth as

$$\lambda_{c,2D}^{Earth} = 3.3 \times 10^{-2} \left(\frac{1\,\mathrm{nT}}{B_o} \right) \tag{6.9}$$

and the spatial dependence as

$$\lambda_{c,2D} = \lambda_{c,2D}^{Earth} \left(\frac{r}{r_0} \right)^{0.6}. \tag{6.10}$$

The spatial dependence is different from that used in the study of solar minima because although not shown in the current study, using 0.6 instead of 0.5 for the radial dependence of $\lambda_{c,2D}$ gave better agreement for latitudinal gradients with observations. The ultrascale used here is given by

$$\lambda_{u,2D} = \sqrt{3.6\lambda_{c,2D}}. \tag{6.11}$$

Note that the ultrascale in Equation 6.11 implies a small-wavenumber decrease in the 2D turbulence spectrum at larger scales by a factor of ∼2 and more than the choice for the solar minimum spectra in Subsection 6.2.2. The slab correlation length is again give by Equation 6.5 with the parametric values given in Table 6.4.

Figure 6.8 shows the long-term magnetic field and computed total variance, using different scales for the two quantities. By construction the variance has the same solar-cycle dependence as the magnetic field. The variance has a minimum value of $\sim 7.5\,\mathrm{nT}^2$ in 2010 and a maximum value of $\sim 39\,\mathrm{nT}^2$ in 1992.

The long-term slab- and 2D correlation scales, and the ultrascale, are shown with the magnetic field in Figure 6.9. Note the difference in scale for these quantities in this figure. Here the maximum values occur in 2010 and the minimum values in 1992, by assumption in anti-correlation with the magnetic field and therefore with the total variance.

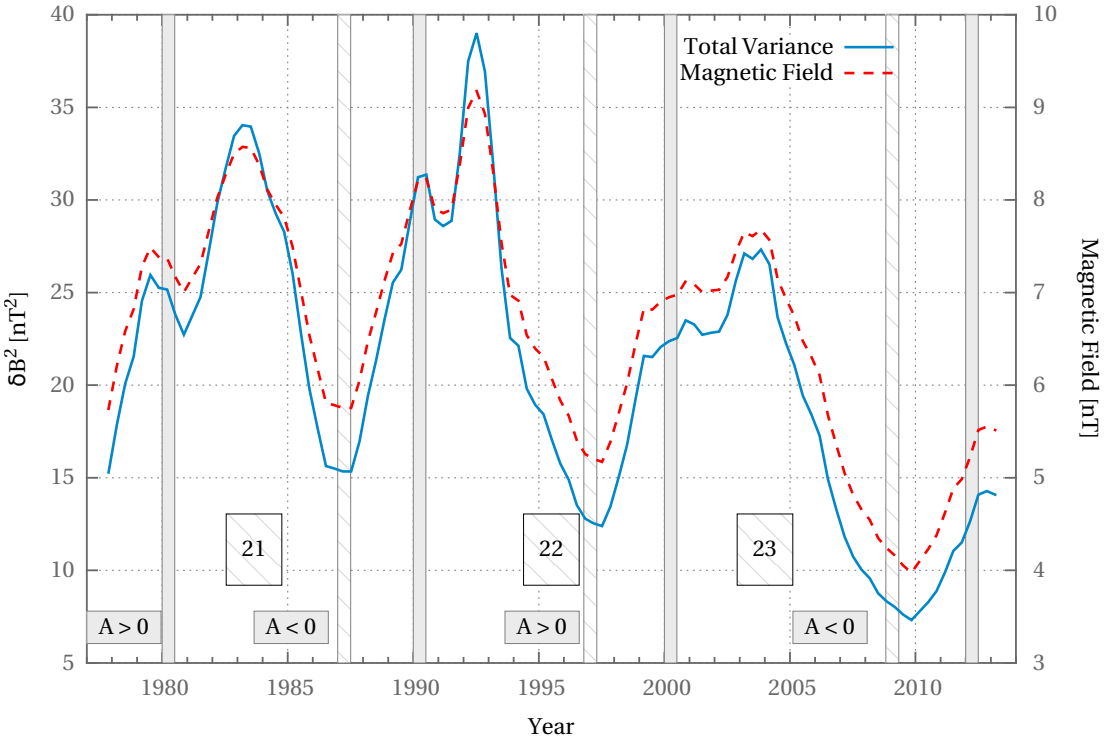

Figure 6.8: *Long-term behaviour of the variance compared with that of the magnetic field. Note the difference in scale for these quantities.*

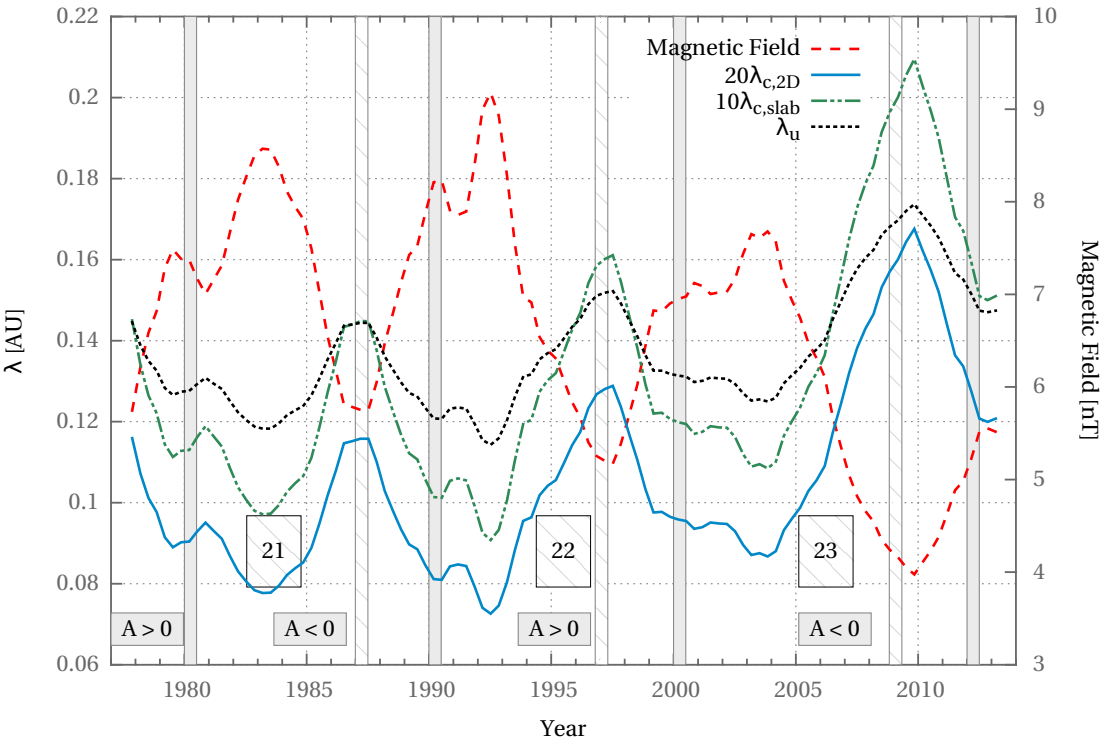

Figure 6.9: *Same as Figure 6.8 but for the slab and 2D correlation scales, as well as the ultrascale.*

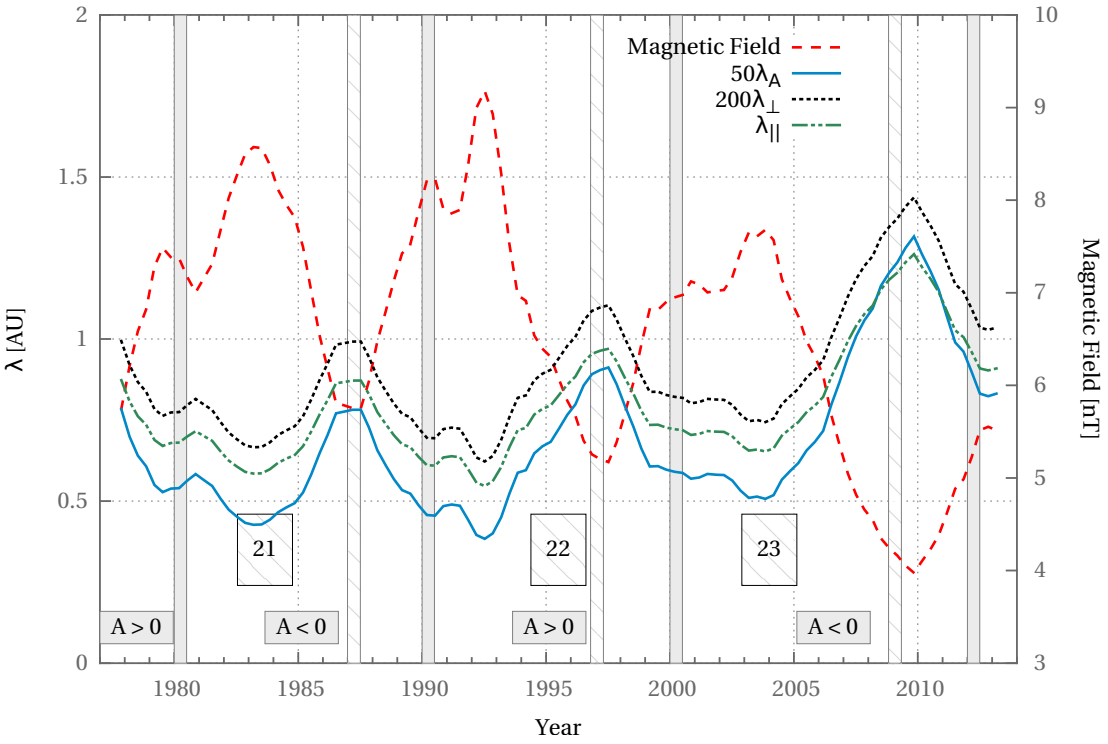

Figure 6.10: *Same as Figure 6.8 but for the the mean free paths and drift scale.*

Figure 6.10 shows the long-term parallel- and perpendicular mean free paths and drift scale with the magnetic field (once again on different scales). Again the maximum values occur in 2010 and the minimum values in 1992, in anti-correlation with the magnetic field and the total variance. This is in agreement with very recent and unpublished results by Nel [2015, private communication].

Figures 6.11a and 6.11b compare the modelled 1 GV and 7 GV intensities with the Sanae (0.8 GV cutoff rigidity) and the Potchefstroom (7.2 GV cutoff rigidity) neutron monitor intensities, respectively. Note that the scale is different for the observational data and the model. The former is expressed as a percentage of the March 1987 neutron monitor count rate while the latter is normalized with respect to the local interstellar value at the rigidity in question. Given that we are more interested in the qualitative than the quantitative behaviour of our fit in terms of the scope of the current project, this difference is not important since it does not affect our conclusions. Looking at both panels, the current model (solid line) does not show at either 1 GV or 7 GV the flat $A > 0$ versus the sharp $A < 0$ peaks characteristic of standard steady-state models [see, e.g., *Kóta and Jokipii*, 1983]. Note however that the model peaks are not symmetric with respect to solar minimum values; the increase toward solar minimum is typically somewhat more gradual than the decrease in intensity afterwards, in qualitative agreement with observations. The 1997 $A > 0$ peak is, however, significantly wider than the 1987

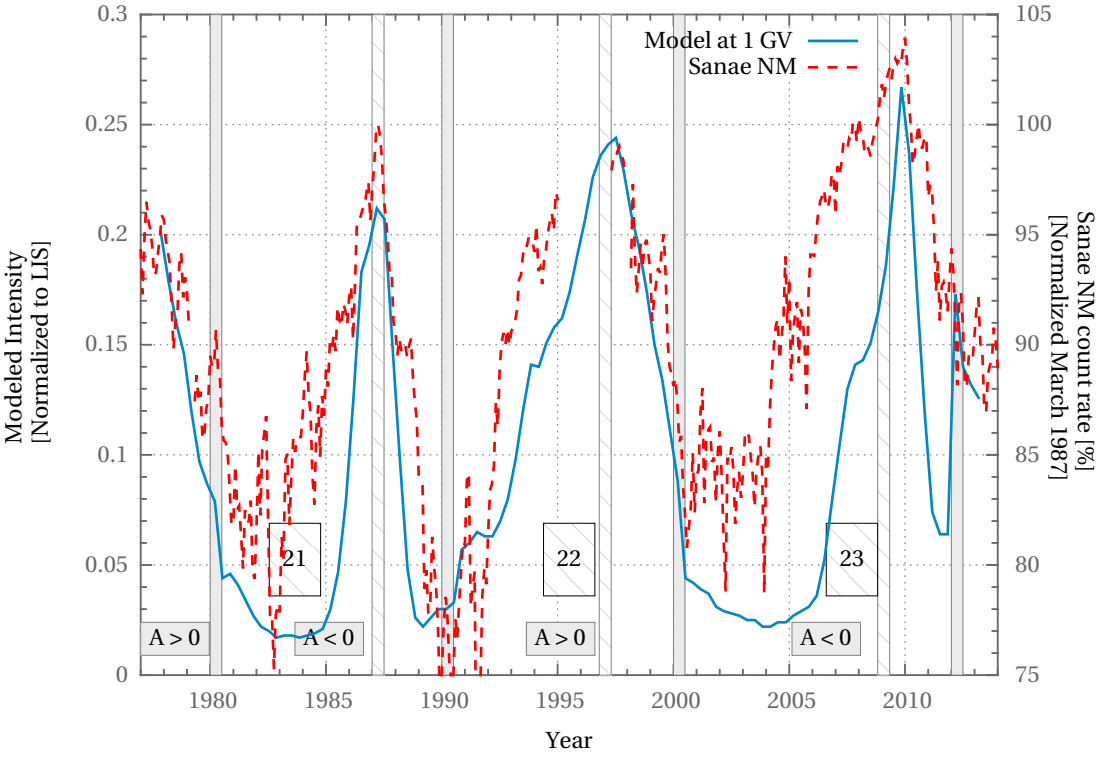

(a) *Comparison of the modelled 1 GV intensity to the Sanae 0.8 GV cutoff rigidity neutron monitor data.*

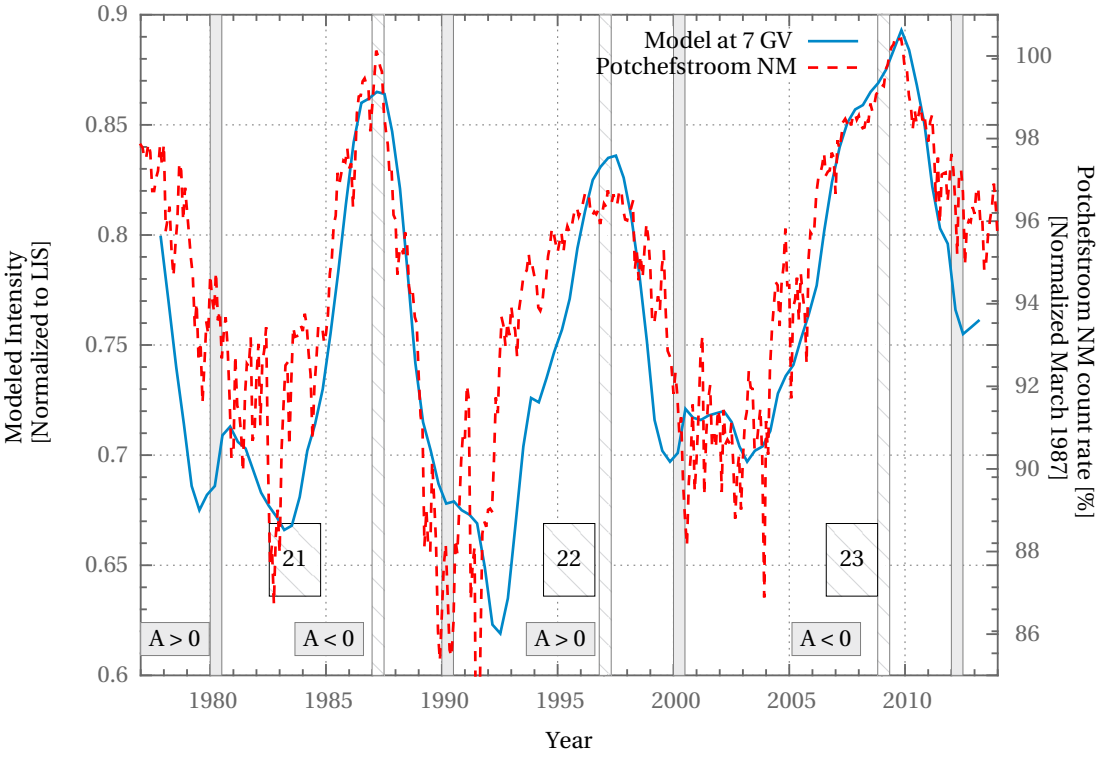

(b) *Comparison of the modelled 7 GV intensity to the Potchefstroom 7.2 GV cutoff rigidity neutron monitor data.*

Figure 6.11: *Modelled 1 GV and 7 GV intensities compared with neutron monitor data.*

$A < 0$ peak modelled at 1 GV. This difference is much less significant for the modelled intensities at 7 GV. Moreover, the $A < 0$ peak around 2009 is very different at the two rigidities. At 1 GV, the intensity shows a double peak around 2011 which is not present at 7 GV.

On average, the data show a decrease of the order of 10 % from solar minimum to solar maximum. At 1 GV, the model predicts a decrease of about a factor 10, whereas at 7 GV the decrease is much more reasonable at ∼30 %. The good agreement between our modelled parallel and perpendicular mean free paths with very recent and unpublished results of Nel [2015, preliminary results, private communication], lead us to conclude that the large changes in the modelled intensity from solar minimum to solar maximum are probably not directly caused by these two transport coefficients.

Another difference between the two rigidities is that the large transient decreases in 1982 and 1991 [see *Cane et al.*, 1996, for a comprehensive list of cosmic-ray decreases with their characteristics] seem to be present in the model at 7 GV, but not at 1 GV. Comparing the two panels, the width of the $A < 0$ peaks in 1987 and 2010 at 7 GV is in much better agreement with the data than the 1 GV peaks during the same periods. This may be because the drift coefficient at 7 GV is closer to the weak scattering value (see Figure 6.5) in the inner heliosphere, while at 1 GV it seems that the coefficient of *Burger and Visser* [2010] may be overestimating drift effects. Because particles reach Earth from the polar regions of the heliosphere during this magnetic polarity cycle, it may also be that our neglect of a latitude dependence for turbulence quantities and the subsequent effect of this on the diffusion tensor may be a contributing factor.

It is quite significant that the modelled intensities at both 1 GV and 7 GV are the highest during the so-called "unusual" solar minimum of 2009. Overall it does seem that the model is more realistic at 7 GV than 1 GV. Given uncertainties like the correct turbulence-reduced form of the drift coefficient [see *Engelbrecht and Burger*, 2015] perfect agreement between model and data in an *ab initio* approach such as the present one is not to be expected.

We now turn to the intensity-tilt loops shown in Figures 6.12 and 6.13 at 1 GV and 7 GV, respectively. Intensities are shown for both spot values and effective values of the tilt angle. The latter is shown for completeness: we will focus on the spot values so as to compare qualitatively with published data. As shown in Figures 5.4 to 5.6, these loops are observed to be wider during odd cycles than during even cycles when intensity is plotted as function of the local, spot value of the tilt angle. This is the case at 1 GV as shown in Figure 6.12 (solid line), but not at 7 GV. For the odd cycles 21 and 23, the sense of rotation is clockwise at 1 GV and 7 GV in agreement with observations. For the even cycle 22, the sense of rotation is again clockwise at 7 GV in agreement

with observations, but no dominant sense of rotation is present at 1 GV. It has been shown in Section 5.4 that the period over which the effective tilt is calculated changes the width of the loops and can also change their sense of rotation. Comparing the behaviour at the two rigidities therefore suggests that the period over which effective values are calculated may well be a function of rigidity. Both panels also show that the change in intensity as the tilt angle changes from its solar minimum value to about 30° is much more pronounced than what data show. This may again be an indication that drift effects are overestimated.

6.4 Effective Temporal Dependence Of Diffusion Tensor

In this chapter we followed a simplified *ab initio* approach, as explained in Chapter 1. We did not modify the chosen transport coefficients in an effort to find better agreement with cosmic-ray data, neither did we disregard data and theoretical results when constructing the turbulence quantities that enter into the various transport coefficients. Choices made for the solar-cycle dependence of turbulence quantities were motivated in Section 6.3. We now show that these choices have an unexpected consequence.

One often finds reference to a B^{-1} dependence of diffusion coefficients in the literature [see, e.g., *Kóta and Jokipii*, 1983; *Scherer and Fichtner*, 2004]. This then implies that the mean free paths should scale as r. In Section 6.2 we have shown that neither the spatial dependence of the parallel mean free path nor that of the perpendicular mean free path satisfies this requirement. The drift scale only satisfies this requirement beyond 5 AU, when the weak-scattering limit is reached, then the scaling is indeed as B_o^{-1}. Here we follow *Burger et al.* [2013] to show that the *temporal* dependence of the mean free paths is inversely proportional to that of the magnetic field. We will also discuss the temporal dependence of the drift scale, which was not addressed by these authors.

First we consider the parallel mean free path given in Equation 4.22. The quantity R that appears in it, defined in Equation 4.20, is small for low-energy particles, and solution 9 in Table 4.1 applies. The quantity R scales as B_o^{-1}, and consequently solution 9 scales as $B_o^{5/3}$, assuming s has the Kolmogorov value of 5/3. Note however that the coefficient of the square brackets in Equation 4.22 is independent of magnetic field magnitude, and therefore

$$\lambda_{\parallel} \propto B_o^{5/3} \qquad \text{Low energies.} \tag{6.12}$$

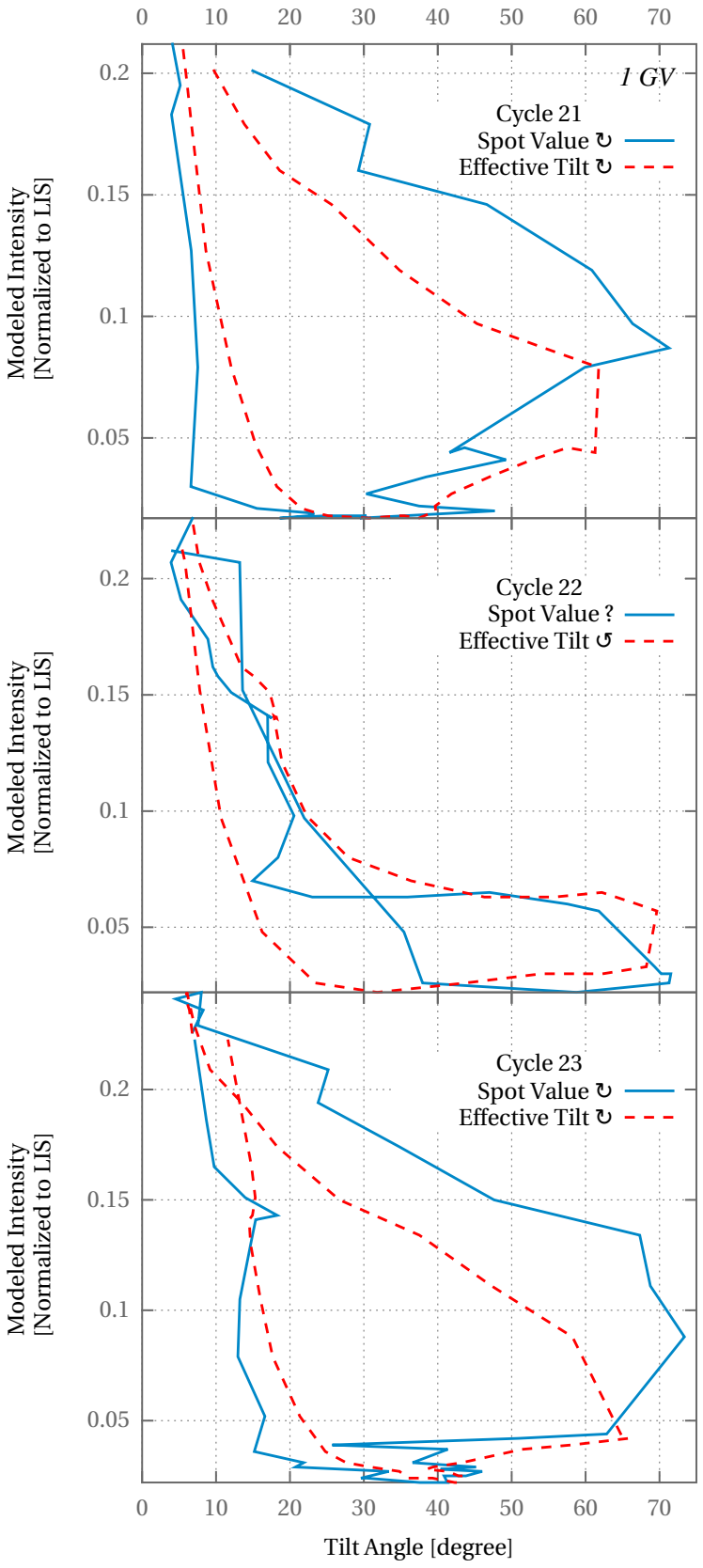

Figure 6.12: *Comparison of the behaviour of computed 1 GV intensity tilt loops for spot tilt angle values and for effective tilt angle values.*

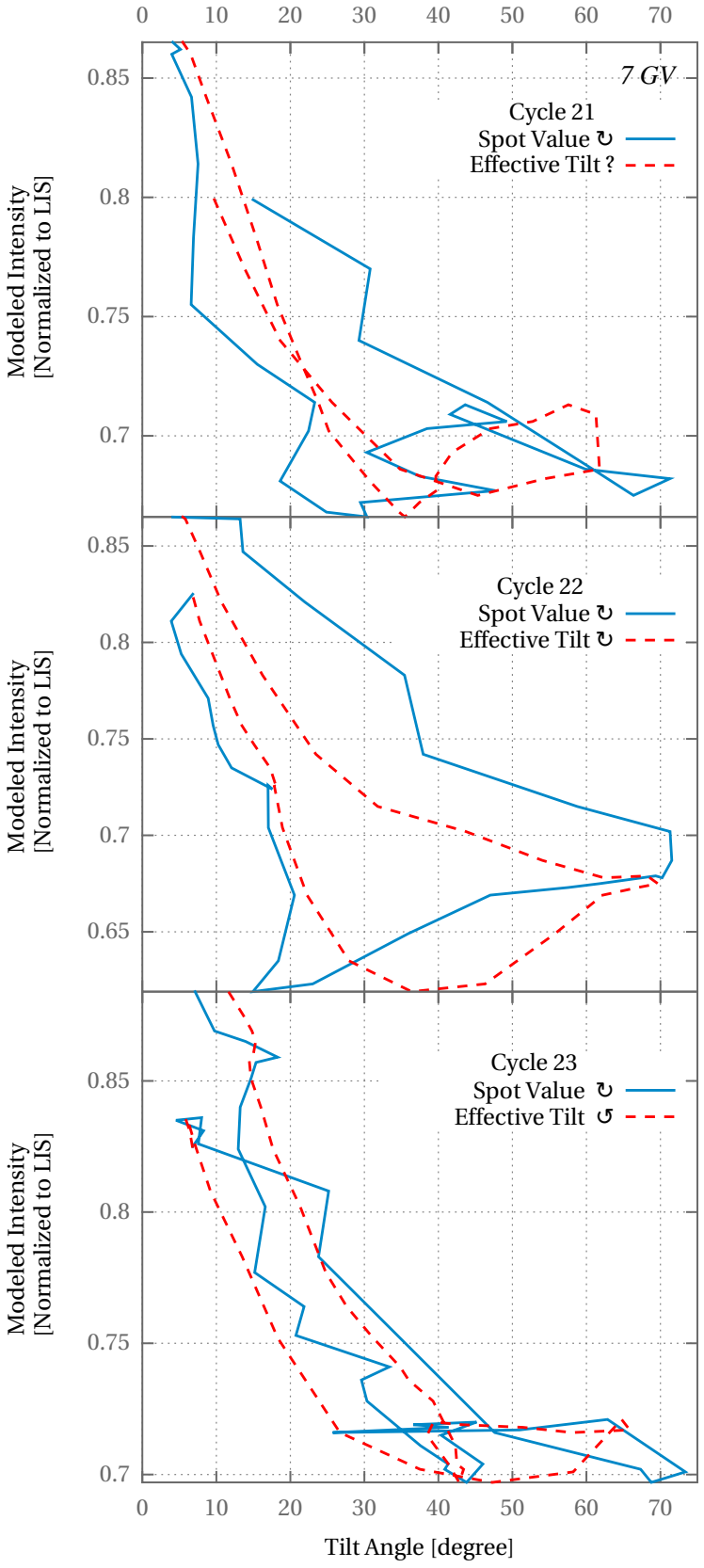

Figure 6.13: *Comparison of the behaviour of computed 7 GV intensity tilt loops for spot tilt angle values and for effective tilt angle values.*

For high energies, $R \gg 1$, solution 1 is appropriate, and is independent of magnetic field magnitude. Therefore

$$\lambda_{\parallel} \propto B_o^0 \qquad \text{High energies.} \tag{6.13}$$

Turning now to the perpendicular mean free path given in Equation 4.23, we readily see that $\lambda_{\perp} \propto B_o^{-4/3} \lambda_{\parallel}^{1/3}$ for a Kolmogorov $-5/3$ spectral index. Using Equations 6.12 and 6.13, we therefore have that

$$\lambda_{\perp} \propto B_o^{-7/9} \qquad \text{Low energies} \tag{6.14}$$

and

$$\lambda_{\perp} \propto B_o^{-4/3} \qquad \text{High energies.} \tag{6.15}$$

The above equations give the explicit dependence of the parallel- and perpendicular mean free paths on magnetic field magnitude, and neither shows a B_o^{-1} dependence. This was already established in Section 6.2, as is evident from Figure 6.7. However, to determine how the temporal dependence of $\lambda_{\parallel}$ and $\lambda_{\perp}$ compare with that of the magnetic field at Earth, we now substitute the temporal dependence of the relevant turbulence quantities at Earth, expressed in terms of the temporal dependence of the magnetic field as discussed in Section 6.3, into Equations 6.14 and 6.15 above.

By noting that k_{min} now has the same time dependence as B_o, we see that R is now independent of B_o. Therefore the temporal dependence of $\lambda_{\parallel}$ is the same at all energies because the term in square brackets in Equation 4.22 is now independent of B_o. Its coefficient scales as $R^2 \cdot B_o^2 \cdot k_{min}^{-1} \cdot \left(\delta B_o^2\right)^{-1}$ and consequently

$$\lambda_{\parallel} \propto B_o^{-1} \qquad \text{All energies.} \tag{6.16}$$

From Equation 4.23 we readily find that the temporal dependence of $\lambda_{\perp}$ is that of $\lambda_{c,2D}^{2/3} \cdot \lambda_{\parallel}^{1/3}$ and therefore the temporal dependence follows as

$$\lambda_{\perp} \propto B_o^{-1} \qquad \text{All energies.} \tag{6.17}$$

Finally we consider the drift scale, as given in Equation 4.25 for the weak scattering case ($\Omega\tau \gg 1$), and in Equation 4.26 for the case when drift is reduced by the effects of turbulence. For the weak scattering case, λ_A is inversely proportional to B_o, independent of turbulence quantities, and therefore has the same spatial and temporal dependence as B_o^{-1}. However, when reduction due to turbulence occurs, the situation changes drastically. In Equation 4.30 for $\Omega\tau$, the ratio $R_L/\lambda_{c,slab}$ is independent of B_o. The ratio $D_\perp/\lambda_{c,slab}$ is *not* independent of B_o because the ultrascale is proportional to the square root of the 2D correlation scale in this study. The quantity $D_\perp/\lambda_{c,slab}$ is raised to the power g, which depends on the ratio $R_L/\lambda_{c,slab}$ and is therefore not a function of B_o. It is, however, a function of particle rigidity. The net effect is that $\Omega\tau$ depends upon B_o in a rather complicated fashion, and moreover, the dependence changes as the particle rigidity changes.

In summary then, while $\lambda_\parallel$ and $\lambda_\perp$ display a rather straightforward temporal dependence, if turbulence plays a role, λ_A does not.

6.5 Summary And Conclusions

A three-dimensional cosmic-ray modulation code described by *Hattingh* [1998] is used to calculate cosmic-ray intensities at Earth. Following *Kóta and Jokipii* [1983], the explicit time dependence is eliminated by solving Parker's cosmic-ray transport equation in a system co-rotating with the Sun. The parallel- and perpendicular mean free paths and the drift scale discussed in Section 4.3 are used. Parametrized fits of turbulence quantities from *Engelbrecht* [2013] are used as input for these three transport coefficients. A spherical heliosphere with radius 100 AU, neglecting both the termination shock and the heliosheath, is assumed.

As one would expect, the unexpected high cosmic-ray intensities during the 2009 solar minimum have attracted a lot of attention [see, e.g., *Heber et al.*, 2009; *Moraal and Stoker*, 2010; *Potgieter et al.*, 2014; *Zhao et al.*, 2014; *Pacini and Usoskin*, 2015]. Although various possible reasons for the high intensities are discussed in these publications, the present study is the first one to follow an *ab initio* approach to study cosmic-ray energy spectra during three consecutive solar minima, including the 2009 one. Fairly accurate fits for the galactic cosmic-ray spectra for the 1987, 1997 and the 2009 solar minima are obtained. This approach yields intensities for the 2009 $A < 0$ solar minimum that are higher than the 1997 $A > 0$ solar minimum, as well as the previous $A < 0$ solar minimum in 1987. This is the first time that turbulence has been demonstrated as the most likely cause of the higher than usual cosmic-ray intensities during the 2009 solar minimum.

One should note that the turbulence quantities used in the present study follow from parametric fits to results from a turbulence transport model, and not the model itself; and that latitudinal effects are neglected. The model includes a larger effective tilt angle for 2009 than for the previous two solar minima; a smaller effective magnetic field magnitude and total variance, but larger effective slab- and 2D correlation scales, and a larger ultrascale. All of these combine to yield larger parallel and perpendicular mean free paths and also a larger drift scale in 2009, compared with those for the 1987 and 1997 solar minima.

To study long-term cosmic-ray modulation following an *ab initio* approach requires information about the solar-cycle dependence of turbulence quantities, in the present study for a period of close to 40 years. Since not all of this information was available, it was assumed that the variance is proportional to the square of the magnetic field magnitude, and that the slab- and the 2D correlation scales are inversely proportional to it. When comparing model results at 1 GV and 7 GV with observed intensities as function of time, better agreement is seen at 7 GV than at 1 GV, and at 7 GV better agreement for $A < 0$ cycles than for $A > 0$ cycles. For intensity-tilt loops, better (but far from perfect) agreement with shape, size and sense of rotation, evident from observations, is seen for 1 GV intensities than for 7 GV intensities. Based on these results for long-term modulation, it is concluded that the effect of turbulence on drift is not described accurately enough, and that the periods over which effective values are calculated for the tilt angle and other quantities are probably not independent of particle rigidity.

The chapter is concluded by showing that due to the assumed scaling of the total variance and correlation scales at Earth with magnetic field magnitude, the temporal dependence of the parallel and of the perpendicular mean free path is the same as that of B_o^{-1}. It is emphasized that this temporal dependence does not imply a similar spatial dependence.

CHAPTER 7

Summary And Conclusions

Background for this study is given in Chapter 2. An expression for cosmic-ray drift in a heliosphere that includes a wavy current sheet was derived in Chapter 3. In Chapter 4, turbulence properties were introduced and a composite slab/2D structure described. The dissipation range for turbulence spectra and effects related to it were ignored, since this study is focused on relatively high energy protons. This assumption lead to a natural selection of the appropriate piece-wise continues functions for the parallel mean free path derived by *Teufel and Schlickeiser* [2003]. An analytical approximation from the Nonlinear Guiding Center Theory (NLGC) of *Matthaeus et al.* [2003] derived by *Shalchi et al.* [2004a] was used for the perpendicular mean free path. Due to the lack of information on the form of the drift coefficient when turbulence is taken into account, the parameterized construction by *Burger and Visser* [2010] was used.

In Chapter 5 a simple idealized drift model was used to study the cosmic-ray intensity dependence on tilt angle. Contrary to the idealized steady-state drift model, intensity-tilt loops for observational data from the Climax neutron monitor [*Smith*, 2006] and the >70 MeV *IMP 8* protons [*Lockwood and Webber*, 2005] have the same sense of rotation and different loop sizes for the positive to negative magnetic polarity change as opposed to the negative to positive change. An effective tilt angle was introduced to emulate time dependence as it associates the intensities measured at a certain time with the average of at least the preceding year's worth of tilt angles. Intensity-tilt loops for neutron monitors, using the effective tilt angle, were found to become narrower for the odd cycles 21 and 23 but become wider for the even cycle 22, with the sense of rotation

for cycles 21 and 23 being clockwise and that for the cycle 22 becoming anti-clockwise, in agreement with the simple idealized drift model.

A three-dimensional cosmic-ray modulation model was used in Chapter 6 to calculate cosmic-ray intensities at Earth. Parametric fits of turbulence quantities from *Engelbrecht* [2013] were used as input for the parallel- and perpendicular mean free paths, and the drift coefficients. Fairly accurate fits for the galactic cosmic-ray spectra for the 1987, 1997 and the 2009 solar minima were obtained. This approach yields intensities for the 2009 $A < 0$ solar minimum that are higher than the 1997 $A > 0$ solar minimum, as well as the previous $A < 0$ solar minimum in 1987. To study long-term cosmic-ray modulation, it was assumed that the variance is proportional to the square of the magnetic field magnitude, and that the slab- and the 2D correlation scales were inversely proportional to it. Comparing model results at 1 GV and 7 GV with observed neutron monitor intensities as function of time, better agreement is seen at 7 GV than at 1 GV. In contrast, better agreement is seen at 1 GV than at 7GV when intensity-tilt loops are considered. This is the first time that turbulence has been demonstrated as the most likely cause of the higher than usual cosmic-ray intensities during the 2009 solar minimum.

To decide how successful the novel approach to long-term modulation introduced in this dissertation is, and whether it would be useful to refine it, one should consider the following:

- Does the present model improve our understanding of long-term cosmic-ray modulation? Perhaps the most significant improvement in our understanding of long-term modulation, is that when an effective tilt angle is used to plot intensity-tilt loops, differences between even and odd solar activity cycles seem to disappear. Features of these loops can then be readily explained using our current understanding of drift patterns in alternating solar magnetic polarity cycles.

- Is the present model a viable alternative to fully time-dependent models? The answer seems to be a guarded yes. Such models would automatically include the effects of propagating features like tilt angles on cosmic-ray modulation, and therefore the concept of effective values would not be needed. However, without a better understand of the drift coefficient, these models would suffer from the same limitation as the present model in this regard.

- Is the present approach a useful one? Firstly, the fact that parametric expressions are provided for the spatial dependences of magnetic variances, correlation scales and the 2D ultrascale, gives a reasonable alternative to solving the complex transport model for composite turbulence. Secondly, the way in which the temporal

dependence of turbulence quantities at Earth is modelled is also of relevance to fully time-dependent models, given the current lack of long-term turbulence data. The answer therefore is a less guarded yes.

There is currently no other simplified or fully *ab initio* model with which the current model can be compared. It will therefore serve as a benchmark for future projects, and several refinements can be made:

- Use a rigidity-dependent window when calculating effective values.
- Use more recent turbulence data when constructing the solar-cycle dependence of variances and correlation scales.
- Use more realistic turbulence spectra with wavenumber dependences that better reflect the behaviour in the energy range near Earth.
- Use the above spectra as input for the diffusion tensor.
- Use a more realistic form for the turbulence-reduced drift coefficient, if and when it becomes available.

Acknowledgements

I would like to thank:

- Prof. R. A. Burger, my supervisor, for the expert guidance, motivation, and the support throughout this entire study.
- Dr. N. E. Engelbrecht, for all the physics advice.
- Mary Voster, for checking my language and grammar.
- Mrs Petro Sieberhagen (Mama Petro) for handling all my financial inquiries most efficiently.
- My family and friends, for all the support.
- The South Africa National Space Agency, National Research Foundation and the Centre for Space Research of the NWU Potchefstroom Campus for financial support.

Katlego Daniel Moloto
Centre for Space Physics, North-West University,
Potchefstroom Campus,
2520, South Africa

APPENDIX A

Phase Shift In Moving Averages

All moving averages operate on a time series of measurements $\{A_i\}_{i=1}^{N}$, where N is the total number of measurements made and A_N is the most recent measurement. An n-point moving average is a new sequence $\{B_i\}_{i=1}^{N-n+1}$ defined from the A_i by taking the arithmetic mean of subsets of n terms. The n-point moving moving average for the k^{th} member can be expressed as

$$B_k = \frac{1}{n} \sum_{i=j}^{n+j-1} A_i, \qquad 1 \leq j \leq N - n + 1 \tag{A.1}$$

The k^{th} member can be defined in different ways, the central moving average and the endpoint moving average (as used to calculate effective values in this study). In the first case the central moving average is computed by using data equally spaced on either side of the point in the series where the mean is calculated, such that $k = j + \frac{(n-2)}{2}$ and

$$B_{j+\frac{(n-2)}{2}} = \frac{1}{n} \sum_{i=j}^{n+j-1} A_i. \tag{A.2}$$

As an example, if we have ten points, A_1 through A_{10}, and we wish to compute a five point moving average, the moving averages for successive points are

$$\begin{aligned} B_3 &= \frac{1}{5}\left(A_1 + A_2 + A_3 + A_4 + A_5\right) \\ B_4 &= \frac{1}{5}\left(A_2 + A_3 + A_4 + A_5 + A_6\right) \\ &\vdots \\ B_8 &= \frac{1}{5}\left(A_6 + A_7 + A_8 + A_9 + A_{10}\right). \end{aligned} \tag{A.3}$$

Another moving to average consider is what we use in the current study to calculate effective values, which is computed by using the n past data points such that $k = n+j-1$ and

$$B_{n+j-1} = \frac{1}{n}\sum_{i=j}^{n+j-1} A_i. \tag{A.4}$$

In this case the moving averages for the example above are

$$\begin{aligned} B_5 &= \frac{1}{5}\left(A_1 + A_2 + A_3 + A_4 + A_5\right) \\ B_6 &= \frac{1}{5}\left(A_2 + A_3 + A_4 + A_5 + A_6\right) \\ &\vdots \\ B_{10} &= \frac{1}{5}\left(A_6 + A_7 + A_8 + A_9 + A_{10}\right). \end{aligned} \tag{A.5}$$

Note that while the six averages in (A.5) are the same as those in (A.3), the positions of the B_k relative to the original data are different, and therefore a phase difference is introduced, given by $i - \left[i - \left(\frac{n-1}{2}\right)\right] = \frac{n-1}{2}$. If n is sufficiently large, the phase shift is one half of the window used to calculate the moving averages. This is well known, and is even referred to in Wikipedia (http://en.wikipedia.org/wiki/Moving_average). In the present study, this phase difference is what emulates time-dependent characteristics into a steady-state model.

Bibliography

Abramowitz, M., and I. A. Stegun, *Handbook of Mathematical Functions*, 1972.

Adriani, O., et al., Time dependence of the proton flux measured by pamela during the 2006 july-2009 december solar minimum, *Astrophys. J.*, *765*(2), 91, 2013.

Aharonian, F., A. Bykov, E. Parizot, V. S. Ptuskin, and A. Watson, Cosmic rays in galactic and extragalactic magnetic fields, *Space Sci. Rev.*, *166*, 97–132, 2012.

Ahluwalia, H. S., and C. Lopate, Response of IMP 8 penetrating proton channel to galactic cosmic ray modulation, in *Proceedings of the 30-th International Cosmic Ray Conference (Mexico City)*, vol. 1, pp. 331–334, 2007.

Alania, M. V., Stochastic Variations of Galactic Cosmic Rays, *Acta Physica Polonica B*, *33*, 1149–1166, 2002.

Alania, M. V., and T. V. Dzhapiashvili, The expected features of cosmic ray anisotropy due to Hall-type diffusion and the comparison with experiment, in *Proc. Int. Conf. Cosmic Ray 16th,* Kyoto, Japan, vol. 3, pp. 19–24, 1979.

Axford, W. I., The acceleration of galactic cosmic rays, in *Origin of Cosmic Rays*, *IAU Sumposium*, vol. 94, edited by G. Setti, G. Spada, and A. W. Wolfendale, pp. 339–358, 1981.

Balogh, A., E. J. Smith, B. T. Tsurutani, D. J. Southwood, R. J. Forsyth, and T. S. Horbury, The heliospheric magnetic field over the south polar region of the Sun, *Science*, *268*, 1007–1010, 1995.

Balogh, A., L. J. Lanzerotti, and S. T. Suess, *The heliosphere through the solar activity cycle*, Springer-Praxis Books and Springer Science+Business Media, 2008.

Baranov, V. B., and Y. G. Malama, Model of the solar wind interaction with the local interstellar medium - Numerical solution of self-consistent problem, *J. Geophys. Res.*, *98*, 15,157, doi:10.1029/93JA01171, 1993.

Barnden, L. R., and M. Bercovitch, Field Gradient and Curvature Drifts and Cosmic Ray Transport into the Solar System, in *International Cosmic Ray Conference*, *International Cosmic Ray Conference*, vol. 3, pp. 875–+, 1975.

Bieber, J. W., and W. H. Matthaeus, Perpendicular diffusion and drift at intermediate cosmic-ray energies, *Astrophys. J.*, *485*(2), 655–659, 1997.

Bieber, J. W., J. Chen, W. H. Matthaeus, C. W. Smith, and M. A. Pomerantz, Long-term variations of interplanetary magnetic field spectra with implications for cosmic ray modulation, *J. Geophys. Res.*, *98*(A3), 3585–3603, 1993.

Bieber, J. W., W. H. Matthaeus, C. W. Smith, W. Wanner, M.-B. Kallenrode, and G. Wibberenz, Proton and electron mean free paths: The Palmer consensus revisited, *Astrophys. J.*, *420*(1), 294–306, 1994.

Bieber, J. W., W. Wanner, and W. H. Matthaeus, Dominant two-dimensional solar wind turbulence with implications for cosmic ray transport, *J. Geophys. Res.*, *101*(A2), 2511–2522, 1996.

Bieber, J. W., W. H. Matthaeus, A. Shalchi, and G. Qin, Nonlinear guiding center theory of perpendicular diffusion: General properties and comparison with observation, *Geophys. Res. Lett.*, *31*, 10,805–+, doi:10.1029/2004GL020007, 2004.

Brun, A. S., S. Turck-Chieze, and P. Morel, Standard solar models in the light of new helioseismic constraints. I. The solar core, *Astrophys. J.*, *506*, 913–925, 1998.

Brun, A. S., S. Turck-Chieze, and J. P. Zahn, Standard solar models in the light of new helioseismic constraints. II. Mixing below the convective zone, *Astrophys. J.*, *525*, 1032–1041, 1999.

Burger, R. A., On the Theory and Application of Drift Motion of Charged Particles in Inhomogeneous Magnetic Fields, Ph.D. thesis, Potchefstroomse Universiteit vir Christelike Hoër Onderwys, R.S.A., 1987.

Burger, R. A., Cosmic-ray modulation and the heliospheric magnetic field, *Adv. Space Res.*, *35*(1), 636–642, 2005.

Burger, R. A., Modeling Drift along the Heliospheric Wavy Neutral Sheet, *Astrophys. J.*, *760*, 60, 2012.

Burger, R. A., and M. Hattingh, Steady-state drift-dominated modulation models for galactic cosmic rays, *Astrophys. Space Sci.*, *230*, 375–382, 1995.

Burger, R. A., and M. Hitge, The effect of a Fisk-type heliospheric magnetic field on cosmic ray modulation, in *Eos Trans. AGU, 83*(47), Fall Meet. Suppl., Abstract SH71A-04, 2002.

Burger, R. A., and M. Hitge, The effect of a Fisk-type heliospheric magnetic field on cosmic-ray modulation, *Astrophys. J. Lett.*, *617*(1), L73–L76, 2004.

Burger, R. A., and D. J. Visser, Reduction of Drift Effects due to Solar Wind Turbulence, *Astrophys. J.*, *725*, 1366–1372, 2010.

Burger, R. A., H. Moraal, and G. M. Webb, Drift theory of charged particles in electric and magnetic fields, *Astrophys. Space Sci.*, *116*, 107–129, 1985.

Burger, R. A., M. S. Potgieter, and B. Heber, Rigidity dependence of cosmic ray proton latitudinal gradients measured by the Ulysses spacecraft: Implications for the diffusion tensor, *J. Geophys. Res.*, *105*(A12), 27,447–27,455, 2000.

Burger, R. A., Y. van Niekerk, and M. S. Potgieter, An estimate of drift effects in various models of the heliospheric magnetic field, *Space Sci. Rev.*, *97*(1-4), 331–335, 2001.

Burger, R. A., T. P. J. Krüger, M. Hitge, and N. E. Engelbrecht, A Fisk-Parker Hybrid Heliospheric Magnetic Field With a Solar-Cycle Dependence, *Astrophys. J.*, *674*, 511–519, doi:10.1086/525039, 2008.

Burger, R. A., N. E. Engelbrecht, K. D. Moloto, and A. Nel, A comparison of cosmic-ray modulation during the 1986- and 2009 solar minima, in *Eos Trans. AGU, Fall Meet. Suppl., Abstract SH31C-07*, 2013.

Burlaga, L. F., V. Florinski, and N. F. Ness, In Situ Observations of Magnetic Turbulence in the Local Interstellar Medium, *804*, L31, doi:10.1088/2041-8205/804/2/L31, 2015.

Busching, I., and M. S. Potgieter, The variability of the proton cosmic ray flux on the Sun's way around the galactic center, *Adv. Space Res.*, *42*, 504–509, 2008.

Caballero-Lopez, R. A., and H. Moraal, The Numerical Description of Neutral Sheet Drift Effects, *International Cosmic Ray Conference*, *7*, 3871, 2003.

Caballero-Lopez, R. A., H. Moraal, and F. B. McDonald, Galactic cosmic ray modulation: Effects of the solar wind termination shock and the heliosheath, *Journal of Geophysical Research (Space Physics)*, *109*, A05,105, doi:10.1029/2003JA010358, 2004.

Candia, J., and E. Roulet, Diffusion and drift of cosmic rays in highly turbulent magnetic fields, *J. Cosmol. Astropart. Phys*, *10*, 007, 2004.

Cane, H. V., I. G. Richardson, and T. T. von Rosenvinge, Cosmic ray decreases: 1964-1994, *J. Geophys. Res.*, *101*, 21,561–21,572, doi:10.1029/96JA01964, 1996.

Cane, H. V., G. Wibberenz, I. G. Richardson, and T. T. von Rosenvinge, Cosmic ray modulation and the solar magnetic field, *Geophys. Res. Lett.*, *26*, 565–568, doi:10.1029/1999GL900032, 1999.

Castellani, V., S. D. Innocenti, G. Fiorentini, M. Lissia, and B. Ricci, Solar neutrinos: beyond standard solar models, *Physics Reports*, *281*, 309–398, 1997.

Choudhuri, A. R., *The physics of fluids and plasmas*, 342–350 pp., Cambridge University Press, Cambridge, 1998.

Cliver, E. W., History of research on solar energetic particle (SEP) events: the evolving paradigm, in *Universal heliophysical processes*, *Proceedings IAU Symposium*, vol. 257, edited by N. Gopalswamy and D. F. Webb, pp. 401–412, 2008.

Cliver, E. W., and A. G. Ling, 22 Year Patterns in the Relationship of Sunspot Number and Tilt Angle to Cosmic-Ray Intensity, *551*, L189–L192, doi:10.1086/320022, 2001.

Coleman, P. J., Jr., Turbulence, Viscosity, and Dissipation in the Solar-Wind Plasma, *Astrophys. J.*, *153*, 371, 1968.

Cranmer, S. R., Coronal holes, *Living Reviews in Solar Physics*, *6*, 3:1–66, 2009.

Davidson, P., *Turbulence: an introduction for scientists and engineers*, Oxford University Press, 2004.

Decker, R. B., S. M. Krimigis, E. C. Roelof, M. E. Hill, T. P. Armstrong, G. Gloeckler, D. C. Hamilton, and L. J. Lanzerotti, Voyager 1 in the foreshock, termination shock and heliosheath, *Science*, *309*, 2020–2024, 2005.

Dorman, L. (Ed.), *Cosmic Ray Interactions, Propagation, and Acceleration in Space Plasmas*, *Astrophysics and Space Science Library*, vol. 339, 2006.

Dunzlaff, P., A. Kopp, and B. Heber, Propagation of Jovian electron jets in heliospheric flux tube structures, *J. Geophys. Res.*, *115*(A10106), 1–11, 2010.

Effenberger, F., H. Fichtner, K. Scherer, S. Barra, J. Kleimann, and R. D. Strauss, A generalized diffusion tensor for fully anisotropic diffusion of energetic particles in the heliospheric magnetic field, *Astrophys. J.*, *750*, 108, 2012.

Engelbrecht, N. E., On the heliospheric diffusion tensor and its effect on 26-day recurrent cosmic ray variations., Master's thesis, North–West University (Potchefstroom Campus), South Africa, 2008.

Engelbrecht, N. E., On the development and applications of a three-dimensional ab initio cosmic-ray modulation model, Ph.D. thesis, North-West University (Potchefstroom campus), 2013.

Engelbrecht, N. E., and R. A. Burger, An Ab Initio Model for Cosmic-ray Modulation, *Astrophys. J.*, *772*, 46, doi:10.1088/0004-637X/772/1/46, 2013.

Engelbrecht, N. E., and R. A. Burger, A comparison of turbulence-reduced drift coefficients of importance for the modulation of galactic cosmic-ray protons in the supersonic solar wind, *Adv. Space Res.*, *55*, 390–400, doi:10.1016/j.asr.2014.09.019, 2015.

Ferreira, S. E. S., The heliospheric transport of galactic cosmic rays and Jovian electrons, Ph.D. thesis, Potchefstroom University for CHE, South Africa, 2002.

Ferreira, S. E. S., The transport of galactic and jovian cosmic ray electrons in the heliosphere, *Adv. Space Res.*, *35*, 586–596, 2005.

Ferreira, S. E. S., and M. S. Potgieter, Modulation over a 22-year cosmic ray cycle: On the tilt angles of the heliospheric current sheet, *Advances in Space Research*, *32*, 657–662, doi:10.1016/S0273-1177(03)00360-0, 2003.

Ferreira, S. E. S., M. S. Potgieter, R. A. Burger, B. Heber, and H. Fichtner, Modulation of Jovian and galactic electrons in the heliosphere: 1. Latitudinal transport of a few MeV electrons, *J. Geophys. Res.*, *106*, 24,979–24,987, 2001.

Fichtner, H., Anomalous cosmic rays: Messengers from the outer heliosphere, *Space Sci. Rev.*, *95*, 639–754, 2001.

Fisk, L. A., Motion of the footpoints of heliospheric magnetic field lines at the Sun: Implications for recurrent energetic particle events at high heliographic latitudes, *J. Geophys. Res.*, *101*, 15,547–15,553, 1996.

Fisk, L. A., On the global structure of the heliospheric magnetic field, *J. Geophys. Res.*, *106*(A8), 15,849–15,857, 2001.

Fisk, L. A., and G. Gloeckler, Acceleration of galactic cosmic rays in the interstellar medium, *Astrophys. J.*, *744*(127), 1–9, 2012.

Fisk, L. A., B. Kozlovsky, and R. Ramaty, An interpretation of the observed oxygen and nitrogen enhancements in low-energy cosmic rays, *Astrophys. J.*, *190*, L35–L37, 1974.

Fisk, L. A., T. H. Zurbuchen, and N. A. Schwadron, On the coronal magnetic field: Consequences of large-scale motions, *Astrophys. J.*, *521*, 868–877, 1999.

Fisk, L. A., et al., Global processes that determine cosmic ray modulation, in *Cosmic rays in the heliosphere*, pp. 179–214, Springer, 1998.

Florinski, V., Pickup ion acceleration at the termination shock and in the heliosheath, *Space Sci. Rev.*, *143*, 111–124, 2009.

Forbush, S. E., Three unusual cosmic-ray increases possibly due to charged particles from the Sun, *Physical Review Letters*, *70*, 771–772, 1946.

Forman, M. A., J. R. Jokipii, and A. J. Owens, Cosmic-ray streaming perpendicular to the mean magnetic field, *Astrophys. J.*, *192*(2), 535–540, 1974.

Fraternale, F., L. Gallana, M. Iovieno, M. Opher, J. D. Richardson, and D. Tordella, Turbulence in the solar wind: spectra from Voyager 2 data at 5 AU, *ArXiv e-prints*, 2015.

Fujiki, K., M. Kojima, M. Tokumaru, T. Ohmi, A. Yokobe, K. Hayashi, D. J. McComas, and H. A. Elliott, How did the solar wind structure change around the solar maximum? From interplanetary scintillation observation, *Ann. Geophys.*, *21*, 1257–1261, 2003.

Garaud, P., and C. Guervilly, The rotation rate of the solar radiative zone, *Astrophys. J.*, *695*, 799–808, 2009.

Giacalone, J., and J. R. Jokipii, The transport of cosmic rays across a turbulent magnetic field, *Astrophys. J.*, *520*(1), 204–214, 1999.

Giacalone, J., J. R. Jokipii, and J. Kóta, Particle drifts in a fluctuating magnetic field, in *Proc. Int. Conf. Cosmic Ray 26th,* Salt Lake City, U.S.A., vol. 7, pp. 37–40, 1999.

Gloeckler, G., L. A. Fisk, J. Geiss, M. E. Hill, D. C. Hamilton, R. B. Decker, and S. M. Krimigis, Composition of interstellar neutrals and the origin of anomalous cosmic rays, *Space Sci. Rev.*, *143*, 163–175, 2009.

Goldstein, M. L., D. A. Roberts, and W. H. Matthaeus, Magnetohydrodynamic Turbulence In The Solar Wind, *Ann. Rev. Astron. Astrophys.*, *33*, 283–326, doi: 10.1146/annurev.aa.33.090195.001435, 1995.

Gombosi, T. I., *Physics of the Space Environment*, 211–254 pp., Cambridge University Press, Cambridge, 1998.

Gosling, J. T., and V. J. Pizzo, Formation and Evolution of Corotating Interaction Regions and their Three Dimensional Structure, *Space Sci. Rev.*, *89*, 21–52, 1999.

Grechnev, V. V., et al., An extreme solar event of 20 January 2005: Properties of the flare and the origin of energetic particles, *Solar Physics*, *252*, 149–177, 2008.

Gurevitz, M., NASA's Voyager spacecraft: A fact sheet, in *CRS report for Congress*, Congressional Research Service - The Library of Congress, pp. 1–3, 2005.

Hale, G. E., On the probable existence of a magnetic field in sun-spots, *Astrophys. J.*, *28*, 315, 1908.

Hathaway, D. H., The solar cycle, *Living Reviews in Solar Physics*, *7*, 1–65, 2010.

Hattingh, M., The Modulation of Galactic Cosmic Rays in a Three-Dimensional Heliosphere, Ph.D. thesis, Potchefstroomse Universiteit vir Christelike Hoër Onderwys, R.S.A., 1998.

Hattingh, M., and R. A. Burger, A new simulated wavy neutral sheet drift model, *Adv. Space Res.*, *16*(9), 213–216, 1995.

Heber, B., Cosmic rays through the solar hale cycle, *Space Sci. Rev. Online*, pp. 1–14, 2011.

Heber, B., and M. S. Potgieter, Cosmic rays at high heliolatitudes, *Space Sci. Rev.*, *127*, 117–194, 2006.

Heber, B., and M. S. Potgieter, *Galactic and anomalous cosmic rays throught the solar cycle: New insights from Ulysses*, The heliosphere through the solar activity cycle, Springer-Praxis Books and Springer Science+Business Media, 2008.

Heber, B., A. Kopp, J. Gieseler, R. Müller-Mellin, H. Fichtner, K. Scherer, M. S. Potgieter, and S. E. S. Ferreira, Modulation of Galactic Cosmic Ray Protons and Electrons During an Unusual Solar Minimum, *Astrophys. J.*, *699*, 1956–1963, 2009.

Hoeksema, J. T., Extending the sun's magnetic field through the three-dimensional heliosphere, *Advances in Space Research*, *9*, 141–152, doi:10.1016/0273-1177(89)90432-8, 1989.

Hoeksema, J. T., Large-scale structure of the heliospheric magnetic field: 1976-1991, *in Solar Wind Seven Colloquium*, pp. 191–196, 1992.

Isenberg, P. A., and J. R. Jokipii, Gradient and curvature drifts in magnetic fields with arbitrary spatial variation, *Astrophys. J.*, *234*, 746–752, doi:10.1086/157551, 1979.

Jokipii, J. R., Cosmic-ray propagation. I. Charged particles in a random magnetic field, *Astrophys. J.*, *146*(2), 480–487, 1966.

Jokipii, J. R., Particle drifts for a finite scattering rate, in *International Cosmic Ray Conference*, 1993.

Jokipii, J. R., and E. N. Parker, On the convection, diffusion, and adiabatic deceleration of cosmic rays in the solar wind, *Astrophys. J.*, *160*, 735–744, 1970.

Jokipii, J. R., and B. T. Thomas, Effects of drift on the transport of cosmic rays IV. Modulation by a wavy interplanetary current sheet, *Astrophys. J.*, *243*, 1115–1122, 1981.

Jokipii, J. R., E. H. Levy, and W. B. Hubbard, Effects of particle drift on cosmic-ray transport. I. General properties, application to solar modulation, *Astrophys. J.*, *213(3)*, 861–868, 1977.

Jones, G. H., A. Balogh, and E. J. Smith, Solar magnetic field reversal as seen at Ulysses, *Geophys. Res. Lett.*, *30*(19), 8028, doi:10.1029/2003GL017204, 2003.

Kallenrode, M. B., *Space physics: an introduction to plasmas and particles in the heliosphere and magnetospheres*, Springer, 2001.

Kobylinski, Z., Comparison of the Fisk magnetic field with the standard Parker IMF: Consequences for diffusion coefficients, *Adv. Space Res.*, *27*(3), 541–546, 2001.

Kolmogorov, A., The Local Structure of Turbulence in Incompressible Viscous Fluid for Very Large Reynolds' Numbers, *Akademiia Nauk SSSR Doklady*, *30*, 301–305, 1941.

Koskinen, H. E., *Physics of space storms: From the solar surface to the Earth*, Springer-Praxis Books in Environmental Sciences, 2011.

Kóta, J., Drift - the Essential Process in Losing Energy, in *International Cosmic Ray Conference*, *International Cosmic Ray Conference*, vol. 3, pp. 13–+, 1979.

Kóta, J., and J. R. Jokipii, Effects of drift on the transport of cosmic rays. VI - A three-dimensional model including diffusion, *Astrophys. J.*, *265*, 573–581, doi:10.1086/160701, 1983.

Kóta, J., and J. R. Jokipii, 3-D simulation of heliospheric transport: a comparison of models, in *Proc. Int. Conf. Cosmic Ray 24th,* Durban, South Africa, vol. 2, pp. 25–28, 1997.

Kóta, J., and J. R. Jokipii, Cosmic-ray modulation and the structure of the heliospheric magnetic field, in *Proc. Int. Conf. Cosmic Ray 26th,* Salt Lake City, U.S.A., vol. 7, pp. 9–12, 1999.

Kóta, J., and J. R. Jokipii, Recurrent depressions of galactic cosmic rays in CIRs: 22-year cycle, in *Proceedings of the 27-th International Cosmic Ray Conference (Hamburg)*, vol. 9, pp. 3577–3580, 2001.

Kóta, J., and J. R. Jokipii, Modulation of cosmic rays in heliomagnetic fields with organized meridional components, in *Eos Trans. AGU, 82*(47), Fall Meet. Suppl., Abstract SH22A-51, 2001.

Krimigis, S. M., D. G. Mitchell, E. C. Roelof, K. C. Hsieh, and D. J. McComas, Imaging the Interaction of the Heliosphere with the Interstellar Medium from Saturn with Cassini, *Science*, *326*, 971–, doi:10.1126/science.1181079, 2009.

Krüger, H., A calibration neutron monitor for long-term cosmic ray modulation stuidies, Ph.D. thesis, North-West University (Potchefstroom Campus), 2006.

Krüger, T. P. J., The effect of a Fisk-Parker hybrid magnetic field on cosmic rays in the heliosphere, Master's thesis, North-West University (Potchefstroom Campus), 2005.

Langner, U. W., Effects of termination shock acceleration on cosmic rays in the heliosphere, Ph.D. thesis, Potchefstroom University for CHE, South Africa, 2004.

Le Roux, J. A., and M. S. Potgieter, A time-dependent drift model for the long-term modulation of cosmic rays with special reference to asymmetries with respect to the solar minimum of 1987, *Astrophys. J.*, *361*, 275–282, 1990.

Le Roux, J. A., and M. S. Potgieter, The simulated features of heliospheric cosmic-ray modulation with a time-dependent drift model. II - On the energy dependence of the onset of new modulation in 1987, *Astrophys. J.*, *390*, 661–667, doi:10.1086/171317, 1992.

Leamon, R. J., W. H. Matthaeus, C. W. Smith, G. P. Zank, D. J. Mullan, and S. Oughton, MHD-driven Kinetic Dissipation in the Solar Wind and Corona, *Astrophys. J.*, *537*, 1054–1062, doi:10.1086/309059, 2000.

Lockwood, J. A., and W. R. Webber, On the interplanetary cosmic ray latitudinal gradient, *J. Geophys. Res.*, *97*(A6), 8221–8230, 1992.

Lockwood, J. A., and W. R. Webber, Intensities of galactic cosmic rays of ˜1.5 GV rigidity at Earth versus the heliospheric current sheet tilt, *J. Geophys. Res.*, *110*, A04,102, doi:10.1029/2004JA010880, 2005.

Lockwood, J. A., W. R. Webber, and J. T. Hoeksema, Interplanetary cosmic ray latitudinal gradient in 1984 to 1987 using IMP 8 and Voyager data, *J. Geophys. Res.*, *93*, 7521–7526, doi:10.1029/JA093iA07p07521, 1988.

Lockwood, J. A., W. R. Webber, and H. Debrunner, Differences in the maximum intensities and the intensity-time profiles of cosmic rays in alternate solar magnetic field polarities, *J. Geophys. Res.*, *106*, 10,635–10,644, doi:10.1029/2000JA000307, 2001.

Manuel, R., Time-dependent modulation of cosmic rays in the outer heliosphere, Ph.D. thesis, North-West University (Potchefstroom campus), 2013.

Matthaeus, W. H., M. L. Goldstein, and D. A. Roberts, Evidence for the presence of quasi-two-dimensional nearly incompressible fluctuations in the solar wind, *J. Geophys. Res.*, *95*, 20,673–20,683, 1990.

Matthaeus, W. H., P. C. Gray, D. H. Pontius Jr., and J. W. Bieber, Spatial structure and field-line diffusion in transverse magnetic turbulence, *Phys. Rev. Lett.*, *75*(11), 2136–2139, 1995.

Matthaeus, W. H., G. P. Zank, C. W. Smith, and S. Oughton, Turbulence, spatial transport, and heating of the solar wind, *Physical Review Letters*, *82*, 3444–3447, 1999.

Matthaeus, W. H., G. Qin, J. W. Bieber, and G. P. Zank, Nonlinear collisionless perpendicular diffusion of charged particles, *APJ*, *590*(1), L53–L56, 2003.

Matthaeus, W. H., J. W. Bieber, D. Ruffolo, P. Chuychai, and J. Minnie, Spectral Properties and Length Scales of Two-dimensional Magnetic Field Models, *Astrophys. J.*, *667*, 956–962, doi:10.1086/520924, 2007.

Maunder, E. W., Note on the distribution of sun-spots in heliographic latitude, 1874-1902, *Mon. Not. R. Astron. Soc.*, *64*, 747–761, 1904.

McComas, D. J., R. W. Ebert, H. A. Elliott, B. E. Goldstein, J. T. Gosling, N. A. Schwadron, and R. M. Skoug, Weaker solar wind from the polar coronal holes and the whole Sun, *Geophys. Res. Lett.*, *35*(L18103), 1–5, 2008.

McComas, D. J., M. A. Dayeh, H. O. Funsten, G. Livadiotis, and N. A. Schwadron, The Heliotail Revealed by the Interstellar Boundary Explorer, *Astrophys. J.*, *771*, 77, doi:10.1088/0004-637X/771/2/77, 2013.

McComas, D. J., et al., Solar wind observations over Ulysses' first full polar orbit, *J. Geophys. Res.*, *105*, 10,419–10,434, 2000.

McDonald, F. B., Integration of neutron monitor data with spacecraft observations: a historical perspective, *Space Sci. Rev.*, *93*, 263–284, 2000.

McDonald, F. B., H. Moraal, J. P. L. Reinecke, N. Lal, and R. E. McGuire, The cosmic radiation in the heliosphere at succesive solar minima, *J. Geophys. Res.*, *97*, 1557–1570, 1992.

Meyer-Vernet, N., *Basics of the Solar of the Wind*, Cambridge University Press, 2007.

Minnie, J., J. W. Bieber, W. H. Matthaeus, and R. A. Burger, On the ability of different diffusion theories to account for directly simulated diffusion coefficients, *Astrophys. J.*, *663*, 1049–1054, doi:10.1086/518765, 2007a.

Minnie, J., J. W. Bieber, W. H. Matthaeus, and R. A. Burger, Suppression of particle drifts by turbulence, *Astrophys. J.*, p. In press, 2007b.

Moraal, H., Cosmic-Ray Modulation Equations, *Space Sci. Rev.*, p. 291, 2011.

Moraal, H., and P. H. Stoker, Long-term neutron monitor observations and the 2009 cosmic ray maximum, *J. Geophys. Res.*, *115*(A12109), 1–9, 2010.

Nagashima, K., and L. Morishita, Twenty-two year modulation of cosmic rays associated with polarity reversal of polar magnetic field of the sun, *28*, 195–205, doi:10.1016/0032-0633(80)90095-1, 1980.

Ness, N. F., Heliospheric Magnetic Fields and Termination Shock Crossing: Voyager 1, *ISSI Scientific Reports Series*, *5*, 183–202, 2006.

Ness, N. F., and J. M. Wilcox, Sector structure of the quiet interplanetary magnetic field, *Science*, *148*(3677), 1592–1594, 1965.

Opher, M., J. F. Drake, B. Zieger, and T. I. Gombosi, Magnetized Jets Driven By the Sun: the Structure of the Heliosphere Revisited, *Astrophys. J.*, *800*, L28, doi:10.1088/2041-8205/800/2/L28, 2015.

Oughton, S., W. H. Matthaeus, C. W. Smith, B. Breech, and P. A. Isenberg, Transport of solar wind fluctuations: A two-component model, *J. Geophys. Res.*, *116*, 8105, 2011.

Pacini, A. A., and I. G. Usoskin, An Unusual Pattern of Cosmic-Ray Modulation During Solar Cycles 23 and 24, *290*, 943–950, doi:10.1007/s11207-014-0645-0, 2015.

Palmer, I. D., Transport coefficients of low-energy cosmic rays in interplanetary space, *Rev. Geophys. Space Phys.*, *20*(2), 335–351, 1982.

Parker, E. N., Dynamics of the interplanetary gas and magnetic fields, *Astrophys. J.*, *128*, 664–676, 1958a.

Parker, E. N., Cosmic-ray modulation by solar wind, *Physical Review*, *110*, 1445–1449, 1958b.

Parker, E. N., The Stellar-Wind Regions., *Astrophys. J.*, *134*, 20, doi:10.1086/147124, 1961.

Parker, E. N., The passage of energetic charged particles through interplanetary space, *Planet. Space Sci.*, *13*, 9–49, 1965.

Phillips, J. L., et al., Ulysses solar wind plasma observations from pole to pole, *Geophys. Res. Lett.*, *22*, 3301–3304, 1995.

Pontieu, B. D., S. W. McIntosh, V. H. Hansteen, and C. J. Schrijver, Observing the roots of solar coronal heating - in the chromosphere, *Astrophys. J.*, *701*, L1–L6, 2009.

Potgieter, M. S., The modulation of galactic cosmic rays as described by a three-dimensional drift model, Ph.D. thesis, Potchefstroom University for CHE, South Africa, 1984.

Potgieter, M. S., Solar cycle variations and cosmic rays, *J. Atmospheric and Solar-Terrestrial Physics*, *70*, 207–218, 2008.

Potgieter, M. S., The dynamic heliosphere, solar activity, and cosmic rays, *Adv. Space Res.*, *46*, 402–412, 2010.

Potgieter, M. S., and H. Moraal, A drift model for the modulation of galactic cosmic rays, *Astrophys. J.*, *294*, 425–440, 1985.

Potgieter, M. S., E. E. Vos, M. Boezio, N. De Simone, V. Di Felice, and V. Formato, Modulation of Galactic Protons in the Heliosphere During the Unusual Solar Minimum of 2006 to 2009, *289*, 391–406, doi:10.1007/s11207-013-0324-6, 2014.

Richardson, I. G., H. V. Cane, T. T. von Rosenvinge, and R. McGuire, IMP 8 GME energetic particle observations over three solar cycles, in *Proceedings of the 30-th International Cosmic Ray Conference (Mexico City)*, vol. 1, pp. 323–326, 2007.

Richardson, J. D., J. C. Kasper, C. Wang, J. W. Belcher, and A. J. Lazarus, Cool heliosheath plasma and deceleration of the upstream solar wind at the termination shock, *Nature*, *454*, 63–66, 2008.

Roberts, D. A., J. Giacalone, J. R. Jokipii, M. L. Goldstein, and T. D. Zepp, Spectra of polar heliospheric magnetic fields and implications for field structure, *J. Geophys. Res.*, *112*, 8103–+, doi:10.1029/2007JA012247, 2007.

Saito, T., and D. B. Swinson, The inclination of the heliospheric neutral sheet and cosmic ray intensity at the earth, *J. Geophys. Res.*, *91*, 4536–4542, doi:10.1029/JA091iA04p04536, 1986.

Scherer, K., and H. Fichtner, Constraints on the heliospheric magnetic field variation during the maunder minimum from cosmic ray modulation modelling, *413*, L11–L14, doi:10.1051/0004-6361:20034636, 2004.

Schlaepfer, H., Cosmic rays, *Spatium*, *11*, 1–15, 2003.

Schrijver, C. J., A. M. Title, K. L. Harvey, N. R. Sheeley, Y. M. Wang, G. H. J. van den Oord, R. A. D. Shine, T. Tarbell, and N. E. Hurlburt, Large-scale coronal heating by the small-scale magnetic field of the sun, *Nature*, *394*, 152, 1998.

Schwenn, R., Solar wind sources and their variations over the solar cycle, *Space Sci. Rev.*, *124*, 51–76, 2006.

Shalchi, A., J. W. Bieber, and W. H. Matthaeus, Analytic forms of the perpendicular diffusion coefficient in magnetostatic turbulence, *Astrophys. J.*, *604*, 675–686, doi: 10.1086/382128, 2004.

Shalchi, A., J. W. Bieber, and W. H. Matthaeus, Analytic forms of the perpendicular diffusion coefficient in magnetostatic turbulence, *Astrophys. J.*, *604*, 675–686, 2004a.

Shalchi, A., J. W. Bieber, W. H. Matthaeus, and G. Qin, Nonlinear parallel and perpendicular diffusion of charged cosmic rays in weak turbulence, *Astrophys. J.*, *616*, 617–629, 2004b.

Shaviv, N., and G. Shaviv, The state of ^{7}Be in the core of the Sun and the solar neutrino flux, *Mon. Not. R. Astron. Soc.*, *341*, 119–128, 2003.

Shikaze, Y., et al., Measurements of 0.2 20 GeV/n cosmic-ray proton and helium spectra from 1997 through 2002 with the BESS spectrometer, *Astroparticle Physics*, *28*, 154–167, 2007.

Simpson, J. A., The cosmic ray nucleonic component: the invention and scientific uses of the neutron monitor, *Space Sci. Rev.*, *93*, 11–32, 2000.

Smith, C. W., P. A. Isenberg, W. H. Matthaeus, and J. D. Richardson, Turbulent heating of the solar wind by newborn interstellar pickup protons, *Astrophys. J.*, *638*, 508–517, 2006.

Smith, E. J., The heliospheric current sheet and modulation of Galactic cosmic rays, *J. Geophys. Res.*, *95*, 18,731–18,743, doi:10.1029/JA095iA11p18731, 1990.

Smith, E. J., The sun, solar wind, and magnetic field. I, in *Course CXLII*, edited by A. Ferrari and E. Sindoni, in *Proc. Int. Sch. of Phys. "Enrico Fermi",* Amsterdam, The Netherlands, 2000.

Smith, E. J., The heliospheric current sheet, *J. Geophys. Res.*, *106*(A8), 15,819–15,831, 2001.

Smith, E. J., The Heliospheric Current Sheet and Galactic Cosmic Rays, in *Physics of the Inner Heliosheath*, *American Institute of Physics Conference Series*, vol. 858, edited by J. Heerikhuisen, V. Florinski, G. P. Zank, & N. V. Pogorelov , pp. 104–109, doi:10.1063/1.2359313, 2006.

Smith, E. J., Solar cycle evolution of the heliospheric magnetic field: The Ulysses legacy, *J. Atmospheric and Solar-Terrestrial Physics*, *73*, 277–289, 2011.

Smith, E. J., and B. T. Thomas, Latitudinal extent of the heliospheric current sheet and modulation of galactic cosmic rays, *J. Geophys. Res.*, *91*, 2933–2942, doi:10.1029/JA091iA03p02933, 1986.

Smith, W. S., W. H. Matthaeus, G. P. Zank, N. F. Ness, S. Oughton, and J. D. Richardson, Heating of the low-latitude solar wind by dissipation of turbulent magnetic fluctuations, *J. Geophys. Res.*, *106*(A5), 8253–8272, 2001.

Snodgrass, H. B., Magnetic rotation of the solar photosphere, *Astrophys. J.*, *270*(1), 288–299, 1983.

Spiegel, E. A., and J. P. Zahn, The solar tachocline, *Astron. Astrophys.*, *265*, 106–114, 1992.

Sternal, O., N. E. Engelbrecht, R. A. Burger, S. E. S. Ferreira, H. Fichtner, B. Heber, A. Kopp, M. S. Potgieter, and K. Scherer, Possible evidence for a Fisk-type heliospheric magnetic field. I. Analyzing Ulysses/KET electron observations, *Astrophys. J.*, *741*(23), 1–12, 2011.

Stix, M., *The Sun: An introduction*, Springer, 2004.

Stone, E. C., A. C. Cummings, F. B. McDonald, B. C. Heikkila, N. Lal, and W. R. Webber, Voyager 1 explores the termination shock region and the heliosheath beyond, *Science*, *309*, 2017–2020, 2005.

Stone, E. C., A. C. Cummings, F. B. McDonald, B. C. Heikkila, N. Lal, and W. R. Webber, An asymmetric solar wind termination shock, *Nature*, *454*, 71–74, 2008.

Stone, E. C., A. C. Cummings, F. B. McDonald, B. C. Heikkila, N. Lal, and W. R. Webber, Voyager 1 Observes Low-Energy Galactic Cosmic Rays in a Region Depleted of Heliospheric Ions, *Science*, *341*, 150–153, doi:10.1126/science.1236408, 2013.

Strauss, R. D., Modelling of anomalous cosmic rays, Master's thesis, North–West University (Potchefstroom Campus), South Africa, 2010.

Strauss, R. D., M. S. Potgieter, S. E. S. Ferreira, and M. E. Hill, Modelling anomalous cosmic ray oxygen in the heliosheath, *Astron. Astrophys.*, *522*(A35), 1–8, 2010.

Svalgaard, L., and J. M. Wilcox, The Spiral Interplanetary Magnetic Field: A Polarity and Sunspot Cycle Variation, *Science*, *186*, 51–53, doi:10.1126/science.186.4158.51, 1974.

Tautz, R. C., and A. Shalchi, Drift Coefficients of Charged Particles in Turbulent Magnetic Fields, *Astrophys. J.*, *744*, 125, 2012.

Teufel, A., and R. Schlickeiser, Analytic calculation of the parallel mean free path of heliospheric cosmic rays. I. Dynamical magnetic slab turbulence and random sweeping slab turbulence, *Astron. Astrophys.*, *393*, 703–715, doi:10.1051/0004-6361:20021046, 2002.

Teufel, A., and R. Schlickeiser, Analytic calculation of the parallel mean free path of heliospheric cosmic rays. II. Dynamical magnetic slab turbulence and random sweeping slab turbulence with finite wave power at small wavenumbers, *Astron. Astrophys.*, *397*, 15–25, 2003.

Thomas, B. T., and E. J. Smith, The Parker spiral configuration of the interplanetary magnetic field between 1 and 8.5 AU, *J. Geophys. Res.*, *85*(A12), 6861–6867, 1980.

Usoskin, I. G., A history of solar activity over millennia, *Living Reviews in Solar Physics*, *5*, 1–88, 2008.

Van Niekerk, Y., An Investigation into the Causes and Consequences of North-South Asymmetries in the Heliosphere, Master's thesis, Potchefstroomse Universiteit vir Christelike Hoër Onderwys, R.S.A., 2000.

Visser, D. J., The effect of turbulence-modified drift on the modulation of galactic cosmic rays in the heliosphere, Master's thesis, North-West University (Potchefstroom campus), 2009.

Wang, Y. M., Coronal holes and open magnetic flux, *Space Sci. Rev.*, *144*, 383–399, 2009.

Wang, Y. M., Semiempirical models of the slow and fast solar wind, *Space Sci. Rev.*, pp. 1–21, 2011.

Webber, W. R., and J. A. Lockwood, Characteristics of the 22-year modulation of cosmic rays as seen by neutron monitors, *J. Geophys. Res.*, *93*, 8735–8740, doi:10.1029/JA093iA08p08735, 1988.

Webber, W. R., and J. A. Lockwood, The onset of the new solar modulation cycle in 1987-1988 as a function of heliocentric radius and latitude, *J. Geophys. Res.*, *95*, 2253–2259, doi:10.1029/JA095iA03p02253, 1990.

Webber, W. R., and J. A. Lockwood, Intensity variations of > 70-MeV cosmic rays measured by Pioneer 10, Voyager 1 & 2 and IMP in the heliosphere during the recovery period from 1992-1995, *Geophys. Res. Lett.*, *22*, 2669–2672, 1995.

Webber, W. R., and J. A. Lockwood, Voyager and Pioneer spacecraft measurements of cosmic ray intensities in the outer heliosphere: Toward a new paradigm for understanding the global modulation process: 2. Maximum solar modulation (1990-1991), *J. Geophys. Res.*, *106*, 29,333–29,340, doi:10.1029/2001JA000119, 2001.

Webber, W. R., and F. B. McDonald, Recent Voyager 1 data indicate that on 25 August 2012 at a distance of 121.7 AU from the Sun, sudden and unprecedented intensity changes were observed in anomalous and galactic cosmic rays, *Geophys. Res. Lett.*, *40*, 1665–1668, doi:10.1002/grl.50383, 2013.

Weygand, J. M., W. H. Matthaeus, S. Dasso, M. G. Kivelson, L. M. Kistler, and C. Mouikis, Anisotropy of the Taylor scale and the correlation scale in plasma sheet and solar wind magnetic field fluctuations, *J. Geophys. Res.*, *114*, 7213, 2009.

Weygand, J. M., W. H. Matthaeus, D. S., and M. Kivelson, Correlation and Taylor scale variability in the interplanetary magnetic field fluctuations as a function of solar wind speed, *J. Geophys. Res.*, *116*, 2011.

Zank, G. P., W. H. Matthaeus, and C. W. Smith, Evolution of turbulent magnetic fluctuation power with heliospheric distance, *J. Geophys. Res.*, *101*(A8), 17,093–17,107, 1996.

Zhao, L.-L., G. Qin, M. Zhang, and B. Heber, Modulation of galactic cosmic rays during the unusual solar minimum between cycles 23 and 24, *J. Geophys. Res.*, *119*, 1493–1506, doi:10.1002/2013JA019550, 2014.

Zurbuchen, T. H., N. A. Schwadron, and L. A. Fisk, Direct observational evidence for a heliospheric magnetic field with large excursions in latitude, *J. Geophys. Res.*, *102*, 24,175–24,181, 1997.